On micro to mesoscale homogenization of electrical properties for damaged laminated composites

(and their potential applications in electrical tomography)

Thesis by

Lakshmi Selvakumaran

In Partial Fulfillment of the Requirements

For the Degree of

Doctor of Philosophy

King Abdullah University of Science and Technology, Thuwal,

Kingdom of Saudi Arabia

December, 2015

The thesis of Lakshmi Selvakumaran is approved by the examination committee

Committee Member: Prof. Ibrahim Hoteit

Committee Member: Prof. Vassilis Kostopoulos

Committee Member: Prof. Gilles Lubineau

Committee Member: Prof. Serge Prudhomme

Committee Member: Prof. Ravi Samtaney

Committee Chairperson: Prof. Sigurdur Thoroddsen

King Abdullah University of Science and Technology

2015

ABSTRACT

On micro to mesoscale homogenization of electrical properties for damaged laminated composites (and their potential applications in electrical tomography)

Lakshmi Selvakumaran

Efficient and optimal use of composites in structures requires tools to monitor and capture the complex degradation that can occur within the laminates over time. Structural health monitoring (SHM) techniques uses sensors/actuators on the structure to progressively monitor the health of the structure with minimal manual intervention. Electrical tomography (ET) is a SHM technique that uses voltage measurements from the surface of the laminate to reconstruct a conductivity map of the structure. Since damage has been shown to modify the conductivity of the laminate, the conductivity map can provide an indirect measure of the damage within the material. Studies have shown the capability of ET to identify macroscale damage due to impact. But, little has been done to quantitatively assess damage using ET.

In this work, we present a theoretical framework to link degradation mechanisms occuring at the microscale to the conductivity at the mesoscale through damage indicators. The mesoscale damage indicators are then shown to be intrinsic to the ply. Next, we use the knowledge obtained through mesoscale homogenization to study the detectability of transverse cracks. Last, we show how the mesoscale homogenization participates in regularization of the inverse problem and in the quantitative assess-

ment of the reconstructed conductivity map. This is as such the first step towards turning ET into a viable quantitative health monitoring technique.

ACKNOWLEDGEMENTS

I would like to sincerely express my gratitude to my advisor Prof. Gilles Lubineau for being an excellent teacher and mentor. Without his incredible support and patience, this work would not have been possible. Thank you for making a researcher out of me. I would also like to extend my sincere thanks to Prof. Serge Prudhomme for his discussions and insights on my work. I would like to thank all my lab members at COHMAS for creating a friendly working and information sharing environment.

My deepest gratitude to Amber Siddiqui, Indira Rajagopalan, Abhinay Ramaprasad, Sunita Pawar, Prof. Ravi Samtaney, and Dr. Todd Pietruszka for providing incredible moral and emotional support during critical times. Your confidence in me brought back my confidence during the difficult times.

I would like to thank Ali, Annie, Basmah, Daniel, Farhan, Felix, Gustavo, Huma, Hanan, Huda, Idris, Islam, Konpal, Rasha, Rishabh, Rkia, Sud and Varsha for making KAUST a home away from home.

Last but not the least, I would like to thank my entire family and friends back home for all the support and love. Special thanks to my mom and sister for being my pillars of strength.

This thesis is dedicated to all of you.

TABLE OF CONTENTS

LIST OF FIGURES

LIST OF TABLES

Chapter 1

Introduction

Laminated composites possess superior mechanical properties, such as high strength-to-weight ratio, corrosion resistance, and better fatigue properties in comparison to metals, which make them ideal candidates for long-term structural applications [7]. In spite of their proven advantages, the behavior of composites is complex when compared to classical metallic materials, due to the wide range of possible degradation mechanisms. The possible degradation mechanisms can be broadly classified as: intralaminar degradation, which includes fiber breakage [8, 9], diffuse damage [10, 11], transverse cracking [12, 13, 14], and local delamination [15, 16, 17, 18, 19], and interlaminar degradation which mainly includes delamination. Furthermore, significant damage can occur in such materials without being visible over the surface, which in turn makes real-time monitoring crucial. Being able to track and monitor the initiation and evolution of degradation in composites is key to the successful usage of such complex materials with high level of confidence.

Techniques to evaluate the degradation state without damaging the material is termed as non-destructive testing (NDT). Some of the commonly used NDT techniques are ultrasonics, thermography, X-ray tomography, etc. Traditional NDT techniques can only be used offline and often requires dismantling of the part to be tested.

It also involves bulky and expensive equipment and skilled labor to carry out the inspection process. This poses serious limitations in identifying damage in composites. With the advances of sensor technology, some of the NDT methods have been adapted as structural health monitoring (SHM) techniques. SHM techniques can possibly be used *in-situ* to obtain information about the presence of degradation [20] without having to dismantle the structure. However, using the SHM techniques to categorize and quantitatively assess damage in composites is still a challenge. Thus, NDT techniques are suitable for refined inspection of parts that have been clearly identified as damaged while SHM techniques, which are comparatively fast, efficient, and cost-effective, can be used for detecting the initiation and location of such damage within the system during operation [20].

SHM techniques that are currently available include optical fibers [21], acoustic emission [22], ultrasonics [23], modal analysis [24], lamb waves [24, 25, 26], strain memory alloy method [24], and eddy current techniques [27]. Most of these techniques require sensors/actuators that are sometimes expensive, offer poor resolution and often require the system to be non-operational.

Electrical tomography (ET) is a SHM technique that has the potential to be used in *real-time* and *in-situ*. Depending on the current source, ET can be classified as ERT (Electrical Resistance Tomography) or EIT (Electrical Impedance Tomography). ERT which uses DC currents, or EIT which uses AC currents, aims at reconstructing the conductivity field within the inspected part based on a set of electrical measurements on the surface. It can be used to identify damage in materials since damage can alter the conductivity of the material. It does not require expensive sensors/actuators and can be non-invasive. Since the reinforcements of the laminate are part of the sensing network, the laminate can be tailored to become sensitive to the different modes of damage. However, ET is not straightforward for composites due to 1) complex damage mechanisms, and 2) electrical orthotropy. The electrical orthotropy demands the development of sophisticated measurement/reconstruction techniques and the complex damage mechanisms make the interpretation of the acquired conductivity difficult. The full potential of ET for composites has not been achieved yet.

Identifying damage in composites via ET can be viewed as a two-step process, involving two inverse problems. The first one is a global inverse problem where the conductivity map of the material is recovered from the finite number of voltage measurements obtained on the surface. The measurements themselves are obtained by applying current through pairs of electrodes and measuring the potential difference between all other subsequent pairs of electrodes. This inverse problem always constitutes an ill-posed problem due to the limited amount of information provided by the data over the boundary to describe the complex continuous field of the material in the bulk [28, 29]. The second one is a local inverse problem that involves using the conductivity map obtained from the reconstruction process to locally correlate the conductivity values to the various damage mechanisms in the composite. The solution of this inverse problem is also non-unique as the obtained conductivity can be interpreted in multiple ways in terms of the different underlying possible damage mechanisms.

Studies using ET for composites so far focus on obtaining the conductivity map and correlating to the presence or absence of large scale damage. However identification of small scale damage such as transverse cracks is crucial but missing. This is important because in fiber reinforced laminates, system failure often initiates through transverse cracks. To make ET sophisticated enough to track such small scale damage, we need systemic models that can bridge the microscale damage to the conductivity at a larger scale. Until such link is established, ET cannot be used as a reliable health monitoring technique.

The current work focuses on developing the bridge between the conductivity of the ply and the various microscale damage mechanisms through mesoscale homogenization. This model provides a clear relationship between how mechanisms such as transverse cracking and local delamination affects the conductivity at the ply level. In addition, it also participates in the regularization of the inverse problem and in the interpretation of the reconstructed conductivity.

The influence of different geometrical and material parameters of the laminate on the sensitivity of measurements towards transverse cracking is discussed. Finally, a preliminary demonstration of the mesoscale homogenization guided electrical tomography on two commonly used laminate configurations is shown.

The thesis is organized as follows: a comprehensive literature review is presented in the following chapter. In the end of Chapter 2, the problem statement and the objectives are outlined. In Chapter 3, the core of the work, which is the mesoscale homogenization, is presented. The equivalent mesoscale model for the microscale degradation is developed and is proved numerically to be valid for any laminate configuration. Special focus is then given towards identifying transverse cracks using ET. In Chapter 4, the results from mesoscale homogenization is used to study the effect of the various geometrical and material parameters of the laminate on detectability of transverse cracks. Chapter 5 presents simple numerical experiments to show the capability of the mesoscale model in identifying the level of transverse cracks in the laminate. Last, we outline the impact of the work and present recommendations for future work.

Chapter 2

Background, state-of-the art and objectives

2.1 Damage in composites

Damage in composites is a complex phenomenon involving a number of different mechanisms happening simultaneously and interacting with each other. Extensive experimental campaigns have been carried out to figure out the details regarding initiation, propagation and interactions of these mechanisms. A simple schematic of the various mechanisms is shown in Fig. 2.1.

Fiber breaking Fibers are the main load carrying component in the composite due to their high strength and stiffness [8]. Individual fibers are non homogenous in general and exhibit varying strength along the length [9]. Fiber breaking mainly occurs when the tensile load in the fiber direction exceeds a critical value. Fiber breaking is usually brittle in nature as the fiber is a brittle material. Fiber kinking/buckling occurs when the ply is loaded in compression. Fiber damage results in the degradation of the fiber/matrix interface thereby damaging the matrix and the interface as well.

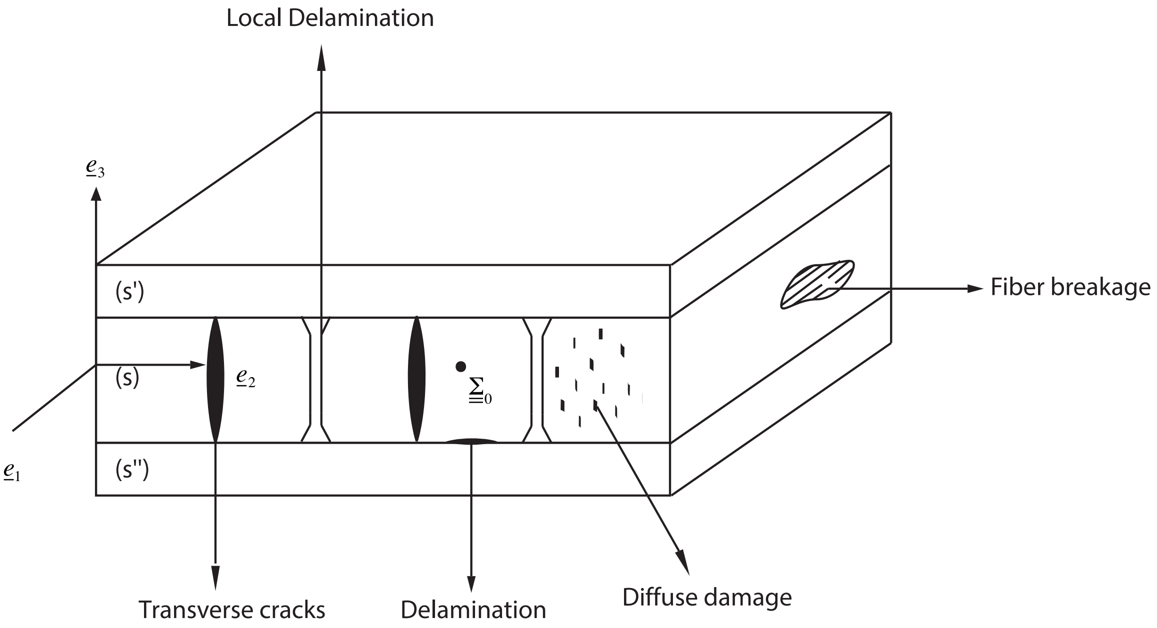

Figure 2.1: A schematic of various damage mechanisms in laminate

Diffuse ply damage Generally, damage starts within the composite as microcracks within the matrix and as fiber/matrix debonding [10, 11]. Fiber/matrix debonding occurs mainly due to the stress concentrations at the interface. The fiber/matrix interface is characterized to have the lowest strength when compared to the individual constituents. Thus even the matrix microcracks extend towards the interface and extend along the fiber direction. Debonding primarily starts at the free edge with increase in the debonding angle with increasing stress. Then the debonding propagates along the fiber direction after a critical debonding angle is reached. The microcracks and fiber/matrix debonding are together commonly referred to as diffuse ply damage.

Transverse cracks With increasing stress, the debonds and the microcracks coalesce together and extend through the thickness of the ply in the direction transverse to the loading to form the transverse cracks [30]. The formation of transverse cracks increases with increasing thickness, with stable microcracks for thinner plies. The transverse cracks are quantified through the crack density which is the number of cracks per unit length. Transverse cracks are the primary transverse stiffness reducing damage mechanism in the ply [31] and acts as the initiation point for local delamination. Hence monitoring transverse cracks is crucial.

Delamination Local delamination starts at the edges of the crack tips of transverse cracks and runs along the interface between the plies, once the transverse crack density has reached a critical value[15, 16, 17]. Edge delamination initiates at the free edges because of the out-of-plane stresses. Edge delamination and the local delamination may coalesce together to result in macroscopic delamination.

2.2 NDT and SHM for composites

Most of these damage mechanisms discussed above can occur without being visible on the surface. Fig. 2.2 shows an example of how a low energy impact typically results in "barely visible impact damage". These different damage mechanisms although not visible on the surface can compromise the integrity of the structure in regular use. Hence, monitoring the health of the laminate regularly is crucial for successful usage of composites. A range of NDT techniques are currently available to evaluate the health of composites. A list of the standard NDT techniques with their capabilities are summarized in Fig. 2.3. In Fig. 2.3, "+" or yellow corresponds to "positive performance", "0" or green corresponds to "with limitations" and "-" or grey "prohibitive". These techniques require expensive and bulky equipment, skilled labor, and the structure to be non-operational. From Fig. 2.3, we see that apart from Thermography, the field of view is very limited for the other techniques, requiring large structural scanning times. These limitations prohibit frequent inspection cycles especially when the structure is inaccessible (for eg: underground pipes). With the advent of sensors and actuators, much of the NDT techniques have been translated to SHM techniques where the sensors/actuators are embedded over the composite and various parameters are monitored over time. This addressed the major drawbacks for NDT as SHM made *in-situ* and offline monitoring possible.

SHM techniques can be broadly classified as active and passive techniques. Active techniques use actuators to send in excitation signals which are then picked up by sensors. The change in the reponse from the excitation signal is then used to identify damage/strain. This includes techniques like ultrasonics, optical fibers, etc. Passive techniques uses sensors to pick-up signals from the material which can then be interpreted for damage. Acoustic emission is a passive SHM technique. The primary difference between active and passive SHM is that active SHM can capture existing damage while passive SHM cannot. Some of the major SHM techniques are listed in table. 2.1 along with their advantages and limitations.

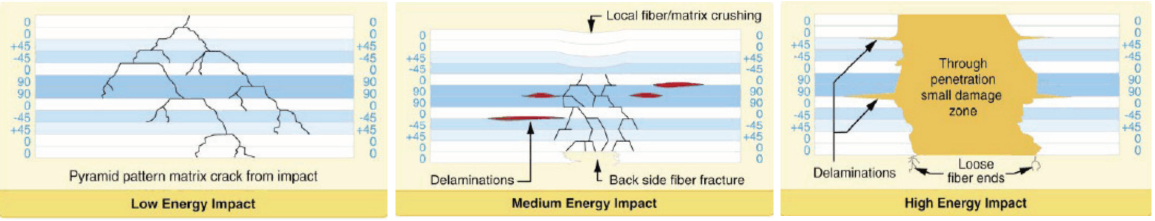

Figure 2.2: Damage observed with different levels of impact load (source: www.flightlearnings.com)

Most of the SHM techniques are limited in the scope of their application because: (i) the resolution is poor, (ii) all damage types cannot be identified, (iii) characterization is difficult, and/or (iv) requires that the system be non-operational. Electrical tomography which has been predominantly used for medical imaging [32] and geophysical imaging [33, 34] is also used for structural health monitoring. In ET, electrodes are placed over the surface of the structure and current is passed between pairs of

Technique	Physics	Parameter observed and detection principle	Advantages	Limitations	References
Optical fibers	Light	Change in phase/wavelength/ intensity –> change in strain/temperature	Sensitive to strain;flexible;Immune to EMI	Expensive; Damage is interpreted from strain and is difficult	[21]
Acoustic emission	Sound	Bursts/counts –> damage	Sensitive to damage; Inexpensive sensors	Characterization (size, type, location) of damage is difficult; cannot identify existing damage	[22]
Ultrasonics	Sound	Signal Amplitude change/time of flight of signal –> damage	Widely used for delamination; Sensitive	Can only track damage perpendicular to the signal; Field view is limited	[23]
Modal analysis	Vibration	Change in natural frequency/mode shape/-damping –> stiffness change	Global method; Sensitive	Characterization of damage is difficult; Low resolution damage cannot be detected; Structure has to be non-operational	[24]
Lamb waves	Vibration	Change in transmitted waves –> damage	Global method; Sensitive	Structure has to be non-operational; Generation of pure lamb wave is difficult; scattering is complex for composites	[24, 25, 26]
Strain memory alloy method	Magnetism	Change in magnetic susceptibility –> strain	Sensitive to strain	Can track local changes in strain	[24]
Eddy current	Electro - magnetism	Change in mutual inductance –> damage	Sensitive	Can only track local damage	[27]

Table 2.1: Different SHM methods available

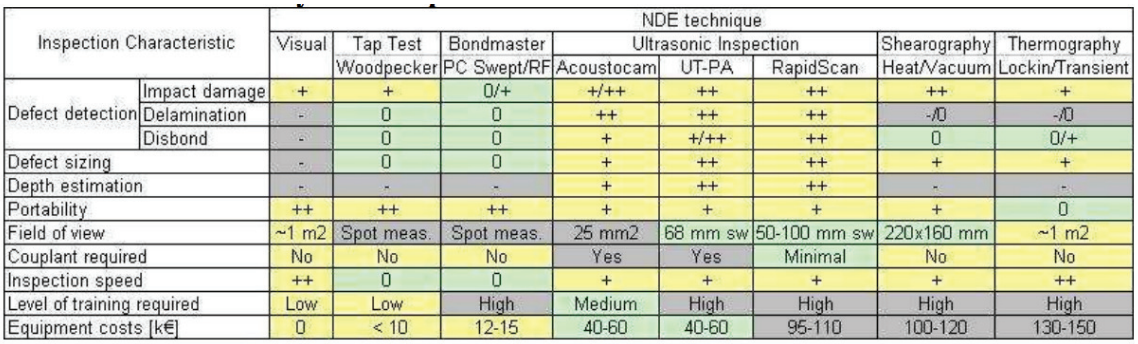

Inspection Characteristic		NDE technique							
		Visual	Tap Test	Bondmaster	Ultrasonic Inspection			Shearography	Thermography
			Woodpecker	PC Swept/RF	Acoustocam	UT-PA	RapidScan	Heat/Vacuum	Lockin/Transient
Defect detection	Impact damage	+	+	0/+	+/++	++	++	++	+
	Delamination	-	0	0	++	++	++	-/0	-/0
	Disbond	-	0	0	+	+/++	++	0	0/+
Defect sizing		-	0	0	+	++	++	+	+
Depth estimation		-	-	-	+	++	++	-	-
Portability		++	++	++	+	+	+	+	0
Field of view		~1 m2	Spot meas.	Spot meas.	25 mm2	68 mm sw	50-100 mm sw	220x160 mm	~1 m2
Couplant required		No	No	No	Yes	Yes	Minimal	No	No
Inspection speed		++	0	0	+	+	+	+	++
Level of training required		Low	Low	High	Medium	High	High	High	High
Equipment costs [k€]		0	< 10	12-15	40-60	40-60	95-110	100-120	130-150

Figure 2.3: NDT techniques and their capabilities [1]

electrodes and voltage is measured from the other/remaining pairs of electrodes. The voltage measurements are used to reconstruct the change in the conductivity of the material over time by solving the inverse problem. The conductivity map obtained from the tomography can be used to detect degradation in a structure, provided a clear relation is established between the mechanisms of degradation and the way they affect the conductivity. ET can also be used in *real-time* and *in-situ* which is an advantage over most SHM techniques. In the following section, we will review the mathematical nature of ET, followed by the electrical behavior of composite laminates and the state of the art in damage identification in composites by ET.

2.3 Electrical Tomography: theory and mathematical formulation

Electrical Tomography (ET) is the process of reconstructing the conductivity map within the domain of interest from the voltage measurements obtained over the surface of the domain. This involves current injection through pairs of electrodes and voltage measurements between the remaining pairs of electrodes. This problem is the inverse of the quasi-static conduction problem which solves for the voltage measurements at the electrodes for a given conductivity map and can be modeled using a set of

PDEs that mimics the experimental set-up. In ET terminology, this model is referred to as Complete Electrode Model (CEM). We begin with discussing the quasi-static conduction problem and then move on to discuss solving the ET problem with various inverse algorithms.

2.3.1 Quasi-static conduction problem

Let Ω be a domain with electrodes $el = 1, 2, ..., n_{el}$ on the surface $\delta\Omega$. Let $\underline{\underline{\Sigma}}$ denote the electrical conductivity of the bulk material Ω and z_{el} denote the contact impedance between the electrode el and $\delta\Omega$. The schematic of the system is described in Fig. 2.4. In electrical tomography, current is applied between pairs of electrodes and voltage is then measured between the other pairs of electrodes. Let I_{el} be the current applied between the electrodes used for current injection, S_{el}, and $\{v\}_1 = \{v_1, ..., v_{n_{el}-2}\}$ be the set of voltage measurements obtained from remaining pairs of electrodes. We denote the electric potential, electric potential at the electrodes, electric field and current density at any point, $\underline{x}$, within the domain Ω as $(u, v, \underline{E}, \underline{J})$ respectively. We solve the quasi-static conduction problem given as: to find (u, v) such that,

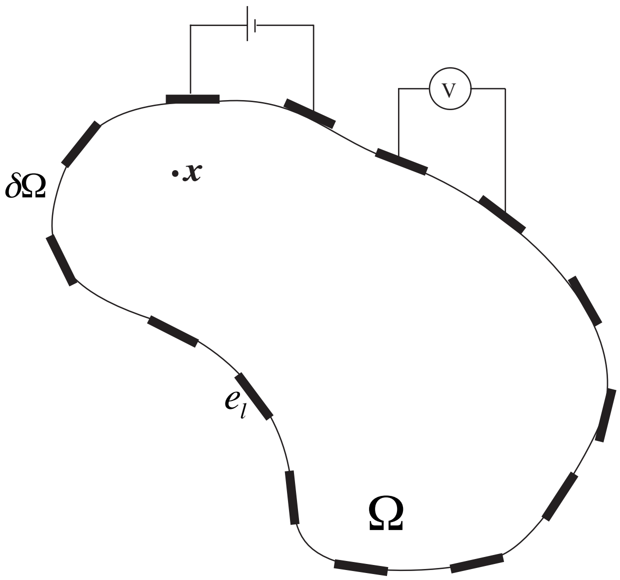

Figure 2.4: Schematic of electrical tomography

- *Kinematic admissibility*

$$\underline{E} = -\nabla u \quad \forall \underline{x} \in \ \Omega \tag{2.1}$$

- *Static admissibility*

$$\nabla \cdot \underline{J} = 0 \quad \forall \underline{x} \in \ \Omega \tag{2.2}$$

$$\int_{e_l} \underline{J} \cdot \underline{n} dS_{e_l} = I_{el} \ \ on \ \ S_{e_l}, e_l = \text{Inj. elec. 1} \tag{2.3}$$

$$\int_{e_l} \underline{J} \cdot \underline{n} dS_{e_l} = -I_{el} \ \ on \ \ S_{e_l}, e_l = \text{Inj. elec. 2} \tag{2.4}$$

$$\underline{J} \cdot \underline{n} = 0 \ \ on \ \ \delta\Omega \backslash \cup e_l \tag{2.5}$$

- *Constitutive equation*

$$\underline{J} = -\underline{\underline{\Sigma}} \otimes \underline{E} \quad \forall \underline{x} \in \ \Omega \tag{2.6}$$

$$v_{el} - u = z_{el}(\underline{J} \cdot \underline{n}) \ \ on \ \ e_l, l = 1, ..., n_{el} - 2 \tag{2.7}$$

- *Conservation equations*

$$\sum_{el=1}^{n_{el}} I_{el} = 0 \tag{2.8}$$

$$\sum_{el=1}^{n_{el}} v_{el} = 0 \tag{2.9}$$

Let t denote the total number of injection patterns considered. Then $V = \{\{v\}_1, ..., \{v\}_t\}$ denotes the complete set of voltage difference measurements and is a vector of size M where M denotes the number of measurements. Given that the applied current remains constant, the electric potential measured at the electrodes depends only on the conductivity of the material. Thereby, when damage modifies the conductivity, the magnitude of change in the electric potential depends only on the magnitude of the change in components of the conductivity tensor $\underline{\underline{\Sigma}}$. This can be used to identify the damage.

2.3.2 The inverse problem

In a typical reconstruction problem, the conductivity to be reconstructed is the discretized conductivity which is mostly taken to be constant per element of the finite element mesh. In the following discussion, Σ denotes the discretized conductivity and is taken to be isotropic for simplicity. If $V_{meas} \in \mathbb{R}^{M\times 1}$ denotes the set of voltage measurements obtained from the experiments and $V_{calc} \in \mathbb{R}^{M\times 1}$ denotes the measurements obtained from solving the quasi-static problem defined above, then the discretized conductivity map $\Sigma \in \mathbb{R}^{N\times 1}$, that best fits the experimental measurements can be obtained by minimizing the gap between V_{meas} and V_{calc} with least squares method. M denotes the number of measurements and N denotes the number of parameters to be reconstructed. The number of parameters denotes the number of discrete conductivity values that are reconstructed. The objective function to be minimized can be given as:

$$\Sigma = \|V_{meas} - V_{calc}(\Sigma)\|_2^2 \tag{2.10}$$

The minimum to this function can be obtained by finding the gradient and equating it to zero.

$$V_{calc}'^{T}(\Sigma)(V_{meas} - V_{calc}(\Sigma)) = 0 \tag{2.11}$$

Linear Case If $V_{calc}(\Sigma)$ is linear with respect to Σ, then the gradient $V'_{calc}(\Sigma)$ can be given by

$$V'_{calc}(\Sigma) = J = \frac{\partial V}{\partial \Sigma}$$

The gradient $J \in \mathbb{R}^{M \times N}$ is the Jacobian matrix or sensitivity matrix of the system. The Jacobian or the sensitivity matrix defines the forward mapping and is calculated as the change in the measurements for small perturbation of every conductivity parameter [28]. Then the solution (2.11) becomes

$$J^T(V_{meas} - J\Sigma) = 0 \tag{2.12}$$

$$J^T V_{meas} - J^T J\Sigma = 0 \tag{2.13}$$

$$\Sigma = (J^T J)^{-1} J^T V_{meas} \tag{2.14}$$

where $(J^T J)^{-1} J^T$ is known as the pseudoinverse or Moore-Penrose inverse of J.

Non-linear Case If $V_{calc}(\Sigma)$ is non-linear with respect to Σ, then $V'_{calc}(\Sigma)$ can be approximated by linearizing $V_{calc}(\Sigma)$ around a initial Σ_0 that is close to Σ. Using Taylor's series, $V_{calc}(\Sigma)$ can be expanded as

$$V_{calc}(\Sigma) = V_{calc}(\Sigma_0) + V'_{calc}(\Sigma_0)(\Sigma - \Sigma_0) + O(\|\Sigma - \Sigma_0\|^2) \tag{2.15}$$

Neglecting the higher-order terms $O(\|\Sigma - \Sigma_0\|^2)$ and taking $V'_{calc}(\Sigma_0)$ as J we introduce (2.15) in (2.11),

$$J^T(\Sigma_0)(V_{meas} - V_{calc}(\Sigma_0)) - J^T(\Sigma_0)J(\Sigma_0)(\Sigma - \Sigma_0) = 0 \tag{2.16}$$

$$\Sigma = \Sigma_0 + (J^T(\Sigma_0)J(\Sigma_0))^{-1}J^T(\Sigma_0)(V_{meas} - V_{calc}(\Sigma_0)) \tag{2.17}$$

Here $J(\Sigma_0)$ denotes the Jacobian matrix calculated at Σ_0. This is known as the Gauss-Newton method and can be solved directly or iteratively until the desired tolerance is reached. It is the most widely used algorithm in solving the inverse problem.

Ill-posedness of the inverse problem The Jacobian matrix is usually severely rank-deficient as the number of independent measurements is typically far lesser than the number of parameters to be reconstructed. This makes the inverse problem ill-posed. The ill-posedness can be quantified by calculating the condition number and by analyzing the singular values of the Jacobian matrix. Polydorides and Borsic [28, 29] analyzed the Jacobian obtained from a model that was close to a typical ET problem in medical field and showed that the condition number was of the order of 15. The smallest singular values were in the order of 10^{-17}. Such ill-conditioned problems need regularization to obtain reliable results in the presence of noise. Regularization introduces prior information about the problem into the solution and stablizes the inversion. There are different methods to regularize the problem. Prominent methods are Tikhonov regularization, Constrained least squares, Truncated SVD, Bayesian inference techniques such as Maximum a posteriori (MAP), MCMC methods, and reduced order models. For special cases, the Bayesian methods can be shown to reduce down to deterministic methods such as Tikhonov regularization/ least squares. The different methods used for solving the ET problem are discussed briefly below. For a detailed mathematical analysis of the different methods listed below, the reader is referred to [28, 35, 36]. We will consider the linear version of equation (2.11) in the derivations. The methods discussed below can be extended to the non-linear case.

Truncated singular value decomposition The inverse of J can be calculated using the singular value decomposition (SVD) method where the Jacobian is decomposed as $J = UST^T$ (U and T are orthogonal matrices and S is a diagonal matrix containing the singular values of J). The solution to the least squares problem is now written as

$$\Sigma = TS^{-1}U^T V_{meas} = \sum_{i=1}^{M} \frac{U_{.,i}^T V_{meas}}{\lambda_i} T_{.,i} \tag{2.18}$$

where $TS^{-1}U^T$ is the pseudo inverse of J. To eliminate noise in the solution and to improve the condition number of the matrix, smaller singular values which are the source of the noise are truncated. The solution is given as

$$\Sigma = \sum_{i=1}^{M} f_i \frac{U_{.,i}^T V_{meas}}{\lambda_i} T_{.,i} \tag{2.19}$$

f_i are known as the filter factors. If k is the level of truncation of the high frequency terms, then

$$f_i = \begin{cases} 1 & i \le k \\ 0 & i > k \end{cases}$$

However, TSVD results in lower resolution [37].

Tikhonov regularization Here the solution of the problem is regularized by adding additional constraints on the solution. Thus the solution is driven towards this constraint. The Tikhonov regularized problem is obtained by modifying the objective function of the minimization problem given by (2.11).

$$\|V_{meas} - J\Sigma\|_2^2 + \alpha\|\Sigma\|_2^2 \tag{2.20}$$

where α is the regularization parameter and $\|\Sigma\|_2^2$ is the regularization function. This is also known as the 0-order Tikhonov method. The solution is given as

$$\Sigma = (J^T J + \alpha I)^{-1} J^T V_{meas}$$

Here $(J^T J + \alpha I)$ is invertible and gives a unique solution. Also, the solution is stable as it filters out the smaller singular values in the data. The Tikhonov regularization is equivalent to the Truncated SVD as the solution of the Tikhonov regularized problem can be represented as

$$\Sigma = \sum_{i=1}^{p} \frac{\lambda_i^2}{\lambda_i^2 + \alpha} \frac{U_{.,i}^T V_{meas}}{\lambda_i} T_{.,i}$$

where $\dfrac{\lambda_i^2}{\lambda_i^2 + \alpha}$ is comparable to filter factor,f_i ($\lambda_i \gg \alpha, f_i \approx 1$ and $\lambda_i \ll \alpha, f_i \approx 0$).

The choice of the regularization parameter determines the accuracy of the solution we obtain. Larger regularization parameter tends to force the solution towards the regularization function and results in lesser fit to the data. On the other hand, very low value of the regularization parameter results in more fit to the data but lesser emphasis on the regularization function. The optimal value of the regularization parameter is usually identified using the L-curve which is the log of the norm of the solution vs the log of the norm of the residual. There are other methods like Generalized cross-validation, Noise figure method, etc. to arrive at the optimal value as well but L-curve is the most commonly used method. Optimal value of the regularization parameter is the one that minimizes both the norms. It is the value of α at the elbow of the L-curve.

Higher-order Tikhonov regularization uses the L2-norm of the first, second or higher derivatives of the solution as the regularization function

$$argmin\|V_{meas} - J\Sigma\|_2^2 + \alpha\|L\Sigma\|_2^2$$

where L denotes the differentiation operator on the solution.

M. Goharian et al., K. Wu et al., M. Vauhkonen et al., Q. Wang et al., and A. Baltopoulos et al. [38, 37, 39, 40, 5, 41, 42] discuss the implementation of this algorithm with different regularization matrices. This is the most common method used for regularization. L2 norm regularization results in the loss of resolution as it is mainly a smoothness prior. Regularization based on L1 norm are better to reconstruct sharp discontinuities and are discussed in detail in [40, 43].

Total variation regularization The main disadvantage of the Tikhonov regularization technique is that the discontinuity in the solution is smoothed out by the regularization function. One way to retain the discontinuity across the solution is to use the total variation technique [37]. The problem is then written as

$$argmin\|V_{meas} - J\Sigma\|_2^2 + \alpha\int_{\Omega}|\nabla\Sigma|d\Omega$$

where $\int_{\Omega}|\nabla\Sigma|d\Omega$ is the total variation of Σ.

Probabilistic approach

In the probabilistic approach the unknown variables are treated as random variables and the prior information can be naturally incorporated into the model [44, 45]. The output is essentially a probability distribution for the unknown(model) variables (Σ). This is obtained through Bayes' theorem which states that the joint probability is given by

$$\pi(\Sigma, V_{meas}) = \pi(\Sigma)\pi(V_{meas}|\Sigma) = \pi(V_{meas})\pi(\Sigma|V_{meas})$$

The posterior probability is obtained as

$$\pi(\Sigma|V_{meas}) = \frac{\pi(\Sigma)\pi(V_{meas}|\Sigma)}{\pi(V_{meas})}$$

Here, $\pi(V_{meas}|\Sigma)$ is the conditional probability of V_{meas} given the model Σ, also known as the likelihood density, $\pi(\Sigma)$ is the prior density and $\pi(V_{meas})$ is the norming constant which is usually ignored.

The output of the Bayesian approach is a probability distribution and not a single estimate. Various approaches namely the maximum likelihood estimate, the maximum a posteriori estimate, or conditional expectation method can be used to obtain single estimates.

Maximum A Posteriori Estimate The maximum a posteriori method estimates the model with the highest posterior density probability

$$\Sigma_{MAP} = argmax_{\Sigma}\pi(\Sigma|V_{meas}) \tag{2.21}$$

Here, the method tries to identify the best model that minimizes the error between the data and the prior information thus leading to an optimization problem such as the regularized least squares. The variance of the data determines how much the posterior density depends on the prior information, i.e. a large variance on the prior information move the solution towards the data provided. Likewise, a large variance on the input data and a lower variance on the prior makes the solution move towards the prior information given.

This method has the advantage of being able to include statistical information about the data and the measurements [46]. The reader is referred to [47] for the definitions and derivations of the objective function. The objective function is obtained by maximizing the posterior probability. Considering that the probability density is Gaussian, the objective function reduces to

$$\|V_{meas} - J\Sigma\|^2_{R_n^{-1}} + \|\Sigma - \Sigma_\infty\|^2_{R_\Sigma^{-1}} \tag{2.22}$$

$$\Sigma = arg\,min[(V_{meas} - J\Sigma)^T R_n^{-1}(V_{meas} - J\Sigma) + (\Sigma - \Sigma_\infty)^T R_\Sigma^{-1}(\Sigma - \Sigma_\infty)] \tag{2.23}$$

which yields the estimate

$$\Sigma = (J^T R_n^{-1} J + R_\Sigma^{-1})^{-1}(J^T R_n^{-1} V_{meas} + R_\Sigma^{-1}\Sigma_\infty) \tag{2.24}$$

where R_Σ, Σ_∞ denote the statistical properties of the prior such as its covariance and mean. Similarly R_n denotes the covariance of the noise from the measurements.

Maximum Likelihood Estimate The maximum likelihood estimate takes the model that maximizes the likelihood of the data. This typically tries to minimize the error between the data and the estimate thus leading to a least squares optimization problem.

$$\Sigma_{ML} = argmax_\Sigma \pi(V_{meas}|\Sigma) \tag{2.25}$$

$$\Sigma = arg\,min[(V_{meas} - J\Sigma)^T R_n^{-1}(V_{meas} - J\Sigma)] \tag{2.26}$$

Since the method does not account for the noise, the results are sensitive to noise in the measurements.

Conditional Expectation Conditional expectation is another estimate where the mean error between the posterior data and the estimated value is minimized and the following integral is evaluated:

$$\Sigma_{|V_{meas}} = \int \Sigma\pi(\Sigma|V_{meas})d\Sigma$$

The calculation of this integral is done using Monte Carlo method. The integration is done by approximating the integral by a ergodic average from systematic samples that are drawn from the posterior distribution using a Markov chain method. Metropolis-Hastings and the Gibbs sampler method are some of the algorithms that randomly moves through the distribution to generate the sample ensemble.

Reduced order model based on POD All studies that use the methods described above for regularization assume piecewise constant conductivity over the finite element mesh. Thus the conductivity is represented over the basis of the finite element mesh itself. The work by [48] explores the possibility of using a reduced-order model where the space of the conductivity and the voltage distribution are projected on a basis constructed by proper orthogonal decomposition (POD) method. These bases are constructed from the eigenvectors of the covariance matrices of the data sets. Highly correlated data can be represented by low number of POD modes, which drastically reduces the number of parameters to be calculated, thereby regularizing the problem and reducing the computational time.

2.4 Conductivity in composites

Composite laminates exhibit orthotropic electrical behavior i.e., the electrical conductivity is orthotropic [49, 50, 51]. The conductivity tensor $\underline{\underline{\Sigma}}^{\circ}$ of a composite ply, before the development of any damage, is assumed to have the form [52]:

$$\underline{\underline{\Sigma}}^{\circ} = \begin{bmatrix} \Sigma_1^{\circ} & 0 & 0 \\ 0 & \Sigma_2^{\circ} & 0 \\ 0 & 0 & \Sigma_3^{\circ} \end{bmatrix}_{(e_1,e_2,e_3)} , \tag{2.27}$$

where (e_1, e_2, e_3) denotes the local coordinate system with respect to the ply, e_1 denotes the fiber direction, e_2 and e_3 represent the transverse and through-thickness directions, respectively.

We define "anisotropy ratio" λ, which is the ratio of the conductivity in the fiber direction to the conductivity in the transverse direction, i.e.

$$\lambda = \frac{\Sigma_1}{\Sigma_2} \tag{2.28}$$

We also define "through-thickness anisotropy ratio" λ_t, which is the ratio of the conductivity in the transverse direction to the conductivity in the through-thickness direction, i.e.

$$\lambda_t = \frac{\Sigma_2}{\Sigma_3} \tag{2.29}$$

Composite laminates predominantly used in structural applications are carbon fiber reinforced plastic (CFRP), glass fiber reinforced plastic (GFRP), nanoparticle doped CFRP and nanoparticle doped GFRP. Table 2.2 shows the conductivity of the primary constituents used in making these composite laminates. Typical epoxy and

Material	Nanomaterial (wt %)	Conductivity (S/m)	References
Pure epoxy	-	$10^{-13} - 10^{-10}$	[53, 54]
Carbon fiber	-	$5.8 \times 10^4 - 1.1 \times 10^5$	[56, 57]
Glass fiber	-	$2.5 \times 10^{-13} - 10^{-8}$	[55]
Nano-doped epoxy resin	MWCNT (up to 1%)	$10^{-9} - 1$	[59, 60]
	CB (up to 1%)	$10^{-10} - 0.1$	[58]

Table 2.2: Typical electrical conductivity values for primary constituents

glass fiber are insulators with conductivity in the range of $10^{-13} - 10^{-10}$ S/m [53, 54] and $2.5 \times 10^{-13} - 10^{-8}$ S/m [55] respectively while the carbon fiber is a conductor with conductivity ranging between $5.8 \times 10^4 - 1.1 \times 10^5$ S/m [56, 57]. Also, by doping the epoxy with nano particles such as carbon black (CB) or multi walled carbon nanotubes (MWCNT), the conductivity of the epoxy can be drastically improved to the range of 0.1-1 S/m [58] provided percolation is reached. Therefore, the electrical behavior of the laminate highly depends on the constituents of the composite laminate.

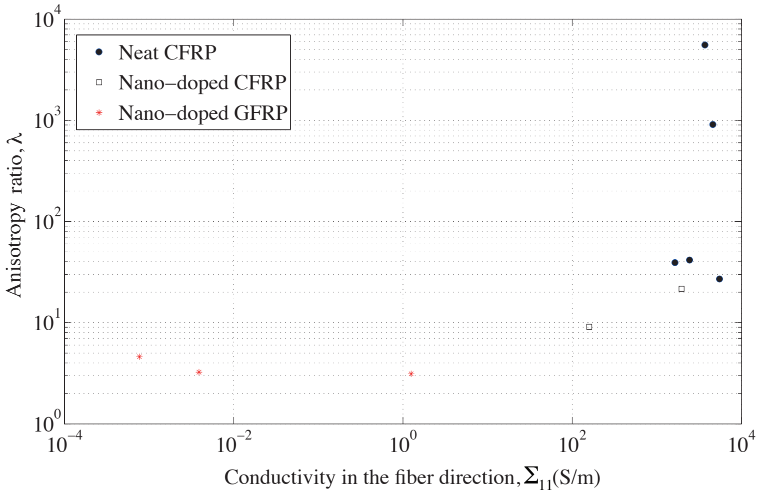

Figure 2.5: Variation of λ in typical composite laminates

For a typical CFRP, the conductivity in the longitudinal direction is mainly due to the conductivity along the fibers. The conductivity along the fiber direction can be well estimated based on the volume fraction and the properties of the individual

Material	Nanomat.	Vol. fr.	Σ°_{11} (S/m)	Σ°_{22} (S/m)	Σ°_{33} (S/m)	λ	λ_t	Ref.
CFRP	-	0.4	3700	0.666	0.0592	5555.6	11.25	[51]
	-	0.47	4600	5.06	1.012	909.1	5	[51]
	-	0.63	2439	58.8	1.02	41.5	57.7	[61]
	-	0.66	1639.3	41.67	30.3	39.3	1.4	[61]
	-	0.62	5500	203.5	20.9	27.02	9.74	[51]
Doped CFRP	3% CB-CC	0.654	1961	90.9	55.56	21.6	2.6	[61]
	1% CNT	-	158.73	17.47	2.11	9.1	8.28	[62]
Doped GFRP	2% CB	0.62	7.69×10^{-4}	1.68×10^{-4}	7.9×10^{-6}	4.6	21.27	[4]
	2% CB-CC	0.6	3.89×10^{-3}	1.2×10^{-3}	3×10^{-5}	3.24	40	[4]
	7% CB	0.3	1.25	0.4	1.11	3.2	0.4	[63]

Table 2.3: Typical electrical conductivity values for neat and doped laminates

constituents using the law of mixtures [49, 51]. Although an ideal ply would not conduct in the other two directions, conduction is observed along the transverse and through-thickness directions as well, due to contacts between fibers. However, the presence of matrix-rich interlamina makes the ply more conductive along the in-plane transverse direction than in the thickness direction. Thus, the electrical conductivity of the laminate can be characterized as follows: the electrical conductivity is much higher in the longitudinal direction than along the transverse direction, which in turn is higher than in the through-thickness direction. In other words, λ is large for a CFRP. Since carbon fiber is the only conducting material, the electrical measurements are highly sensitive to fiber breakage in comparison to the other forms of damage.

When the matrix is nano-doped, the conductivity in the transverse is improved, thereby decreasing λ and λ_t.

GFRP is not suitable for monitoring using ET since both the glass fibers and the matrix are insulators. However, nano-doped GFRP can be monitored using ET due to the presence of a conducting phase. It is to be noted that in the literature nano-doped GFRPs have the lowest λ. The following section summarizes the major studies using electrical measurements to sense damage and strain in composites.

2.5 Strain and damage sensing using electrical measurements

Studies that use electrical measurements to characterize damage and strain in the laminates can be broadly classified into three categories depending on the number of electrodes used and the method of damage interpretation. They are:

(1) Global behavior studies,

(2) Resistance/potential mapping studies,

(3) Electrical tomography studies.

We will review each of these studies in detail.

2.5.1 Global behavior studies

In these studies, two or four electrodes are used on beam type specimens to obtain a single resistance measurement between the two measurement electrodes. The electrical response of the laminate is characterized by simply monitoring the electrical resistance change of the specimen during loading. Measurements are usually made along the longitudinal, transverse or through-thickness directions. Depending on the direction of the measurements, the observed behavior changes due to the change in the conduction path. The observed global resistance change is then correlated to the different conductivity changing mechanisms such as strain and damage. It provides limited information about the nature, size or the location of damage. Also, the obtained resistance change response is specific to the loading and the laminate configuration used and thus the behavior cannot be generalized. However, significant insights can be obtained from these studies. Some of them are highlighted below:

Piezoresistance

Under small strain, a reversible change in the resistance of the laminate is observed. This is known as piezoresistance. Piezoresistance depends on various factors namely the changes in the dimension and change in resistivity of the material. The change in resistivity is affected by degree of contact between the fibers, degree of fiber alignment and the direction of resistance measurement. Along each measurement direction, the mechanism of piezoresistance changes and they have been characterized experimentally in [64, 65, 66].

- **Longitudinal Piezoresistance** Longitudinal resistance is mainly affected by the dimensional change [64, 65, 66]. The little contribution from the resistivity change is mainly due to the change in the fiber alignment. This causes a resistivity decrease in tension due to straightening of the fibers along the current direction.

- **Transverse Piezoresistance** The main cause for the resistivity change along the transverse direction is the change in the fiber network. This is caused by two competing effects: fiber undulation and fiber-fiber contact changes [64]. During compression in the transverse direction, the fiber is elongated in the fiber direction which straightens the fibers thereby reducing the fiber-fiber contact. But at the same time, the compression brings the fibers closer, thereby increasing the area and the number of contacts between the fibers.

- **Through-thickness Piezoresistance** In the through-thickness direction, the contact resistivity changes at the interface decreased between the plies when compressed [65]. At the same time, the resistivity can increase due to the fiber undulation or decrease due to the compression effect.

Piezoresistive response in the composite is found to be highly dependent on the microstructure of the laminate. J. Xiao et al., [67] developed a laminate theory to model the piezoresistance at the mesoscale. Todoroki et al., [64] have extended the laminate theory to include the effect of the multiaxial loading on the piezoresistance changes. They combined the effect of resistance change due to strain in the direction and resistance change due to Poisson effect to describe the piezoresistance for each direction. Both Xiao's and Todoroki's models cannot capture the effects of the microstructure on the piezoresistive response unless a micromechanics based homogenization is priorly done. Their models require ply level piezoresistive coefficient matrix which are usually characterized experimentally. But these results, as pointed out by Todoroki, are strongly influenced by the nature and position of the electrodes and the microstructure and hence cannot be generalized.

The piezoresistive behavior described above is limited to CFRP. In nano-doped CFRP and GFRP, along with the above mentioned mechanisms, the change in the percolation network of the nanoparticles also contribute to the piezoresistance in the different directions.

Damage

Damage causes irreversible changes to the electrical resistance and this can be used to detect damage in composites. Different studies have tried to characterize the resistance changes with respect to the different damage mechanisms in the composite [68, 69, 70, 71, 72].

- **Fiber breakage**

  Fiber breakage in a ply reduces the number of current carrying fibers thereby causing a significant, step-wise increase in the resistance along the longitudinal direction [73, 74]. But this increase in resistance is not directly proportional to the number of broken fibers as the broken fibers still conduct in the transverse direction through the contact network. The electrical response due to fiber breakage was first modeled by J. B. Park et al.,[75] using the concept of electrical ineffective length. This electrical ineffective length is an internal tunable parameter and it signifies the length over which the fiber cannot function as an electrically conductive path when broken [75]. An empirical relation is then derived for the longitudinal resistance change based on the material parameters, ineffective length and model parameters that are fit to the experimental data. Z.H.Xia [76] then related the transverse resistance change to the longitudinal resistance change and the characteristic ineffective length and derived an analytical expression for the transverse resistance changes to damage.

- **Transverse cracks**

  Transverse cracks disrupt the complex three dimensional fiber network and induces an increase in the transverse electrical resistance. This results in increase in resistance[74] which reflects the reduction in the fiber-fiber contact. Studies by Todoroki et al. [77, 78, 79] monitored the effect of isolated matrix cracks in cross-ply laminates on the global electrical resistance changes. Todoroki then attempted to link the transverse cracking density to the observed resistance changes.

- **Delamination**

  Delamination disrupts the fiber-fiber contact between plies thereby increasing the global resistance of the laminate in the through-thickness direction. S. Wang et al., [80] monitored the damage due to impact by measuring the oblique resistance and found that it was sensitive towards damage due to delamination.

2.5.2 Resistance/potential change mapping methods

The natural extension of the global behavior studies is to introduce an array of electrodes on the laminate and acquire large set of data that can be interpreted for damage/strain. Current is injected through pairs of electrodes and multiple potential/resistance change measurements are obtained between the other pairs of electrodes. The measured potential/resistance change is directly used to locate the damage. The regions where significant change in potential/resistance are identified as areas with possible damage. It is to be noted that the mapping technique does not attempt to reconstruct the conductivity map. This method can be used to locate the zone around which damage is likely to have occurred although the nature of the damage is hard to characterize. These studies have been mainly carried out to characterize through-hole and impact damages. Some of the significant studies that utilize the mapping technique is outlined below. The resolution of the mapping depends on the density of the electrode array and can be limiting to large scale damages only.

Todoroki [51, 81] used multiple electrodes on one side of the surface to detect delaminations. The location and the size of the delamination was found by training Artificial Neural Networks (ANN) [82] or Response Surfaces (RS) [83, 84]. These models require extensive experimental data and the output is highly sensitive to the nature of the input data. Also, these models are configuration dependent i.e., it needs to be tuned for the specific configuration that is to be tested.

In [2, 3], multiple electrodes were used around the laminate to identify holes in CFRP laminate. Sixteen through-thickness electrodes were used to inject current and measure electrical potential. The in-plane measurements were used to locate the damage. Peaks were observed in the measurements obtained from the electrodes around the hole. The geometry along with the numerical and experimental results are shown in Fig. 2.6.

In [4], damage due to impact in carbon black doped GFRP is assessed by constructing a damage map from the measurements. The damage is assessed both in the in-plane and through-thickness directions by reconstructing two different damage maps. Each point in the in-plane damage map is assigned a damage value which can be calculated as the sum of the projections of all the measurements at that point. In the through-thickness direction, the resistance change between the top and the bottom electrodes is taken to be the damage. The measurement configuration and the obtained damage maps are shown in Fig. 2.7. The method provided a good match to the damage profile obtained using C-scan. The various damage profiles in Fig. 2.7 correspond to the damage for different intensity of the impact loading.

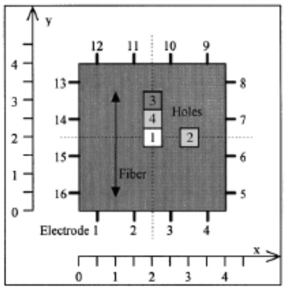

(i) Considered geometry and damage profile:
CFRP with hole

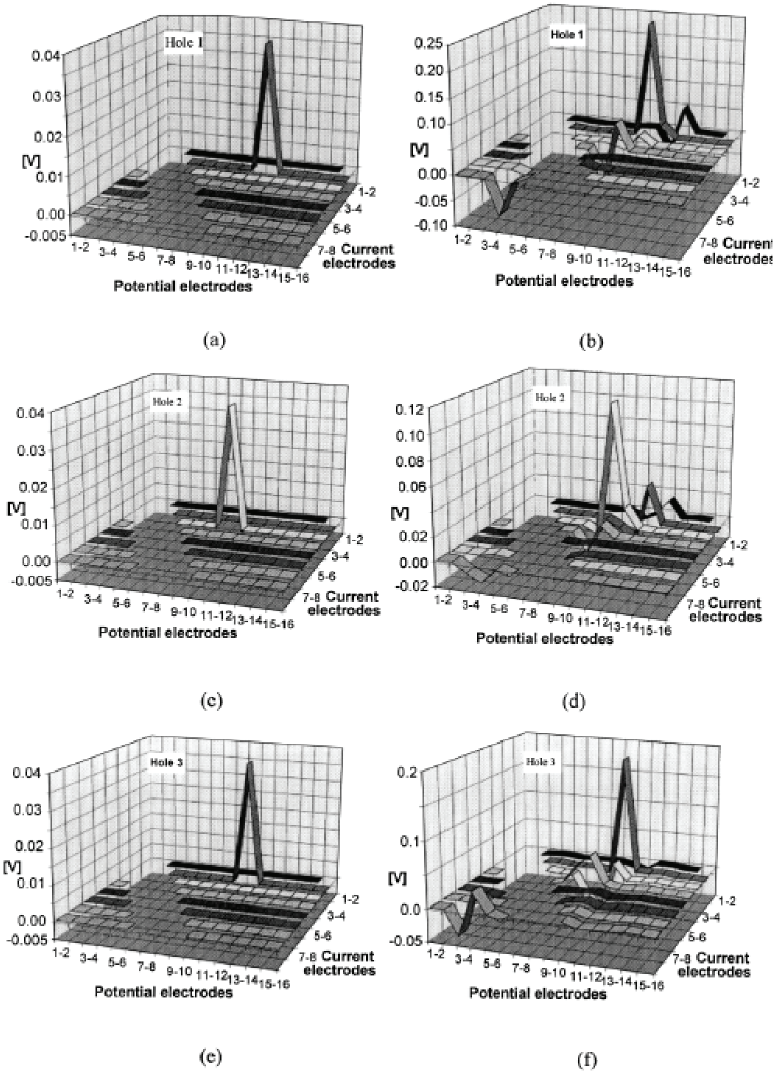

(a) (b)

(c) (d)

(e) (f)

(ii) Numerical (a,c,e) and experimental (b,d,f) results for
different hole positions

Figure 2.6: Considered geometry, and the obtained numerical and experimental potential change maps [2, 3]

2.5.3 Electrical tomography methods

Recent studies use the tomography principle to reconstruct the conductivity map of the laminate from the set of potential difference measurements. The conductivity map is then used to infer the location and size of damage. Although they provide detailed information about the state of damage within the material, the mathematical formulation for the inverse problem is ill-posed and needs regularization techniques. This has already been discussed earlier. One of the advantages of tomography over the mapping techniques is that the resolution can be significantly improved by introducing process specific information as regularization.

A. Baltopoulos et al. [5] used electrical tomography with Tikhonov regularization to reconstruct the damage due to impact on nano-doped woven glass fiber composite. The laminate was isotropic in the in-plane direction. Intrusive through-thickness electrodes placed around the laminate were used for the stimulation and measurements. The in-plane conductivity was reconstructed for two different damage modes: (i) drilled hole and (ii) indentation. The optimal conductivity profile was obtained by plotting the L-curve. Two damage indicators were introduced namely the center of interest (CoI) and region of interest (RoI). The center of interest identifies the location where most change in the conductivity is centered around and the region of interest identifies the zone where the conductivity change is significant. It was shown that these parameters were identified sufficiently close to the actual damage. The geometrical configuration and the reconstructed conductivity map are shown in Fig. 2.8. The dotted line in the figures shows the RoI and the cross mark shows the CoI. The circle marks the actual location of the damage. In their most recent work, A. Baltopoulos et al. [85] reconstructed the conductivity change map for CNT doped woven glass fiber composite. The performance of the reconstruction was investigated

(a) In-plane measurement pattern

(c) Through thickness measurement pattern

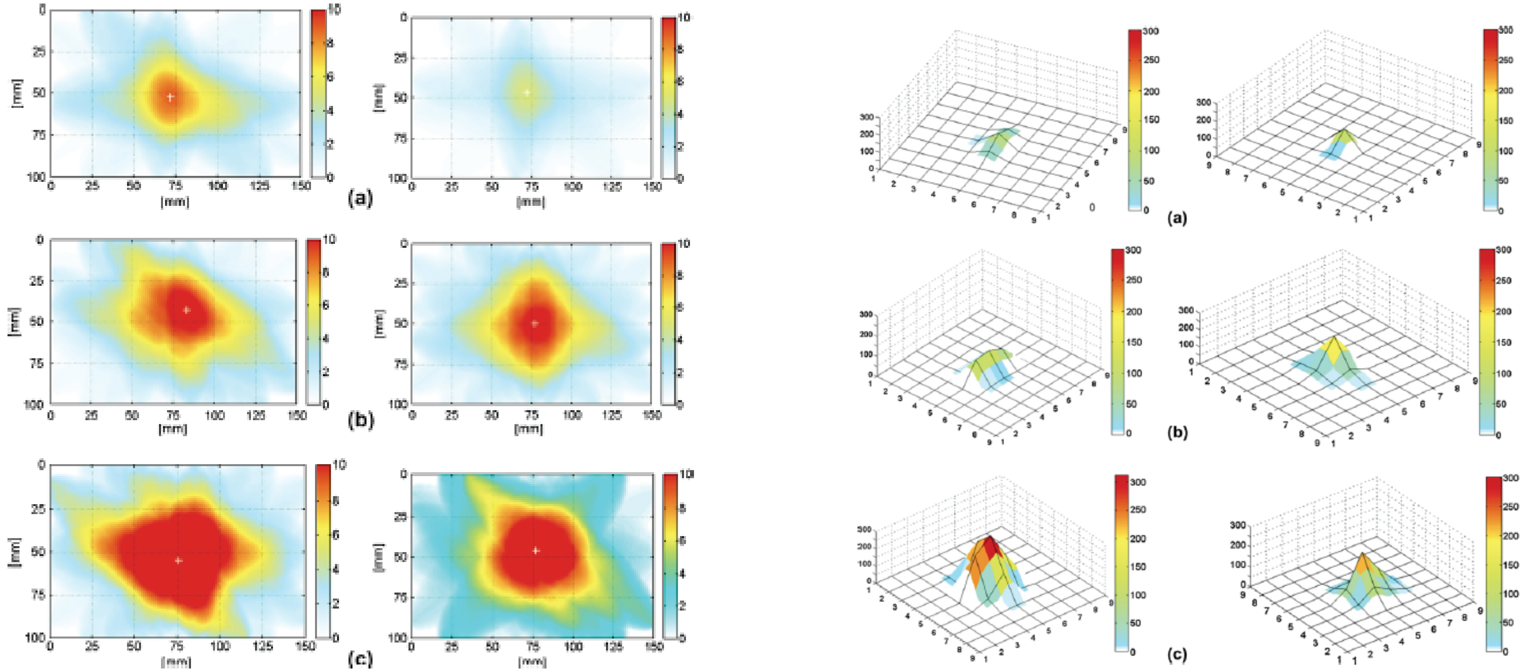

(b) In-plane measurement damage profile

(d) Through thickness damage profile

Figure 2.7: Electrode patterns and the obtained resistance change map [4]

for drilled hole, through-thickness notch, induced interlaminar damage. Apart from the conductivity map, the location and size of damage was identified through the two damage indicators. Good correlation between the damage and conductivity change maps is observed.

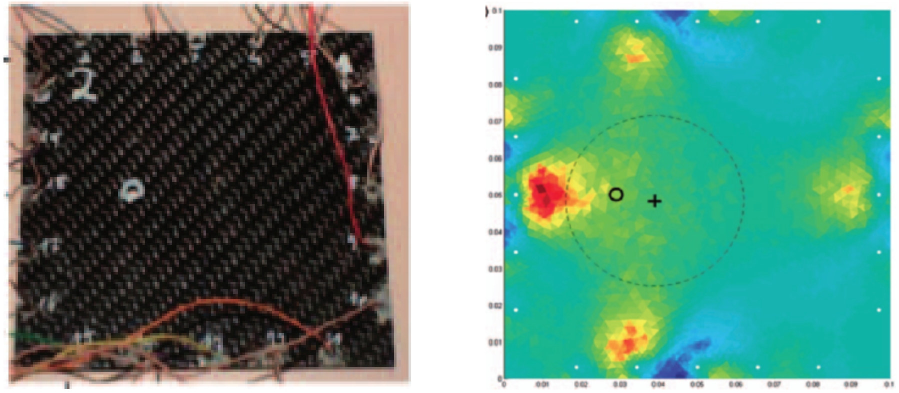

(a) Hole in a woven composite and reconstructed conductivity

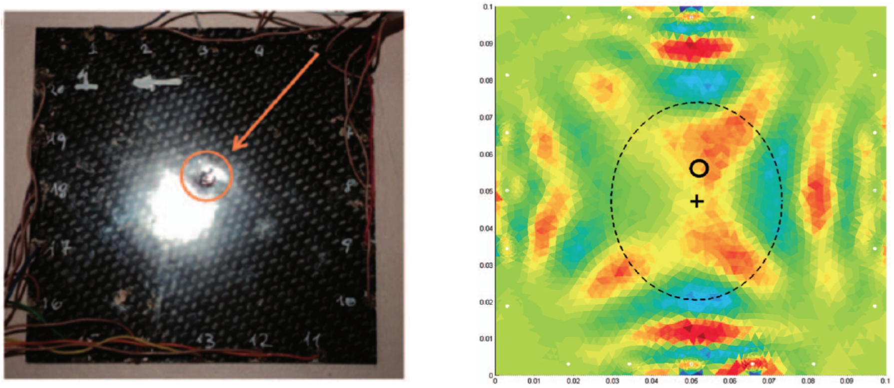

(b) Indentation in a woven composite and reconstructed conductivity

Figure 2.8: Experimental configuration and the reconstructed results for the different damage modes [5]

The latest work by [6] uses 6 X 6 array of electrodes on the top surface of a CFRP laminate to identify delamination and transverse cracks. Each electrode had a size of 15mm X 15mm and were placed 8mm apart. The electrodes were placed at an angle of 45° to the fiber direction. The anisotropic conductivity was accounted for in solving the forward problem. The conductivity was reconstructed for 4 different kinds of damage namely: small hole, two holes, transverse crack and a diagonal crack. Different excitation modes as shown in Fig. 2.9 (a) were compared on several quality metrics. Conductivity of the mid layer was reconstructed from the measurements. Based on their analysis, current injection between the farthest electrodes provided better reconstruction results. The geometry, injection patterns and the reconstructed conductivities for the different injection patterns are shown in Fig. 2.9.

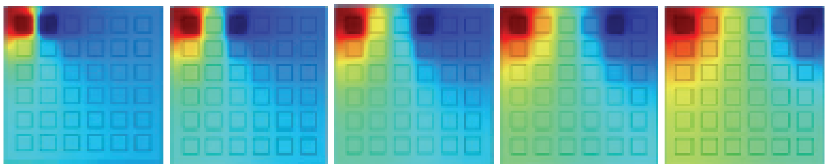

(a) Mode 1 (b) Mode 2 (c) Mode 3 (d) Mode 4 (e) Mode 5

(i) Different excitation modes

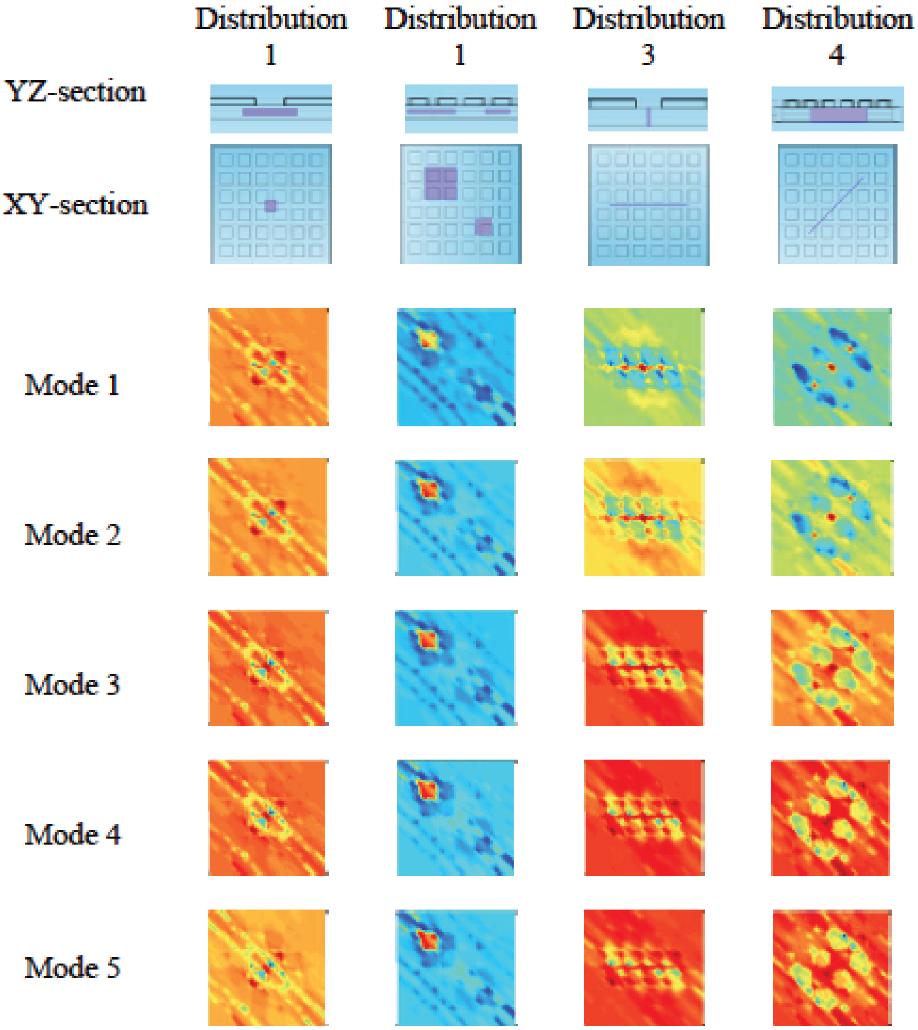

(ii) Damage modes and its reconstruction

Figure 2.9: Numerical configuration and the obtained conductivities for different modes of damage [6]

2.6 Problem statement and research objectives

To summarize, studies that focus on global behavior of the laminate has shown that electrical resistance measurements are sensitive to the different modes of damage. Scaling up, potential/resistance mapping methods have demonstrated the capability of the method to coarsely locate damage within the material. Studies using ET has shown its potential as a qualitative SHM technique that is scalable for real composite structures. However, ET based damage characterization is still in its infancy. Anisotropic conductivity reconstruction is still an active area of research. Identifying the type and quantifying the level of damage from a conductivity map is challenging and has not been attempted so far.

The complexity lies in the fact that observation of conductivity change at laminate level is implicitly connected to the different damage mechanisms that occur at the microscale, i.e., reconstructed conductivity at every local point is implicitly a homogenized representation of the different conductivity changing mechanisms in and around the point. However, the explicit relationship between the different mechanisms and macroscopic conductivity has not been established. Without bridging these two scales, the obtained conductivity map cannot be interpreted for damage. The absence of such a link has limited ET as a qualitative health monitoring technique. Parameters at various length scales can be effectively bridged through homogenization as shown in Fig. 2.10. Depending on the scales and mechanisms involved, different homogenization techniques can be used to connect the quantities of interest.

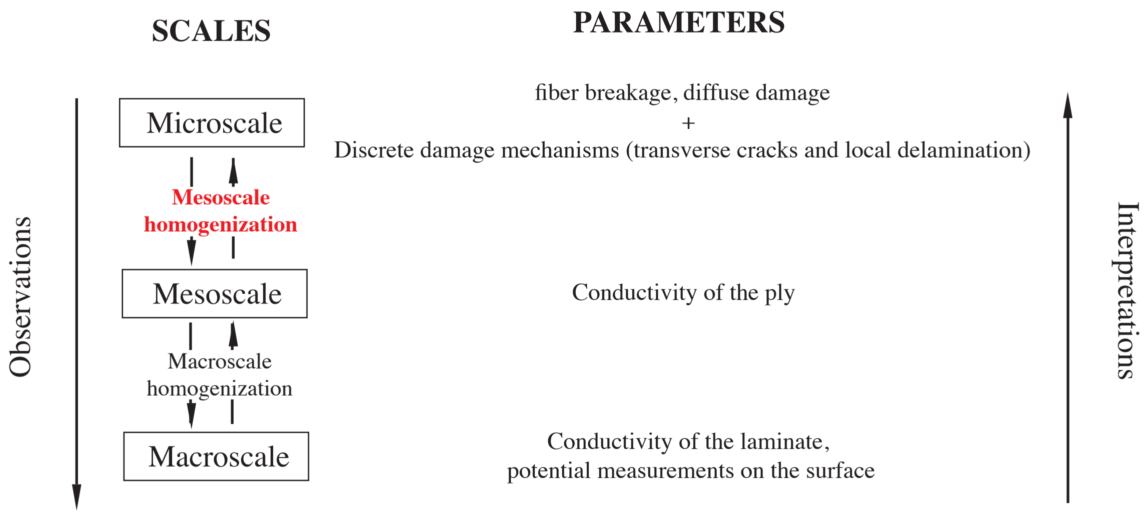

Figure 2.10: Different scales and observable parameters

In this work, we bridge the mesoscale conductivity to the discrete degradation mechanisms (transverse cracks and local delamination) in the ply through mesoscale homogenization. The primary questions we try to answer through this work, is (i) whether the effect of microscale damage on the electrical conductivity of the ply can be understood? (ii) if so, can this relation be used to quantitatively identify the microscale damage at the ply level? With these major goals in mind, the work will focus on the following objectives and related tasks:

1. *Objective:* Bridging microscale discrete damage mechanisms to the electrical behavior at the mesoscale

   This will be done through mesoscale electrical homogenization. The homogenization is carried out for two discrete microscale damage mechanisms: transverse cracking and local delamination. Through this study, an understanding of the effect of transverse cracks and local delamination on conductivity variation at ply level is obtained. The method outlined in this thesis is inspired by the work on mesoscale homogenization of mechanical properties of laminated composites [86] and will be extended to homogenization of electrical behavior. The obtained insights are then used to identify transverse cracks in composite laminates through electrical tomography. Subsequent part of the work focuses on presenting a mesoscale homogenization based regularization method for electrical tomography problem to detect transverse cracks.

2. *Objective:* Perform a sensitivity analysis on transverse cracking mechanism

   A generalized study is performed to understand how the various geometrical and material parameters of composite laminates affect the sensitivity of the voltage measurements towards transverse cracks. Then the optimal electrode network design for tracking transverse cracks using electrical tomography is presented.

3. *Objective:* Demonstrate the performance of Mesoscale homogenization guided electrical tomography

   Based on mesoscale homogenization results, we develop a surrogate/equivalent model that is representative of the cracked laminate and consequently reconstruct the mesoscale conductivity using a reduced basis method. This is a preliminary work to show the potential of such homogenization techniques in their applications to electrical tomography.

Chapter 3

Electrical mesomodel

Abstract

The missing link between the various complex degradation mechanisms within the laminate and continuum conductivity prevents ET from being used as a quantitative technique. This link is also needed to validate/justify the use of macroscopic measurements towards the identification of damage at the ply level. An electrical mesomodel that can establish this link between the various microscale degradations and the conductivity is proposed. The mesoscale homogenization of transverse cracks with local delamination of the ply is first described for in-plane electrical loading for both the outer and the inner plies. The mesoscale model is then extended to include the out-of-plane loading. The relationship between the mesoscale damage indicators and the degradation morphology is identified for various scenarios. These damage indicators are found to be intrinsic to the ply. The effect of crack closure, resin rich interlayer, and various anisotropy levels on the damage indicator is identified. As such, this defines the first step towards the interpretation of resistivity measurement in terms of micromechanical damage.

3.1 Introduction

Microscale models of various degradation mechanisms by considering every single cracked area are expensive, complex and not meaningful in that these often do not aid in the design of structures at the macroscale. Various multi-scale strategies have been developed to create models that work on scales that are meaningful to compute but at the same time derive physical meaning from the behavior at the microscale. One such technique is the damage mesomodel [87] for laminates where the scale of homogenization is the ply. The main points of mesoscale homogenization are that 1) it provides a continuous representation of discrete damage at a higher scale through damage indicators and 2) the damage indicators are intrinsic (i.e. they directly quantify the degradation state of the ply but do not depend on the lamination parameters such as orientation or thickness). Previous work has connected the mechanical damage indicators at the ply level to the micro description of the various damage mechanisms [88, 18, 86, 12, 89]. These indicators were found to be intrinsic, and hence the various damage mechanisms can be modeled independently of the stacking sequence and the material.

In this work, we adapt the concept of homogenization to the construction of mesoscale electrical behavior. Such a description can aid in understanding the conductivity obtained from electrical tomography. In [88, 18, 86, 12, 89], the microscale solution was homogenized to obtain the meso damage indicators under the condition of equal strain energy between the two scales. Here, the same idea of homogenization based on the condition of obtaining the same electrical energy on the two scales is considered. The objective is to define an energetically equivalent ply with a modified conductivity as shown in Fig. 3.2. The basic idea of the mesomodel is that the behavior of the laminate is derived from the two elementary constituents: the ply and the interface. Fiber breaking, diffuse damage and transverse cracks are the degradation mechanisms in the single ply whereas local delamination, diffuse delamination and macroscopic delamination represent the degradation in the interface. The effect of each intralaminar mechanism can then be equivalently represented at the mesoscale (ply level) through the mesoscale homogenization. The procedure and the relationships are detailed in the following sections.

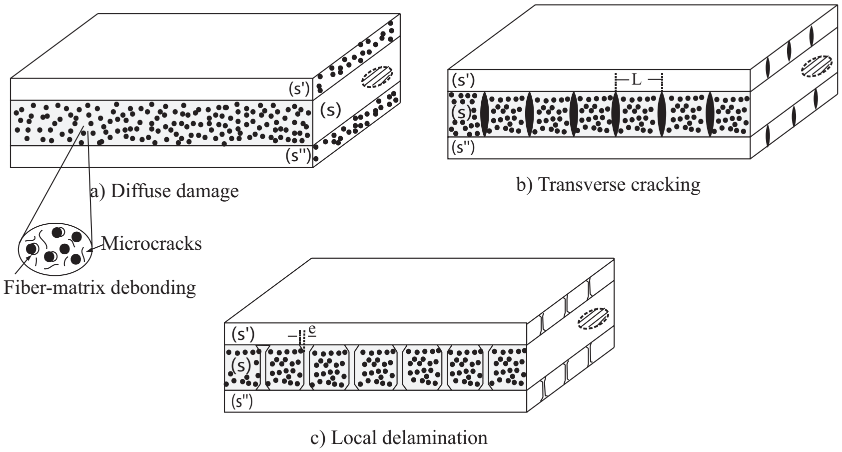

a) Diffuse damage

b) Transverse cracking

c) Local delamination

Figure 3.1: Different damage scenarios

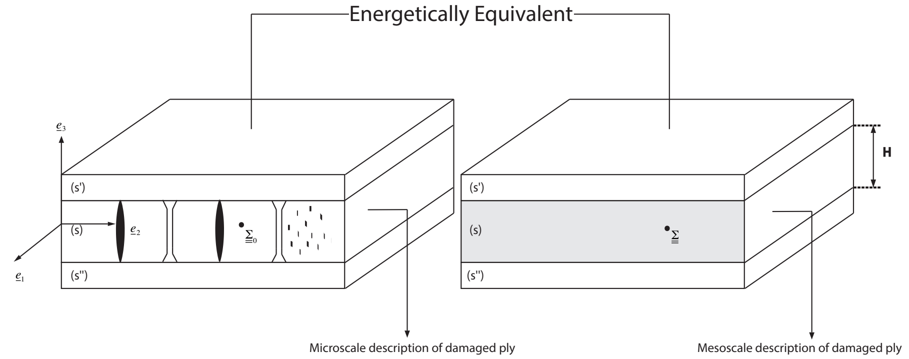

Figure 3.2: Micro-meso equivalence

3.2 Electrical solution of undamaged ply

Let Ω be the laminate under consideration consisting of three sub-domains S', S'' and S. The fiber orientation of the middle ply S is $\underline{e}_1$. When loaded by the electric field $\underline{\bar{E}}$ which is the gradient of the electric potential $\bar{U}$, given by

$$\underline{\bar{E}} = -\underline{\nabla}\bar{U}; \underline{\bar{E}} = \bar{E}_1\underline{e}_1 + \bar{E}_2\underline{e}_2 + \bar{E}_3\underline{e}_3$$

the current density can be obtained by solving the constitutive equation

$$\underline{\bar{J}} = \underline{\underline{\Sigma}}_0.\underline{\bar{E}}$$

where

$$\underline{\underline{\Sigma}}_0 = \Sigma^0_{11}\underline{e}_1 \otimes \underline{e}_1 + \Sigma^0_{22}\underline{e}_2 \otimes \underline{e}_2 + \Sigma^0_{33}\underline{e}_3 \otimes \underline{e}_3$$

defines the local orthotropic conductivity of the ply. The electrical energy of the ply S can be written as

$$EE = \frac{1}{2}\int_S \underline{J}.\underline{E}dS = \frac{1}{2}\int_S \underline{E}.\underline{\underline{\Sigma}}_0.\underline{E}dS$$

3.3 Description of fiber breakage

In the mesoscale the fiber breakage can be treated as naturally homogenized as they occur on a much smaller scale. It is evident that the damage due to fiber breakage primarily affects the conductivity in the fiber direction. Thus the electrical energy of the ply S damaged along the fibers alone can be written as

$$EE = \frac{1}{2}\int_S \underline{E}.\underline{\underline{\Sigma}}.\underline{E}dS$$

where

$$\underline{\underline{\Sigma}} = \Sigma^0_{11}(1-d_f)\underline{e}_1 \otimes \underline{e}_1 + \Sigma^0_{22}\underline{e}_2 \otimes \underline{e}_2 + \Sigma^0_{33}\underline{e}_3 \otimes \underline{e}_3$$

Here the damage due to fiber breakage is quantified by the damage indictor d_f. Mechanically, the damage due to fiber breakage is brittle in nature, and assumes a binary evolution. We start with a simple assumption that d_f undergoes a similar evolution. Thus we can write the modified conductivity tensor as

$$\underline{\underline{\Sigma}} = \Sigma^0_{11}(1-d_f)\underline{e}_1 \otimes \underline{e}_1 + \Sigma^0_{22}\underline{e}_2 \otimes \underline{e}_2 + \Sigma^0_{33}\underline{e}_3 \otimes \underline{e}_3$$

3.4 Description of diffuse damage

Damage due to diffuse damage occurs primarily due to matrix-fiber debonding and modifies both the transverse and the through-thickness conductivities. Similar to the fiber breakage, the diffuse damage is considered as naturally homogenized because of the very small scale at which it occurs. The modification of the electrical energy due to diffuse damage can be quantified through the damage indicator $\tilde{d}, 0 \geq \tilde{d} \leq 1$, which operates on the conductivity matrix as

$$\underline{\underline{\Sigma}} = \Sigma^0_{11}\underline{e}_1 \otimes \underline{e}_1 + \Sigma^0_{22}(1-\tilde{d})\underline{e}_2 \otimes \underline{e}_2 + \Sigma^0_{33}(1-\tilde{d})\underline{e}_3 \otimes \underline{e}_3$$

Thus the electrical energy of ply S is given by

$$EE = \frac{1}{2}\begin{bmatrix} E_1 \\ E_2 \\ E_3 \end{bmatrix} \begin{bmatrix} \Sigma^0_{11} & 0 & 0 \\ 0 & \Sigma^0_{22}(1-\tilde{d}) & 0 \\ 0 & 0 & \Sigma^0_{33}(1-\tilde{d}) \end{bmatrix} \begin{bmatrix} E_1 \\ E_2 \\ E_3 \end{bmatrix}$$

3.5 Mesoscale homogenization of discrete damage mechanisms

Mesoscale homogenization is now performed for two discrete damage mechanisms, namely, transverse cracks and local delamination. We consider that the central ply S is degraded by a periodical network of transverse cracks and local delamination. The density of transverse cracks is denoted by dimensionless cracking density, ρ which is given by:

$$\rho = \frac{H}{L} \tag{3.1}$$

where H is the thickness of the cracked ply and L is the length between two periodic cracks, as shown in Fig. 3.1. The local delamination length is represented by dimensionless delamination length, τ which is given as:

$$\tau = \frac{e}{H} \tag{3.2}$$

where e is the length of the delamination at the tip of the transverse crack as shown in Fig. 3.1.

We consider that the laminate is subjected to a macroscopic in-plane electrical loading. So the electrical field in the laminate can be considered as

$$\underline{\bar{E}} = \bar{E}_1 \underline{e}_1 + \bar{E}_2 \underline{e}_2 \tag{3.3}$$

For a non-damaged laminate, $\underline{\bar{E}}$ is constant in the $\underline{e}_3$ direction. The dual variable $\underline{\bar{J}}$ (flux of current density) is constant within each ply. We now study the structure of the problem when degradation develops in plies while the structure is loaded by

$\bar{\underline{E}}$. A systematic homogenization is then performed at the mesoscale.

3.5.1 Electrical micro-meso homogenization: case of inner ply

The problem being linear, the solution $(U, \underline{E}, \underline{J})$ of the degraded laminate is the superposition of the effective solution $(\bar{U}, \bar{\underline{E}}, \bar{\underline{J}})$ with a periodic correction $(\tilde{U}, \tilde{\underline{E}}, \tilde{\underline{J}})$, so the exact electrical field can be reconstructed as (fig. 3.3)

$$\underline{E} = \bar{\underline{E}} + \tilde{\underline{E}} \tag{3.4}$$

with

$$\langle \tilde{\underline{E}} \rangle_\Omega = \underline{0} \tag{3.5}$$

$\langle . \rangle_\Omega$ denotes the average over the periodical cell used as support for calculating the periodical correction.

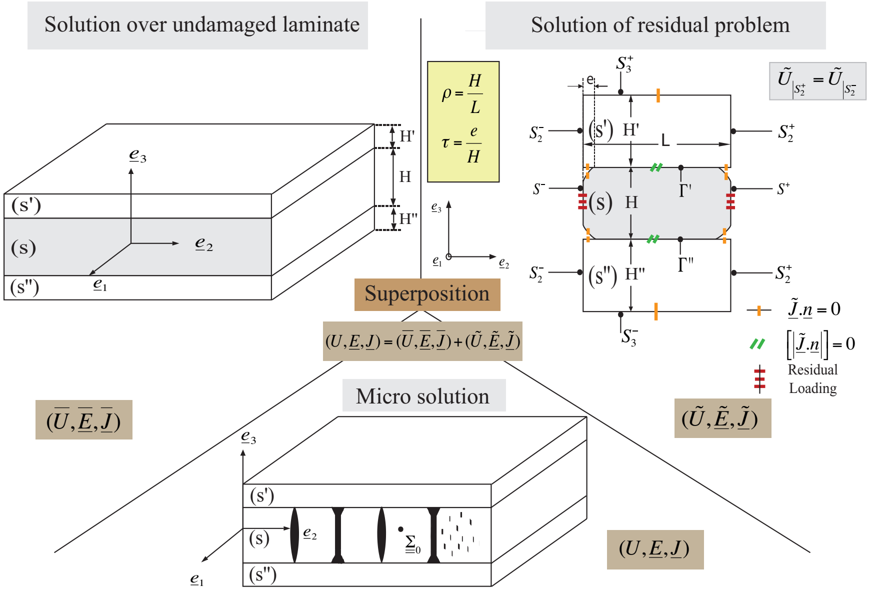

Figure 3.3: Decomposition of the exact solution over the cracked laminate for homogenization process

The residual problem

The periodical cell is bounded by the two periodic transverse cracks in the $\underline{e}_2$ direction. The residual problem gives the correction $(\tilde{U}, \underline{\tilde{E}}, \underline{\tilde{J}})$ to be added to the original solution to recover the flux free condition over the crack surfaces. This is done by imposing a boundary current flux over the cracks that is equal in magnitude and opposite to the effective flux. On the other boundaries, periodic boundary conditions are imposed, so the electric potential field belongs to the space of periodic electric potential fields denoted by U_{per}. The residual problem is defined for a general laminate with boundary conditions as shown in fig.3.3.

To find $(\tilde{U}, \underline{\tilde{E}}, \underline{\tilde{J}})$ at any point $\underline{M}$ such that:

- *Kinematic admissibility conditions:*

  $\underline{\tilde{E}} = -\nabla\tilde{U}, \qquad \forall\underline{M} \in \Omega$ (Compatibility condition)

  $\tilde{U} \in U_{per}$ (Periodicity conditions)

- *Static admissibility conditions:*

  $div\underline{\tilde{J}} = 0 \qquad \forall\underline{M} \in \Omega$ (Interior equilibrium equation)

  $\underline{\tilde{J}} \cdot \underline{n} = 0, \qquad \forall\underline{M} \in S_3^+ \cup S_3^- \cup (delamination\, crack\, surface)$(Free boundaries)

  $[|\underline{\tilde{J}} \cdot \underline{n}|] = 0, \qquad \forall\underline{M} \in \Gamma', \Gamma''$ (Continuity across the interfaces)

  $\underline{\tilde{J}} \cdot \underline{n} = -\underline{\bar{J}} \cdot \underline{n}, \qquad \forall\underline{M} \in S^+ \cup S^-$ (Residual loading)

- *Constitutive equation:*

  $\underline{\tilde{J}} = \underline{\underline{\Sigma}}_0(\underline{M}) \cdot \underline{\tilde{E}}, \qquad \forall\underline{M} \in \Omega$ (Constitutive equation)

Homogenization

Considering the periodical cell, the electrical energy can be given as:

$$EE = \frac{1}{2}\int_\Omega \underline{J} \cdot \underline{E} d\Omega = \frac{1}{2}\int_\Omega \underline{E} \cdot \underline{\underline{\Sigma}}_0 \cdot \underline{E} d\Omega \tag{3.6}$$

where

$$\underline{\underline{\Sigma}}_0 = \Sigma^0_{11}\underline{e}_1 \otimes \underline{e}_1 + \Sigma^0_{22}\underline{e}_2 \otimes \underline{e}_2 + \Sigma^0_{33}\underline{e}_3 \otimes \underline{e}_3 \tag{3.7}$$

defines the local orthotropic conductivity of the ply. Writing the electric field in terms of the partition introduced earlier in (3.4), we get:

$$EE = \frac{1}{2}\int_{\Omega}(\underline{\bar{E}}+\underline{\tilde{E}})\cdot\underline{\underline{\Sigma}}_0\cdot(\underline{\bar{E}}+\underline{\tilde{E}})d\Omega = \frac{1}{2}\int_{\Omega}\underline{\bar{E}}.\underline{\underline{\Sigma}}_0\cdot\underline{\bar{E}}d\Omega+\frac{1}{2}\int_{\Omega}\underline{\tilde{E}}\cdot\underline{\underline{\Sigma}}_0\cdot\underline{\tilde{E}}d\Omega+\int_{\Omega}\underline{\bar{E}}\cdot\underline{\underline{\Sigma}}_0\cdot\underline{\tilde{E}}d\Omega \tag{3.8}$$

For a system with no internal current source, the equilibrium equation can be given as:

$$div\underline{J} = 0 \tag{3.9}$$

The weak form of the equilibrium equation, is given as:

$$\int_{\Omega} U^* \cdot div\underline{J}d\Omega = 0 \ \forall U^* \tag{3.10}$$

$$\int_{\partial\Omega} U^* \cdot \underline{J} \cdot \underline{n}ds - \int_{\Omega} \underline{J} \cdot \underline{\nabla} U^* d\Omega = 0 \ \forall U^* \tag{3.11}$$

$\int_{\partial\Omega} U^* \cdot \underline{J} \cdot \underline{n}ds = 0$ due to periodicity and by choosing $U^* = \tilde{U}$ we get:

$$\int_{\Omega} \tilde{E} \cdot \underline{\underline{\Sigma}}_0 \cdot (\underline{\bar{E}} + \underline{\tilde{E}})d\Omega = 0 \tag{3.12}$$

Introducing (3.12) in (3.8) we directly get:

$$EE = \frac{1}{2}\int_{S'}\underline{\bar{E}}\cdot\underline{\underline{\Sigma}}_0\cdot\underline{\bar{E}}dS'+\frac{1}{2}\int_{S''}\underline{\bar{E}}\cdot\underline{\underline{\Sigma}}_0\cdot\underline{\bar{E}}dS''+\frac{1}{2}\int_{S}\underline{\bar{E}}\cdot\underline{\underline{\Sigma}}_0\cdot\underline{\bar{E}}dS-\frac{1}{2}\int_{\Omega}\underline{\tilde{E}}\cdot\underline{\underline{\Sigma}}_0\cdot\underline{\tilde{E}}d\Omega \tag{3.13}$$

Since we consider linearity, the solution of the residual problem is linear with respect to the loading. Thus, the term $\int_{\Omega} \underline{\tilde{E}} \cdot \underline{\underline{\Sigma}}_0 \cdot \underline{\tilde{E}}d\Omega$ can be recast as

$$\int_{\Omega} \underline{\tilde{E}} \cdot \underline{\underline{\Sigma}}_0 \cdot \underline{\tilde{E}} d\Omega = |S| \underline{\bar{E}} \cdot (\tilde{\Sigma}_{22} \underline{e}_2 \otimes \underline{e}_2) \cdot \underline{\bar{E}} \tag{3.14}$$

where $\tilde{\Sigma}_{22}$ is the effective conductivity of periodic cell whose value can be obtained from the solution of the residual problem. Hence from (3.13) and (3.14) the electrical energy becomes:

$$EE = \frac{1}{2} \int_{S'} \underline{\bar{E}} \cdot \underline{\underline{\Sigma}}_0 \cdot \underline{\bar{E}} dS' + \frac{1}{2} \int_{S''} \underline{\bar{E}} \cdot \underline{\underline{\Sigma}}_0 \cdot \underline{\bar{E}} dS'' + \frac{1}{2} \int_{S} \underline{\bar{E}} \cdot \underline{\underline{\Sigma}} \cdot \underline{\bar{E}} dS \tag{3.15}$$

where

$$\underline{\underline{\Sigma}} = \underline{\underline{\Sigma}}_0 - \tilde{\Sigma}_{22} \underline{e}_2 \otimes \underline{e}_2 \tag{3.16}$$

This depicts the total energy of the laminate with a modified equivalent conductivity tensor that effectively homogenizes the cracked ply at the mesoscale. This change in conductivity can be quantified using a mesoscale damage indicator d_2^e defined as:

$$d_2^e = \frac{\tilde{\Sigma}_{22}}{\Sigma_{22}^0} \tag{3.17}$$

Now the conductivity tensor can be expressed as:

$$\underline{\underline{\Sigma}} = \Sigma_{11}^0 \underline{e}_1 \otimes \underline{e}_1 + (1 - d_2^e) \Sigma_{22}^0 \underline{e}_2 \otimes \underline{e}_2 + \Sigma_{33}^0 \underline{e}_3 \otimes \underline{e}_3 \tag{3.18}$$

Considering $\underline{\bar{J}} = \underline{\underline{\Sigma}}_0 \cdot \underline{\bar{E}}$ to be the current flux through the uncracked ply S. Then the effective flux over the cracks in the periodic cell can be taken as $\underline{\bar{J}} \cdot \underline{n} = \underline{\underline{\Sigma}}_0 \cdot \underline{\bar{E}} \cdot \underline{n}$. Since the unit normal vector to the cracks is $\underline{e}_2$, the effective flux becomes $\underline{\bar{J}} \cdot \underline{e}_2 = \underline{\underline{\Sigma}}_0 \cdot \underline{\bar{E}} \cdot \underline{e}_2$. Using this relationship in (3.14), and by reshaping it, d_2^e can be evaluated from the residual problem as:

$$d_2^e = \frac{\Sigma_{22}^0}{\mid S \mid (\underline{\bar{J}} \cdot \underline{e}_2)^2} \int_\Omega \underline{\tilde{E}} \cdot \underline{\underline{\Sigma}}_0 \cdot \underline{\tilde{E}} d\Omega \tag{3.19}$$

Solving the residual problem

The residual problem is solved using COMSOL Multiphysics. As a first example to illustrate the effect of local delamination on resistivity damage, a cross-ply laminate ($H = H' = H'' = 250.10^{-6}$m) is considered. The dimension of the cell about direction $\underline{e}_2$ depends on the dimensionless cracking density via $L = H/\rho$, while its dimension about the direction $\underline{e}_3$ is arbitrary. The non-damaged conductivity matrix is the same for each ply in its basis of orthotropy:

$$\underline{\underline{\Sigma}}_0 = \begin{bmatrix} 5500 & 0 & 0 \\ 0 & 203.5 & 0 \\ 0 & 0 & 20.4 \end{bmatrix} S/m$$

The geometry is discretized using Lagrange quadratic elements. A systematic convergence study has been performed for the total energy of the problem to carefully ensure results were accurate. As a final choice, a constant element size of 10×10^6 m has been used about $\underline{e}_2$ and $\underline{e}_3$ directions for all crack densities. Only one element is necessary about $\underline{e}_1$ direction as all fields (electrical field, electrical potential and current density) do not depend on the x-coordinate (cracks being infinite about this direction). All presented results are at convergence and can be considered as mesh independent. The linear system is solved using conjugate gradient solver.

The damage indicator for various (ρ, τ) configurations is shown in Fig. 3.4. The baseline curve ($\tau = 0$) corresponds to the damage due to transverse cracking alone and is consistent with the one already proposed by [90]. The growth of local delamination shows an upward shift of the damage curve, and the damage reaches unity when the delamination length reaches the length of the periodical cell. When transverse cracks occur, the ply transfers the electrical energy through the surrounding plies. Now, when the delamination length spans through the entire interface, this channel is disrupted, leading to complete conductive failure of the ply. We introduce a normalized dimensionless quantity $\rho/(1-2\rho\tau)$ which denotes the ratio of the effective length of the cracked cell (i.e. excluding the length of delamination) to the thickness of the ply. The damage parameter is found to be intrinsic to this quantity as can be seen in Fig. 3.5.

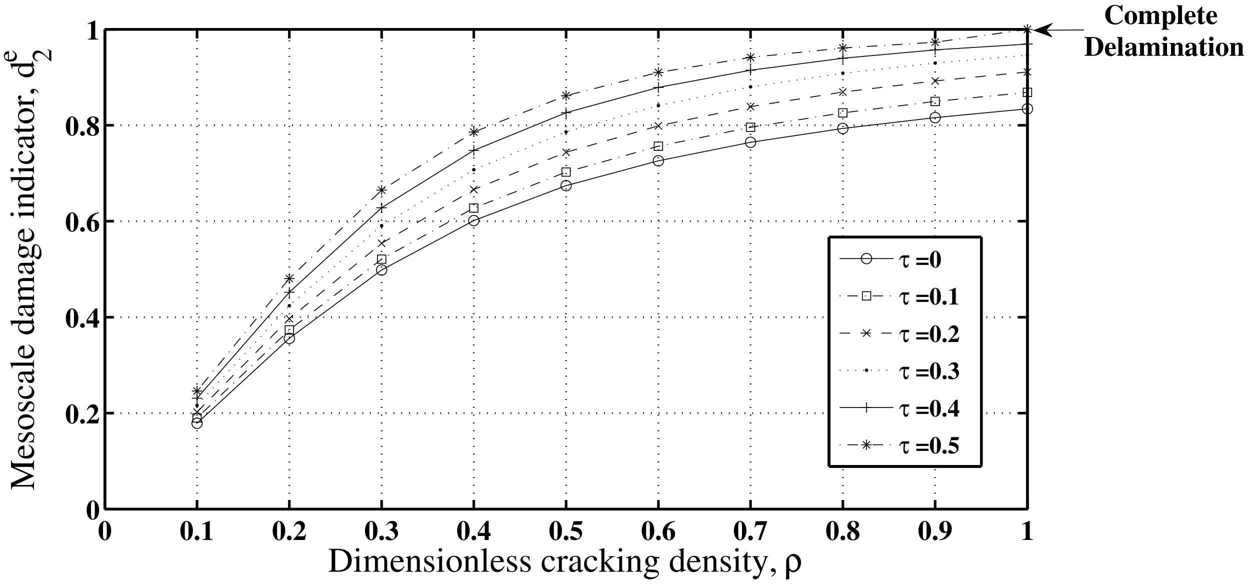

Figure 3.4: Variation of damage indicator with transverse cracks and local delamination in inner ply

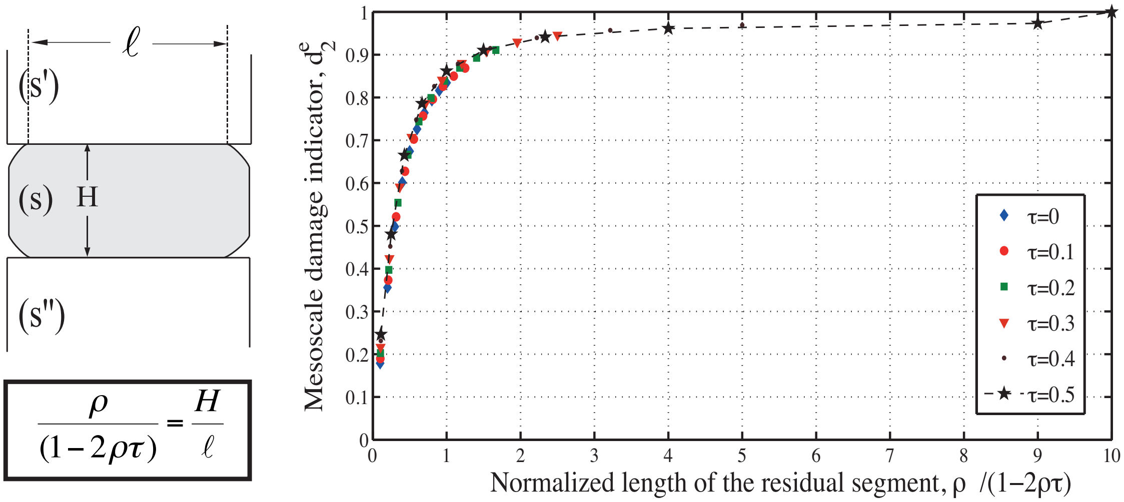

Figure 3.5: Variation of damage indicator with normalized effective length of the inner ply

3.5.2 Electrical micro-meso homogenization: case of outer plies

We now have a quick look at the homogenization results in the case of cracked outer plies. A similar homogenization process can be used, provided we are using the periodical cell defined in Fig. 3.6. Note that for outer plies, we introduce a different definition of ρ and τ:

$$\rho = \frac{2H}{L}; \tau = \frac{e}{2H} \tag{3.20}$$

to take advantage of the classical observation in mechanical homogenization (from a mechanical point of view, an outer ply behaves similarly to an inner ply with double thickness, and we intend to explore if the same conclusion is true for the electrical homogenization [12]).

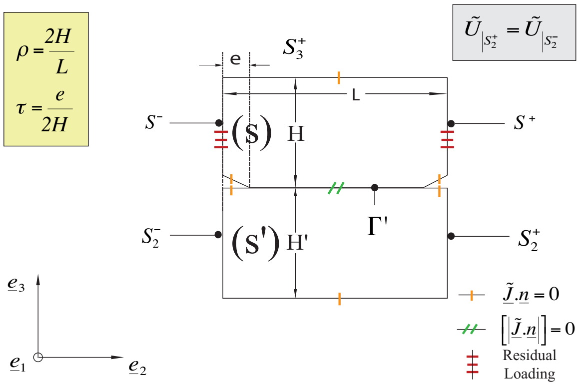

Figure 3.6: Periodic cell with boundary conditions for transverse cracks with local delamination in outer plies

Fig. 3.7 shows the damage levels for increasing cracking density and delamination lengths on the outer plies. It can be seen that they show similar trends as the inner plies.

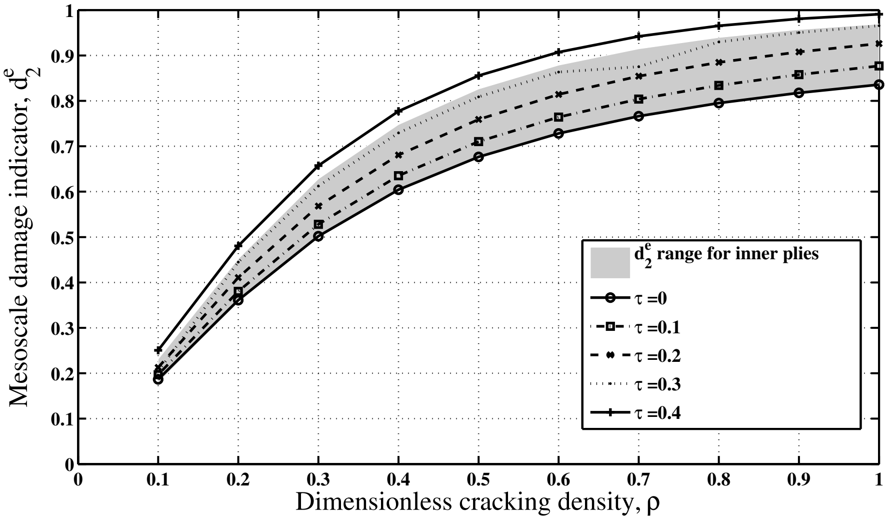

Figure 3.7: Damage indicator for transverse cracks with various delamination lengths on outer plies

3.5.3 Intrinsic property

By the definition of the damage parameter (3.19), one can see that it is dependent on the micro degradation (ρ, τ), the constitutive parameters of the material, and the geometry of the ply and the surrounding plies. But for the indicator to provide a mesoscale description, it must be independent of the influence of the parameters of the surrounding plies. Thus, tests are conducted to establish the intrinsic nature of the damage indicator.

Influence of plies' thickness For inner plies, the thickness of the bottom and the top plies are varied as $H' = H'' = [0.5, 1, 2, 4, 8].H$ and the behavior of the damage variable are determined.

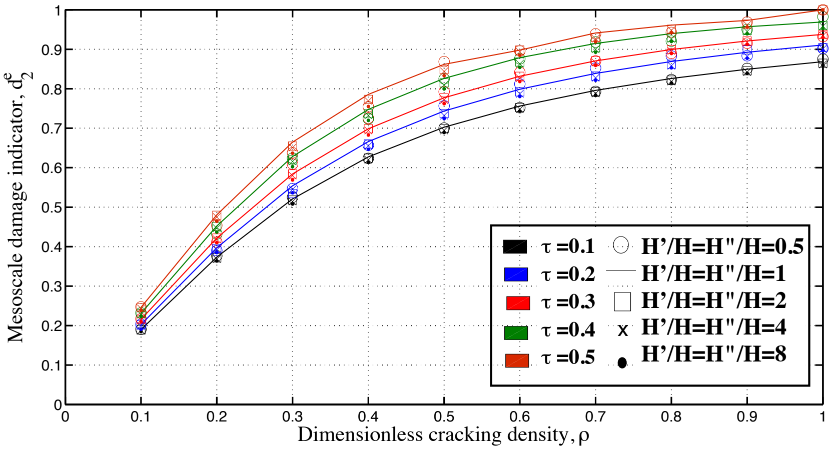

Figure 3.8: Influence of thickness of the outer plies on the damage indicator of degraded inner ply

Fig. 3.8 shows that the damage indicator is independent of the thickness of the surrounding plies. Similar independency is obtained, when the degradation is in the outer plies, with respect to the thickness of inner plies which is not reported here.

Influence of plies' orientation Similarly, in the case of degraded inner ply, the orientation of the two outer plies are varied as $\theta' \in [0°, 30°, 45°, 60°, 90°]$ and $\theta'' \in [0°, 30°, 45°, 60°, 90°]$. The profile of the damage for these various orientations shows

ρ	τ	d_{min}	d_{max}	Relative variation (%)
0.25	0.1	0.4524	0.5435	4.57
0.5	0.1	0.7025	0.76946	2.27
0.75	0.1	0.8118	0.85965	1.43
1	0.1	0.8685	0.90483	1.02
0.25	0.4	0.5476	0.65205	4.35
0.5	0.4	0.83613	0.87645	1.48
0.75	0.4	0.90483	0.9283	0.54
1	0.4	0.96918	0.97638	0.19

Table 3.1: Relative variation of damage indicator for various orientations of the adjacent plies for an inner ply with transverse cracks and local delamination

minimal relative variance (Table. 3.1) at various cracking states as can be seen in Fig. 3.9. Outer plies show similar independency when the orientation of the inner ply is varied as $\theta \in [0°, 30°, 45°, 60°, 90°]$. The relative variation over all the considered angle configurations is defined as:

$$\text{Relative variation (\%)} = \frac{d_{max} - d_{min}}{2(d_{max} + d_{min})} \times 100\% \tag{3.21}$$

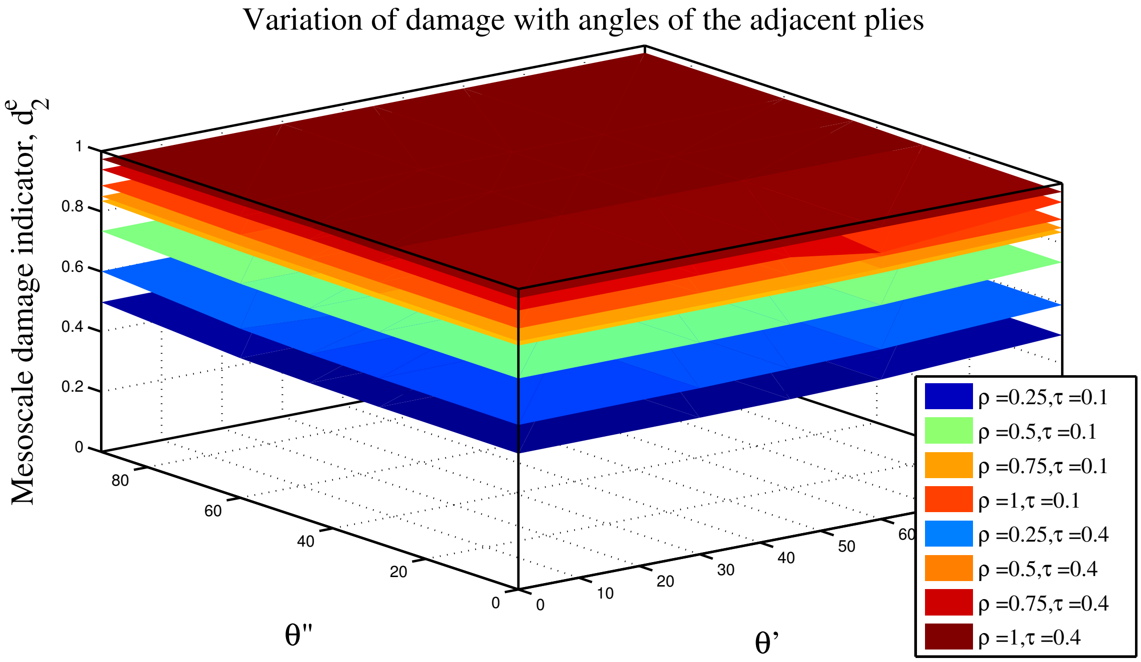

Figure 3.9: Influence of orientation of adjacent plies for an inner ply with transverse cracks and local delamination

3.5.4 Effect of diffuse damage

We have so far established the effect of transverse cracks and local delamination on the electrical damage indicator, d_2^e. The conductivity of the bulk material has always been taken as constant and equal to $\underline{\underline{\Sigma}}_0$. Yet, diffuse damage can also take place at the same time as transverse cracking and local delamination, leading to different conductivities of the plies.

We will address this point of the homogenization problem for inner plies (outer plies show similar behavior) with transverse cracks and no local delamination ($\tau = 0$). Adjacent parts (S') and (S'') still have the same reference conductivity $\underline{\underline{\Sigma}}_0$, but the conductivity of the central ply is taken to be dependent on diffuse damage. There is a paucity of information concerning the effect of diffuse damage on conductivity. For simplicity, we will retain the following form:

$$\underline{\underline{\Sigma}} = \Sigma^0_{11}\underline{e}_1 \otimes \underline{e}_1 + (1-\tilde{d})\Sigma^0_{22}\underline{e}_2 \otimes \underline{e}_2 + (1-\tilde{d})\Sigma^0_{33}\underline{e}_3 \otimes \underline{e}_3 \tag{3.22}$$

that assumes diffuse damage has no effect on Σ^0_{11} and has an isotropic effect in the transverse directions. A parametric study is conducted for $\tilde{d} = [0.05, 0.1, 0.15, 0.2, 0.25]$.

We see from Fig. 3.10 that the damage indicator d^e_2 is independent of the diffuse damage state within the ply.

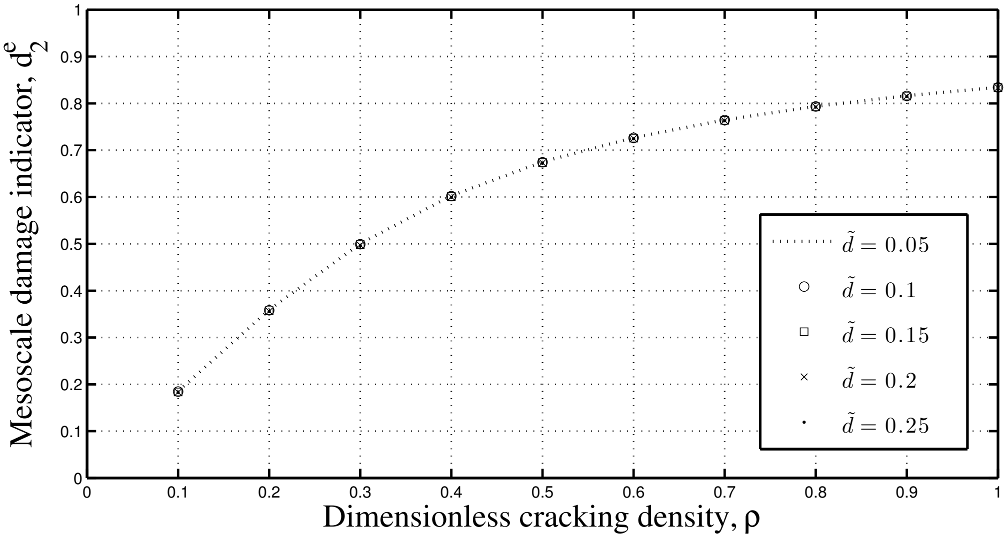

Figure 3.10: Evolution of d^e_2 with ρ for various diffuse damage states in inner ply

3.6 Mesoscale homogenization: extension to out-of-plane loading

In the earlier section we homogenized the effects of transverse cracking and local delamination for in-plane loading, and we proved that the mesoscale indicators are intrinsic. Now the effects of out-of-plane loading are considered. The laminate is loaded by the in-plane part $\underline{\underline{\pi}}.\underline{\bar{E}}$ of the macroscopic electrical field $\underline{\bar{E}}$ ($\underline{\underline{\pi}}$ is the projector over the plane $(\underline{e}_1, \underline{e}_2)$ defined as $\underline{\underline{\pi}} = \underline{e}_1 \otimes \underline{e}_1 + \underline{e}_2 \otimes \underline{e}_2$) and the out-of-plane part $\underline{\underline{\pi}}^{\perp}.\underline{\bar{J}}$ of the macroscopic current density ($\underline{\underline{\pi}}^{\perp} = \underline{\underline{1}} - \underline{\underline{\pi}}$). We start with obtaining the solution of the uncracked laminate and superimpose the solution from the two periodic residual problems (a) and (b). Once the total microsolution is obtained, the mesoscale solution is obtained by homogenization. The problems involved are defined as shown in Fig. 3.11.

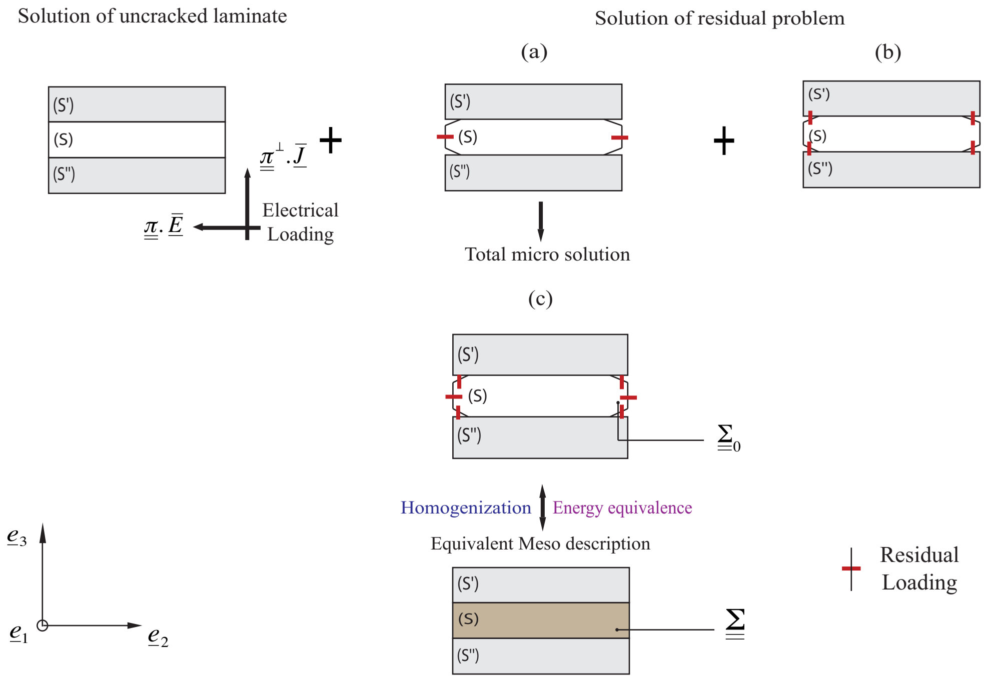

Figure 3.11: The basic ply problem

Homogenization

The homogenization is done as shown in section 3.5.1. The solution of the residual problem (c) can be written as:

$$\int_{\Omega} \underline{\tilde{E}}.\underline{\underline{\Sigma}}_0 \underline{\tilde{E}} d\Omega = |S| \underline{\bar{E}}.(\tilde{\Sigma}_{22} \underline{e}_2 \otimes \underline{e}_2 + \tilde{\Sigma}_{33} \underline{e}_3 \otimes \underline{e}_3 + \tilde{\Sigma}_{23} (\underline{e}_2 \otimes \underline{e}_3 + \underline{e}_3 \otimes \underline{e}_2)).\underline{\bar{E}} \tag{3.23}$$

where

$$\tilde{\Sigma}_{23}(\underline{e}_2 \otimes \underline{e}_3 + \underline{e}_3 \otimes \underline{e}_2) \tag{3.24}$$

represents the coupling between the two mechanisms. It should be noted that the $\underline{\bar{E}}$ is the one of the ply S as $\underline{\bar{E}}$ varies between the plies and is piecewise constant. The electrical energy can be given as:

$$EE = \frac{1}{2}\int_{S'} \underline{\bar{E}}.\underline{\underline{\Sigma}}_0.\underline{\bar{E}}dS' + \frac{1}{2}\int_{S''} \underline{\bar{E}}.\underline{\underline{\Sigma}}_0.\underline{\bar{E}}dS'' + \frac{1}{2}\int_{S} \underline{\bar{E}}.\underline{\underline{\Sigma}}.\underline{\bar{E}}dS \tag{3.25}$$

where

$$\underline{\underline{\Sigma}} = \underline{\underline{\Sigma}}_0 - (\tilde{\Sigma}_{22}\underline{e}_2 \otimes \underline{e}_2 + \tilde{\Sigma}_{33}\underline{e}_3 \otimes \underline{e}_3 + \tilde{\Sigma}_{23}(\underline{e}_2 \otimes \underline{e}_3 + \underline{e}_3 \otimes \underline{e}_2)) \tag{3.26}$$

We begin with a simple assumption that the coupling between the two mechanisms is negligible (this assumption will be validated later) and define the two mesoscale damage indicators given by:

$$d_2^e = \frac{\tilde{\Sigma}_{22}}{\Sigma_{22}^0}\,;\;\; d_3^e = \frac{\tilde{\Sigma}_{33}}{\Sigma_{33}^0} \tag{3.27}$$

Thus the modified mesoscale conductivity becomes:

$$\underline{\underline{\Sigma}} = \Sigma_{11}^0\underline{e}_1 \otimes \underline{e}_1 + (1 - d_2^e)\Sigma_{22}^0\underline{e}_2 \otimes \underline{e}_2 + (1 - d_3^e)\Sigma_{33}^0\underline{e}_3 \otimes \underline{e}_3 \tag{3.28}$$

d_2^e and d_3^e are calculated from the residual problems (a) and (b) respectively as:

$$d_2^e = \frac{\Sigma_{22}^0}{\mid S \mid (\underline{\bar{J}}.\underline{e}_2)^2}\int_{\Omega} \underline{\tilde{E}}.\underline{\underline{\Sigma}}_0.\underline{\tilde{E}}d\Omega\,;\;\; d_3^e = \frac{\Sigma_{33}^0}{\mid S \mid (\underline{\bar{J}}.\underline{e}_3)^2}\int_{\Omega} \underline{\tilde{E}}.\underline{\underline{\Sigma}}_0.\underline{\tilde{E}}d\Omega \tag{3.29}$$

Solving the residual problem

The residual problem (a) for the in-plane loading has already been discussed earlier (Section 3.5.1). The residual problem (b) for the out-of-plane loading is given as shown in Fig. 3.12 which solves for the damage indicator d_3^e. The evolution of the damage indicator for various delamination lengths and transverse cracking densities can be seen in Fig. 3.13. The damage value increases as the delamination length increases thereby decreasing the conductivity in the through-thickness direction. The increase in the transverse cracking density causes a shift in the damage curve for the same delamination lengths. This is due to the increase in the relative area of delamination. As expected, we observe complete damage for $\tau = 0.5$ and $\rho = 1$ denoting complete debonding. Again, we define a normalized quantity which is the ratio of the delamination length to the initial length of the interface, and find that this provides an intrinsic description of the damage indicator as seen in Fig. 3.14.

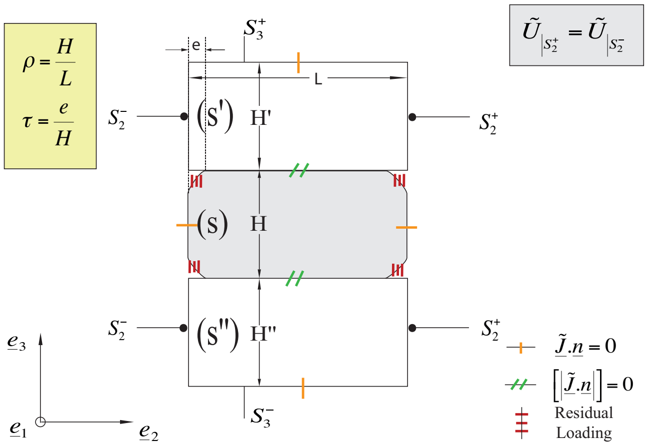

Figure 3.12: Residual problem for out-of-plane damage indicator

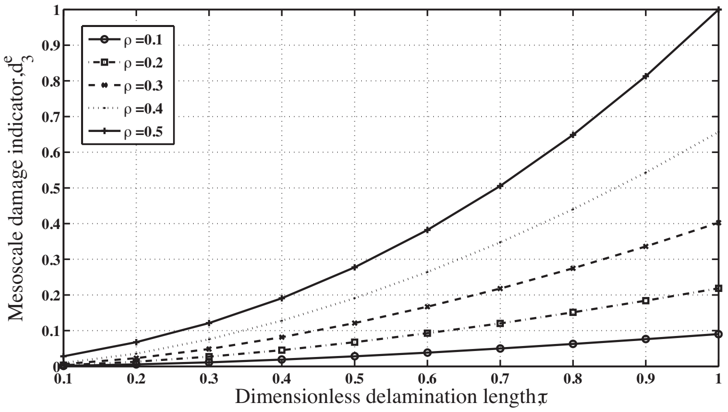

Figure 3.13: Variation of d_3^e as a function of τ for various ρ

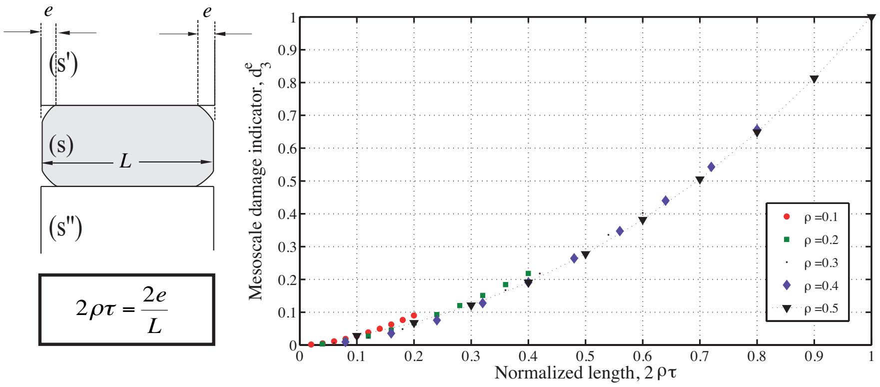

Figure 3.14: Variation of d_3^e with normalized length $2\rho\tau$

3.6.1 Intrinsic property

To check whether the damage indicator d_3^e is a ply-material indicator, we perform parametric studies varying the thickness $H' = H'' = [0.5, 1, 2, 4, 8].H$ and the orientation $\theta', \theta'' \in [0°, 30°, 45°, 60°, 90°]$ of the adjacent plies. Fig. 3.15 shows that the thickness of the adjacent plies does not contribute to the evolution of damage within the ply. Similarly, Fig. 3.16 shows that the damage indicator is independent of the orientation of the adjacent plies. The relative variation of the damage indicator for the various parameters is shown in Table 3.2.

3.6.2 Coupling effects

Earlier, we assumed negligible coupling effects between the two residual problems for simplicity. Now we will see if this assumption can be validated, by solving three residual problems:

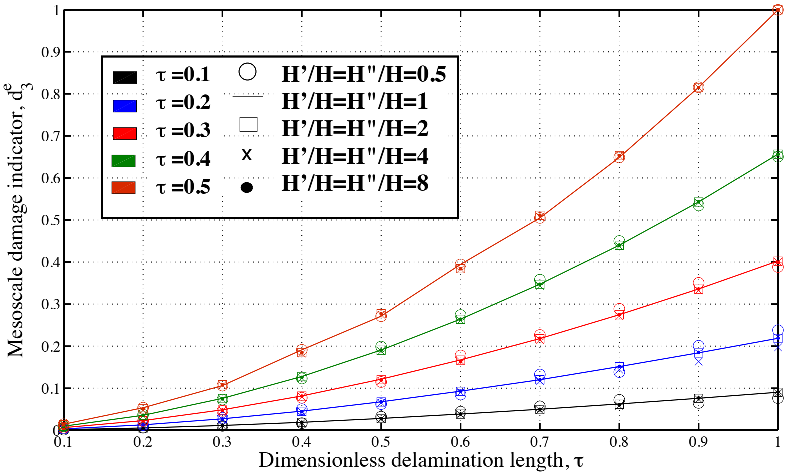

Figure 3.15: Evolution of d_3^e as a function of τ for various ρ and thickness of adjacent plies

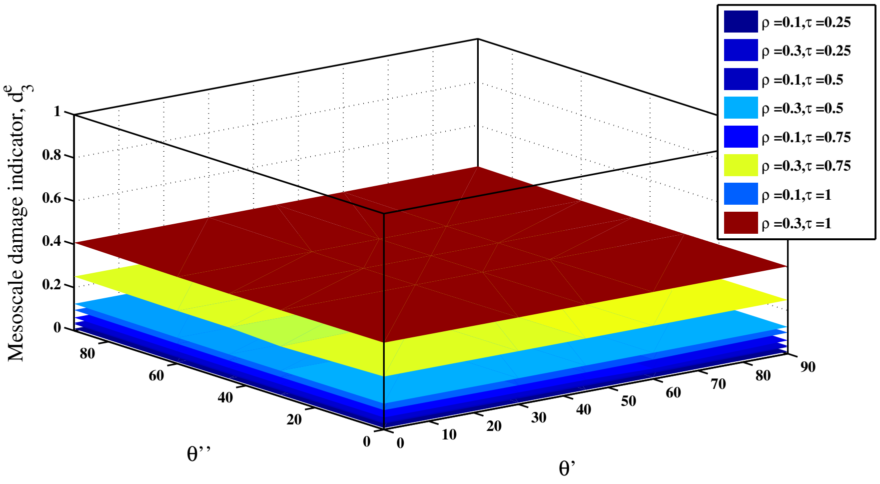

Figure 3.16: Variation of d_3^e with orientation of adjacent plies

a) The in-plane problem where the residual flux is in the $\underline{e}_2$ direction only

τ	ρ	d_{min}	d_{max}	Relative variation (%)
0.25	0.1	0.00796	0.01056	7.02
0.5	0.1	0.0279	0.0341	4.98
0.75	0.1	0.056	0.0657	3.9
1	0.1	0.0903	0.103	3.3
0.25	0.3	0.0344	0.0385	2.84
0.5	0.3	0.1207	0.1277	1.42
0.75	0.3	0.246	0.254	0.77
1	0.3	0.4025	0.4094	0.43

Table 3.2: Relative variation of d_3^e for various orientations of the adjacent plies

b) The out-of-plane problem where the residual flux is in the $\underset{\sim}{e}_3$ direction only

c) The coupled problem where both the in-plane and out-of-plane problem are solved together

The coupling effects can be neglected provided the difference between the electrical energy of the coupled problem (c) and the sum of energies of the other two residual problems (a+b) are negligible. The problem is solved for all τ keeping $\rho = 0.1$. The geometry and the boundary conditions are as mentioned in the earlier sections.

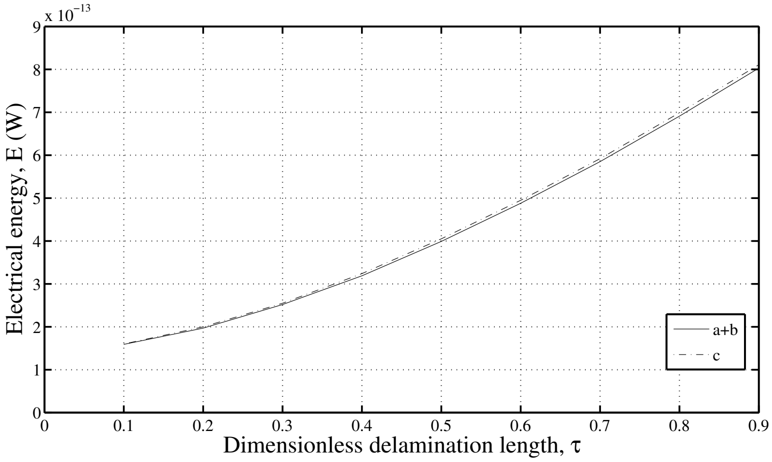

Figure 3.17: Electrical energy of the residual problems (a+b) and c

From Fig. 3.17, we can see that the difference is negligible. Thus the coupling effects are small and can be neglected, and the assumption of a diagonal homogenized conductivity operator (3.28) is validated. As in Section 3.5.4 , we finally perform a systematic study of the effect of diffuse damage on the damage indicator d_3^e. It is found that d_3^e does not depend on the level of diffuse damage in the plies.

3.7 Effect of ply conductivity

Parametric studies varying thickness and orientation of the surrounding plies have shown that the derived mesoscale relationship is intrinsic to the ply. The influence of the ply conductivity has not been investigated. Laminate families have highly varying conductivity based on the primary constituents of the laminate. This brings the question, whether the mesoscale model can be extended to all the laminate families with their highly varying anisotropy ratio and if so, how does the relationship between the cracking density and the damage indicator vary. For this study, conductivity values of laminates found in the literature are used to solve the homogenization problem. The conductivities can be found in Table 2.3. The relationship between d and ρ is plotted in Fig. 3.18. For simplicity, τ is taken to be 0. It can be seen that the relationship between the damage indicator and ρ significantly varies with the conductivity of the ply. On careful observation, it can be seen that the damage curve depends on the value of the through-thickness anisotropy ratio, λ_t. This is illustrated in Fig. 3.19 where the dependence of the damage value for $\rho = 0.5$ on λ and λ_t is shown. Higher λ_t leads to larger damage at a given cracking density. This is because when λ_t is smaller, the applied energy can diffuse more along the through-thickness direction, thereby reducing the intensity of damage. The intrinsic nature of the mesoscale relationship obtained for the different conductivities is investigated as well.

Influence of ply thickness: For inner plies, the thickness of the bottom (H') and the top plies (H'') were varied as $H'/H = H''/H = [0.5, 1, 2, 4, 8]$ and the behavior of the damage variable is determined. Fig. 33.18 shows that the damage indicator is independent of the thickness of the surrounding plies.

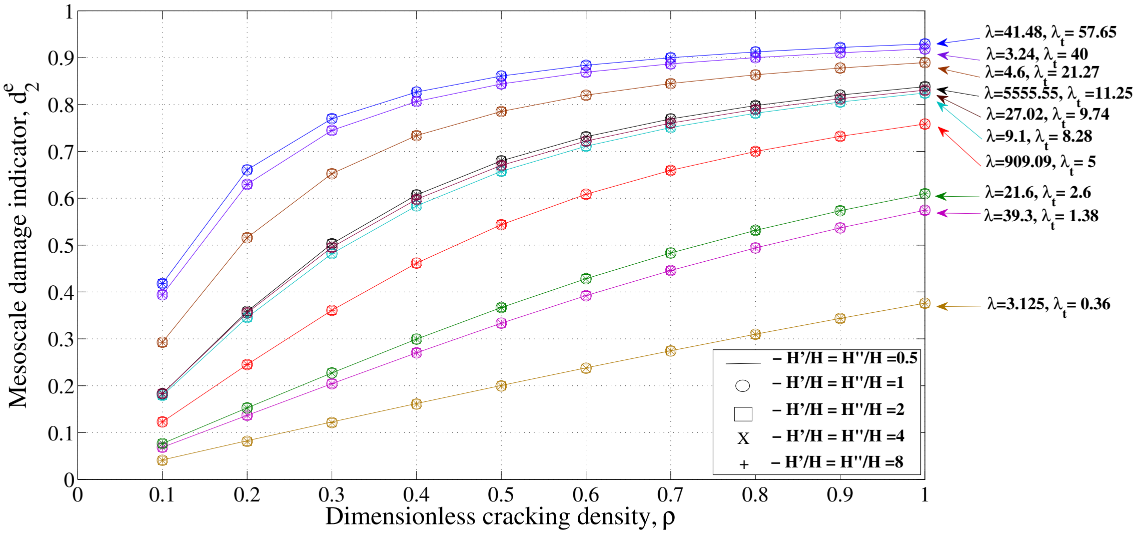

Figure 3.18: Influence of thickness of the outer plies on the damage indicator of degraded inner ply

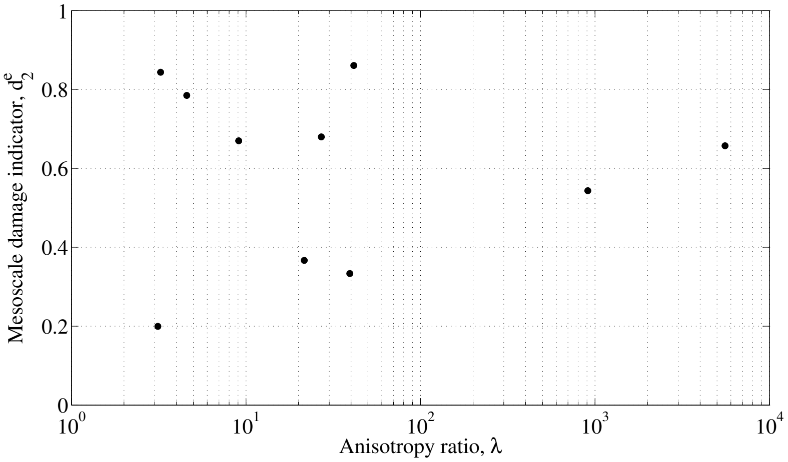

(a) Dependence of d_2^e for a given ρ on λ

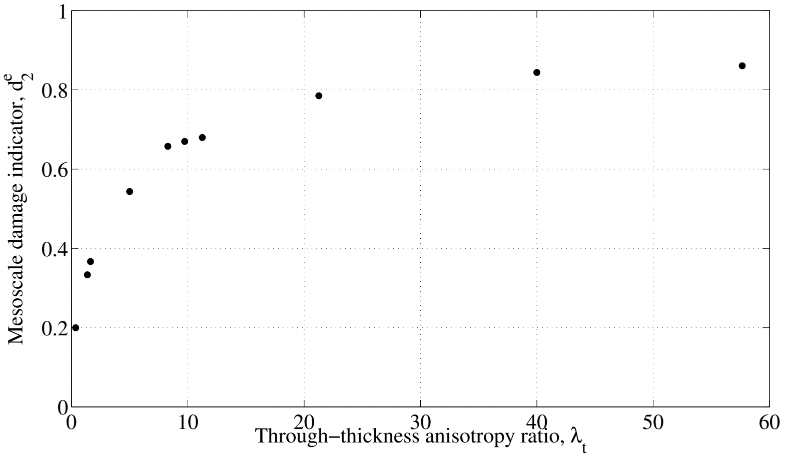

(b) Dependence of d_2^e for a given ρ on λ_t

Figure 3.19: Dependence of d_2^e for a given ρ on anisotropy

Influence of orientation: Similarly the influence of the orientation of the surrounding plies is studied by varying the orientation of the two outer plies (θ', θ'') as $\theta' \in [0^0, 30^0, 45^0, 60^0, 90^0]$ and $\theta'' \in [0^0, 30^0, 45^0, 60^0, 90^0]$. From Fig. 3.20, we can observe that the damage indicator is independent of the orientation of surrounding plies as well.

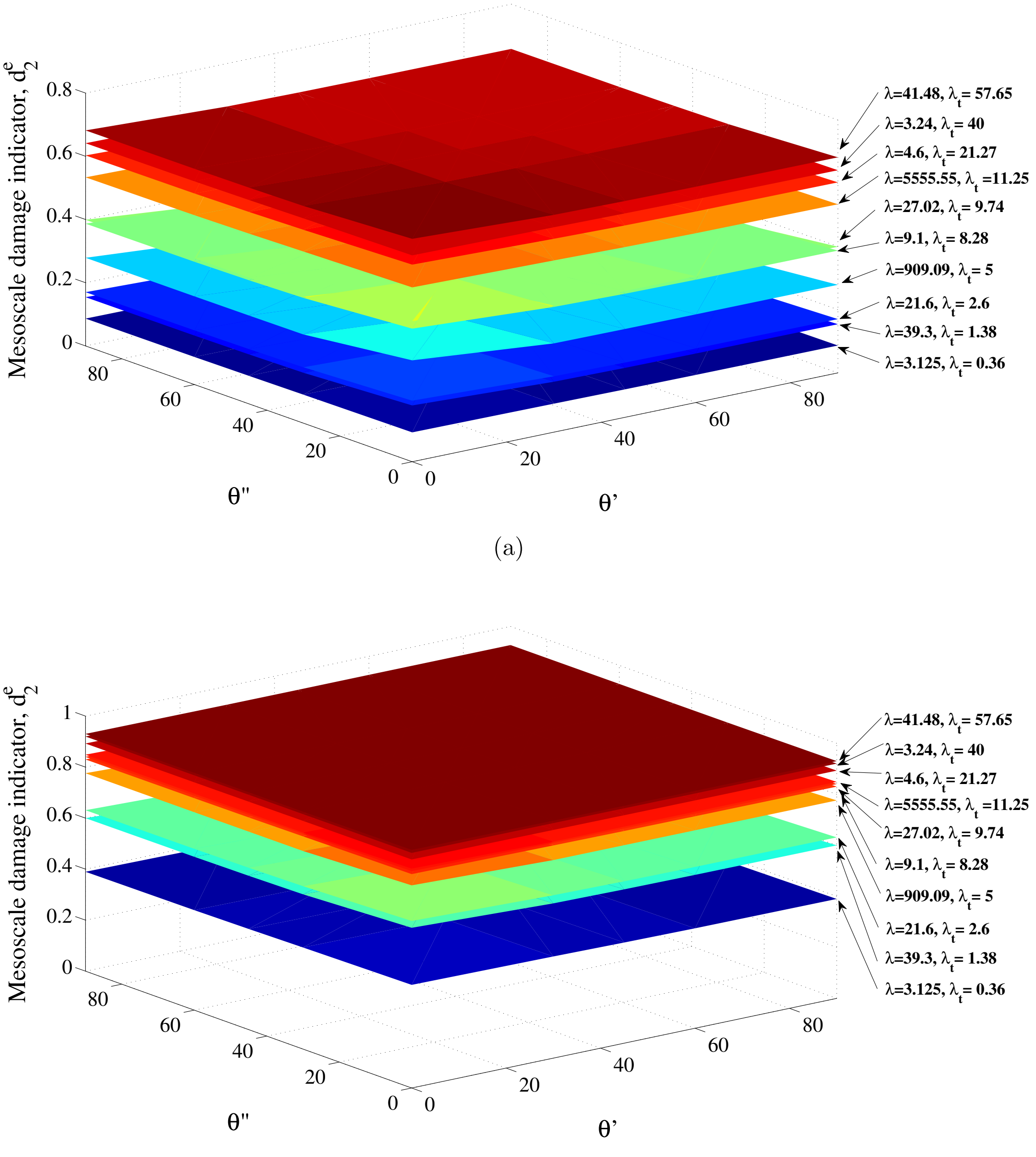

(a)

(b)

Figure 3.20: Influence of orientation of the outer plies on the damage indicator of degraded inner ply for various ply conductivity

3.8 Effect of resin rich interlayer between plies

In toughened composite laminates, there is a presence of a thin matrix layer between the plies as shown in Fig. 3.21. This insulating matrix layer, which is around 10-30μm thick, inhibits current flow in the through-thickness direction and can affect the developed relationship between the mesoscale damage indicator and the microscale cracking densities. To understand the effect of this layer, a thin representative layer is introduced between the plies in the residual problem and the mesoscale homogenization is carried out for various thickness of the resin layer. The residual problem solved for is shown in Fig. 3.22.

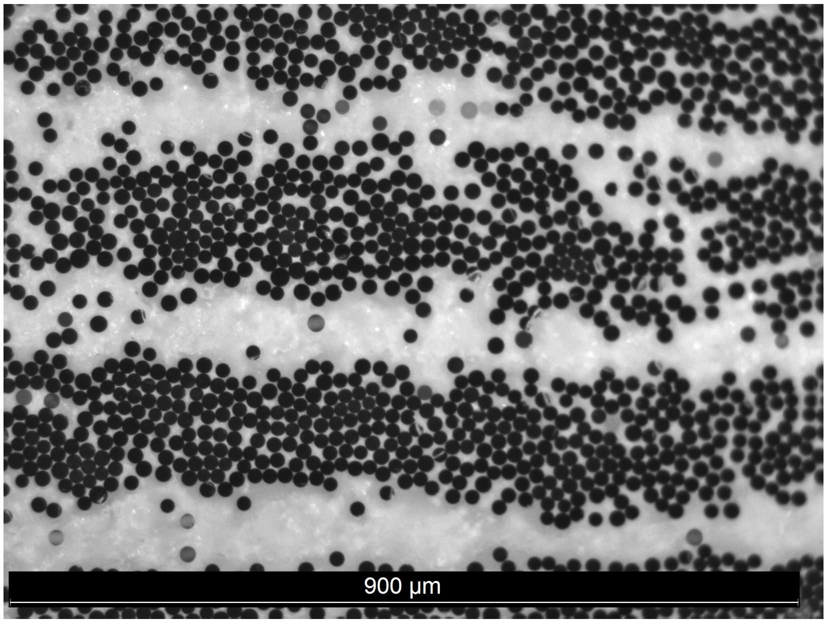

Figure 3.21: Toughened composite laminate with resin rich interlayer

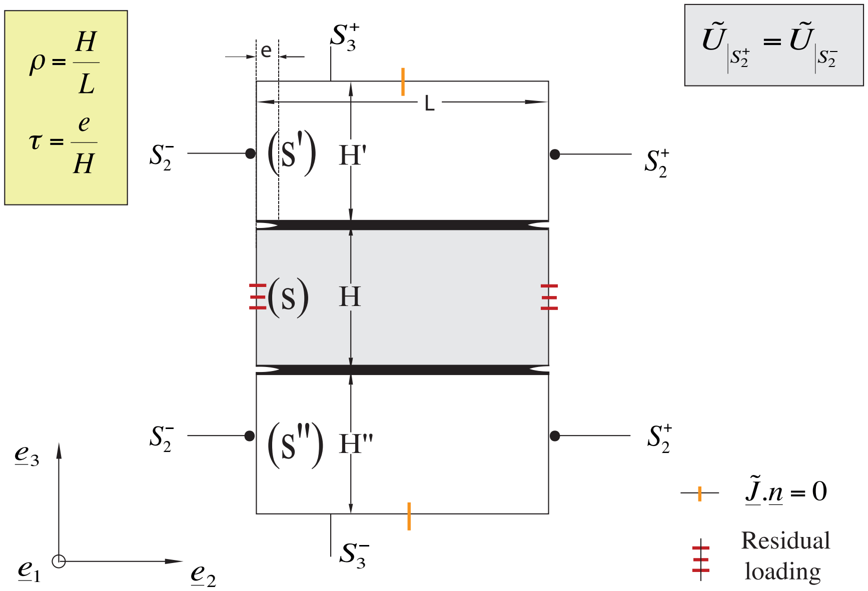

Figure 3.22: Residual problem for the toughened composite laminate

The results for d_2^e is shown in Fig. 3.23 (a) along with the damage indicator for laminates with no resin rich interlayer. It can be seen that the presence of the matrix layer between the plies increases the magnitude of damage indicator for the same cracking density. However, changing the thickness of the interlayer (from 10 to 100 microns) does not shift the damage curve further.

Fig. 3.23 (b) shows the damage curve when local delamination is introduced. We observe that damage curve is independent of the increasing local delamination length. This is due to the resin layer which inhibits the sensitivity towards local delamination. It is also to be noted that due to the presence of the resin layer, the applied electric current cannot penetrate through the thickness of the laminate. Hence, identification of transverse cracks in composite laminates with rich resin interlayer is only possible through intrusive electrodes that run through the thickness of the laminate.

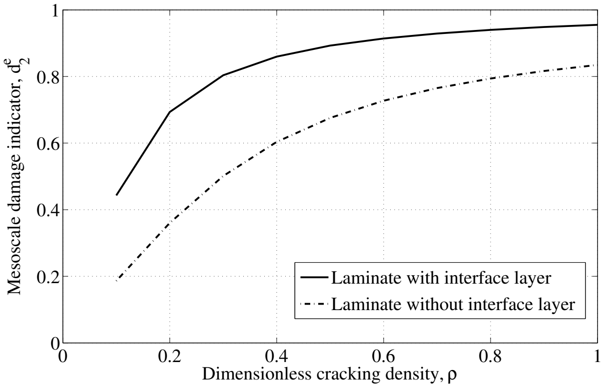

(a) Variation of damage indicator with and without a resin rich interlayer

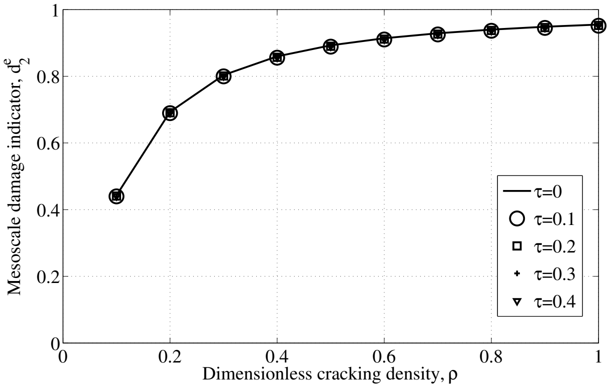

(b) Variation of damage indicator for varying transverse cracks and local delamination with a resin rich interlayer

Figure 3.23: Effect of resin rich interlayer between plies

3.9 Effect of crack closure

In the development of the mesoscale model, we consider that the transverse cracks and local delamination are fully open, i.e., the resistivity is extremely large. However, in real case scenarios, cracks can be partially open, i.e., there is partial electrical contact between the two crack surfaces. This is especially observed when the structure is unloaded. In such cases, the value of the damage indicator will vary depending on the level of contact between the two cracked surfaces. To understand the effect of crack closure, a new residual problem is proposed where contact impedance is introduced at the cracks and mesoscale homogenization is performed. By varying the contact impedance, the effect of the different levels of crack closure can be modeled. It is assumed that the contact impedance is uniform over the entire crack surface and between the other cracks. The residual problem to be solved is shown in Fig. 3.24. The material properties are taken to the same as the initial simulations (the same procedure can be extended to any conductivity).

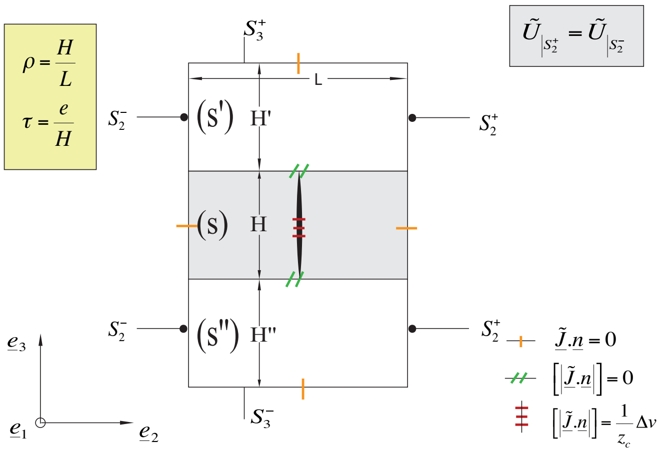

Figure 3.24: Influence of the partial contact between cracks on the damage indicator

Fig. 3.25 shows the variation of the damage indicator as a function of varying contact impedance between the cracks corresponding varying level of crack closure. It can be seen that the intensity of damage decreases with decreasing contact impedance. The magnitude of the contact impedance that corresponds to completely open and closed cracks can also be identified from Fig. 3.25 (a).

Fig. 3.26 shows the variation of the damage indicator when both transverse cracks and local delamination are present. Local delamination is taken as $\tau = 0.1$. Fig. 3.26 (a) and (b) show the influence of the local delamination closure on d_2^e. Fig. 3.26 (a) shows the evolution when the contact impedance between the local delamination is 1 Ωm^2 and Fig. 3.26 (b) shows the evolution when the contact impedance is $1e^{-8}\Omega\text{m}^2$. We observe that the local delamination closure shifts the damage curve to the damage

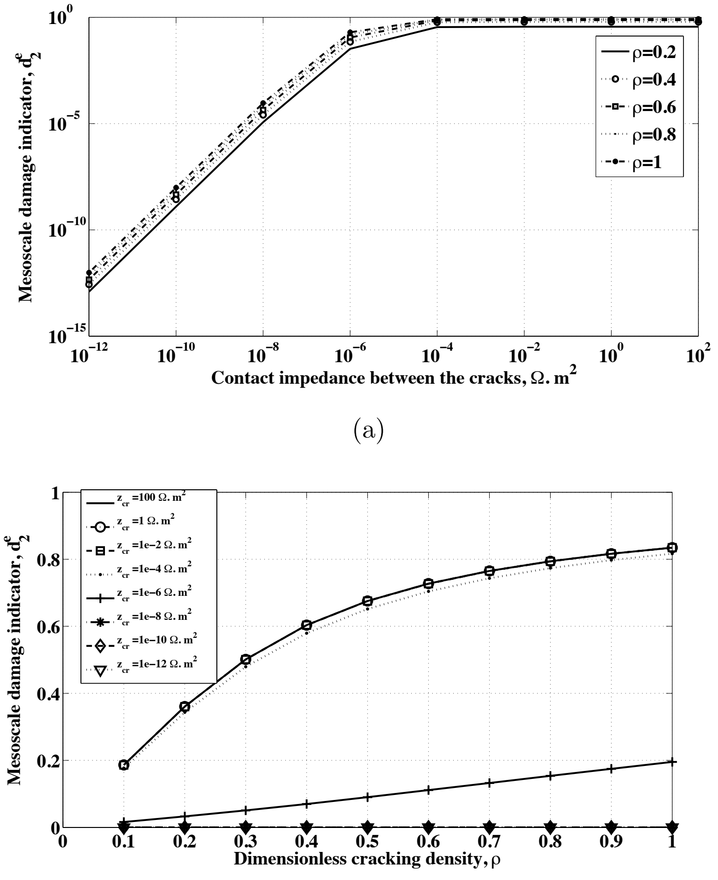

(a)

(b)

Figure 3.25: Variation of damage indicator for different levels of crack closure

corresponding to $\tau = 0$. Although not shown here, similar behavior is observed for other values of τ.

3.10 Validation of the homogenized model on a complex damage scenario

We present a scenario with complex damage profile to validate the mesoscale model developed, by comparing the electrical energy at the microscale in the presence of the degradation and the equivalent mesomodel. The conductivity of the undamaged ply

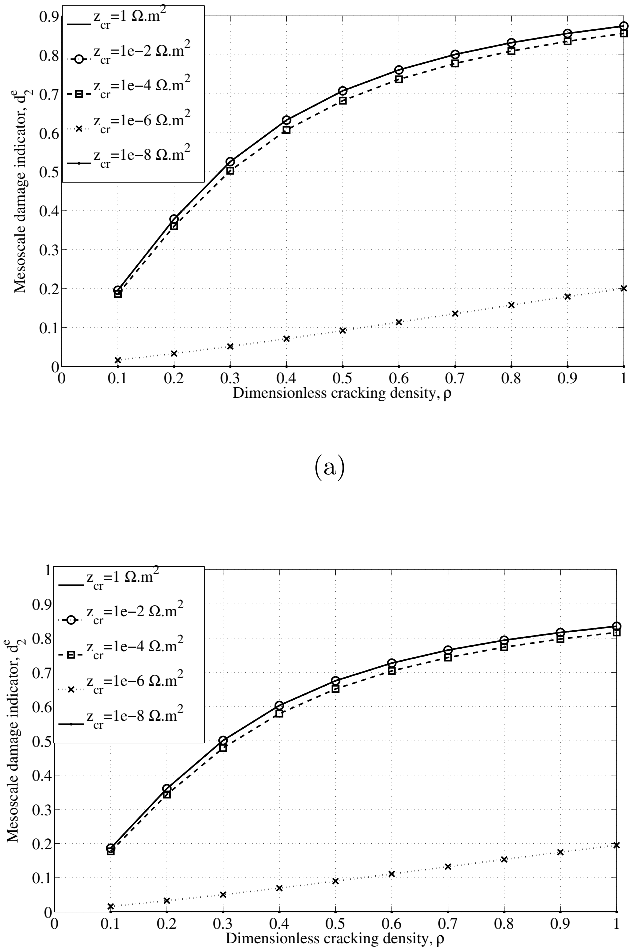

(a)

(b)

Figure 3.26: Variation of damage indicator for different levels of transverse cracks and local delamination closure

is taken as

$$\underline{\underline{\Sigma}}_0 = \begin{bmatrix} 5500 & 0 & 0 \\ 0 & 203.5 & 0 \\ 0 & 0 & 20.4 \end{bmatrix} S/m$$

The configuration considered consists of a quasi-isotropic laminate ($[0/-45/45/90]_s$) with a different degradation state in each ply as shown in Fig. 3.27 below. The choice of this degradation pattern within the laminate is arbitrary to showcase the capability of the model to represent any complex scenario, and does not reflect any experimental results. This example is given here as a case study. Similar results were obtained with multiple case studies that are not presented here. The loading consists of both the in-plane and the out-of-plane components. The in-plane loading consists of potential difference $V_{NN'}$ across the periodic domain. The out-of-plane loading consists of a uniform current applied across the through-thickness direction.

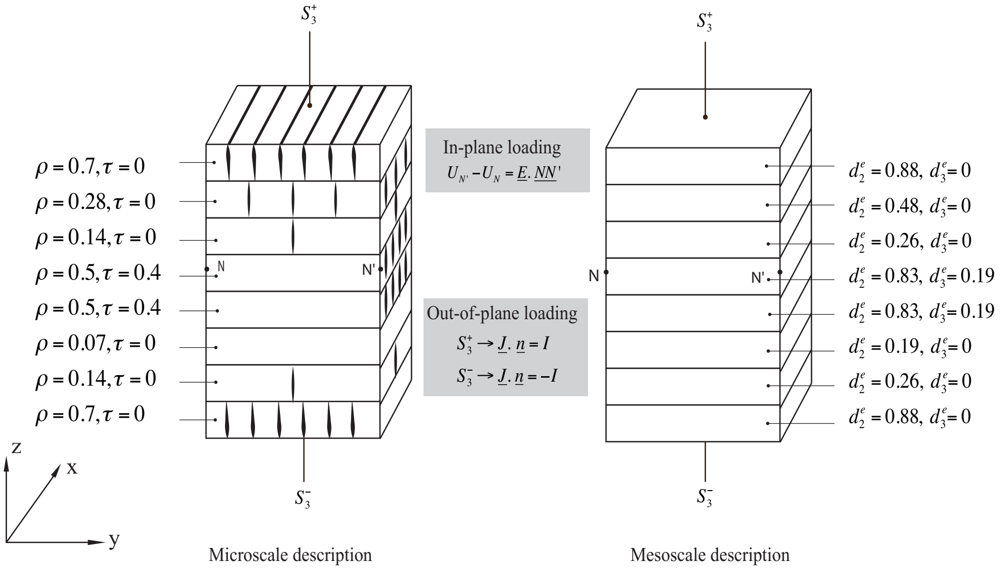

Figure 3.27: Damage scheme considered for validation

For the microscale problem (in which crack and delaminations are explicitly introduced as discontinuities) the problem is then to find $(U, \underline{E}, \underline{J})$ such that:

- *Kinematic admissibility conditions:*

$$\underline{E} = -\underline{\nabla} U, \qquad \forall \underline{M} \in \Omega \qquad \text{(Compatibility condition)}$$

$$U_N - U_{N'} = \bar{\underline{E}}.\underline{NN'} \qquad \forall (N, N') \in \text{ x, y boundaries} \qquad \text{(Periodicity conditions)}$$

- *Static admissibility conditions:*

$$div \underline{J} = 0 \qquad \forall \underline{M} \in \Omega \qquad \text{(Interior equilibrium equation)}$$

$$\underline{J}.\underline{n} = I, \qquad \forall \underline{M} \in S_3^+ \qquad \text{(Loading)}$$

$\underline{J}.\underline{n} = -I, \quad \forall \underline{M} \in S_3^-$ (Loading)

$[|\underline{J}.\underline{n}|] = 0, \quad \forall \underline{M} \in$ interfaces (Continuity across the interfaces)

$\underline{J}.\underline{n} = 0, \quad \forall \underline{M} \in$ crack surface (Flux free condition over cracks and delamination)

- *Constitutive equation:*

  $\underline{J} = \underline{\underline{\Sigma}}_0(\underline{M}) \otimes \underline{E}, \quad \forall \underline{M} \in \Omega$

For the mesoscale problem, the explicit description of cracks is removed, and we modify the constitutive tensor in each ply as a result of the homogenization defined earlier:

$$\underline{J} = \underline{\underline{\Sigma}}(\underline{M}).\underline{E}, \quad \forall \underline{M} \in \Omega \tag{3.30}$$

where

$$\underline{\underline{\Sigma}}(\underline{M}) = \Sigma_{11}^0 \underline{e}_1 \otimes \underline{e}_1 + (1 - d_2^e)\Sigma_{22}^0 \underline{e}_2 \otimes \underline{e}_2 + (1 - d_3^e)\Sigma_{33}^0 \underline{e}_3 \otimes \underline{e}_3 \tag{3.31}$$

with d_2^e and d_3^e describing the ply level damage in the transverse and the through-thickness directions.

Experiments found in the literature use a constant current between 10mA-300mA at the electrodes. For the current study, we chose a constant current of 10mA across the $\underline{e}_3$ direction along with a potential difference of 3.3mV in the in-plane direction. To understand the effects of the in-plane loading direction, we perform a systematic study by rotating the in-plane field between 0° and 360°. The choice of the loading was made to reflect a physically reasonable electrical loading state and is otherwise arbitrary. For the configuration described above, Fig. 3.28 (b) shows the electrical energy of the 1) microscale model without any cracks 2) microscale model with cracks and 3) equivalent mesoscale energy for two sample loading directions (along $0°, 45°$

with respect to the x-axis). It can be seen that the differences between the electrical energies in the micro and the mesoscale model is negligible. This difference is due to the coupling effects between the degradations in the different plies that are not accounted for in the present model.

Fig. 3.28(a) describes the relative variation in the energies (microscale and mesoscale) when the cracks are introduced. This shows the change one can expect when cracks start to develop in the system, which for this specific case is found to be in the range of 1.9-2.6 for microscale and 1.7-2.4 for mesoscale. The error between the two models is of the order of 0.2% which shows that the mesomodel is sufficiently accurate. The relative variation at the microscale (mesoscale variation is given by a similar definition) is given by

$$\text{Relative variation}(\%) = \frac{E_{uncracked} - E_{micro}}{2(E_{uncracked} + E_{micro})} \times 100\% \tag{3.32}$$

where E_{micro} is given by the electrical energy at the microscale when the cracks are introduced and $E_{uncracked}$ denotes the electrical energy of the uncracked model. Fig. 3.28 (c) shows the percentage ratio of the error between the microscale and the mesoscale model (modeling error) to the change in the energy at the microscale when cracks are introduced, which is found to be quite small (below 12%). This ensures that the mesomodel is valid and can be used to capture the effects of cracking in the laminate. The voltage profiles across the three planes of symmetry for the loading applied in the x-direction are shown in Fig. 3.29.

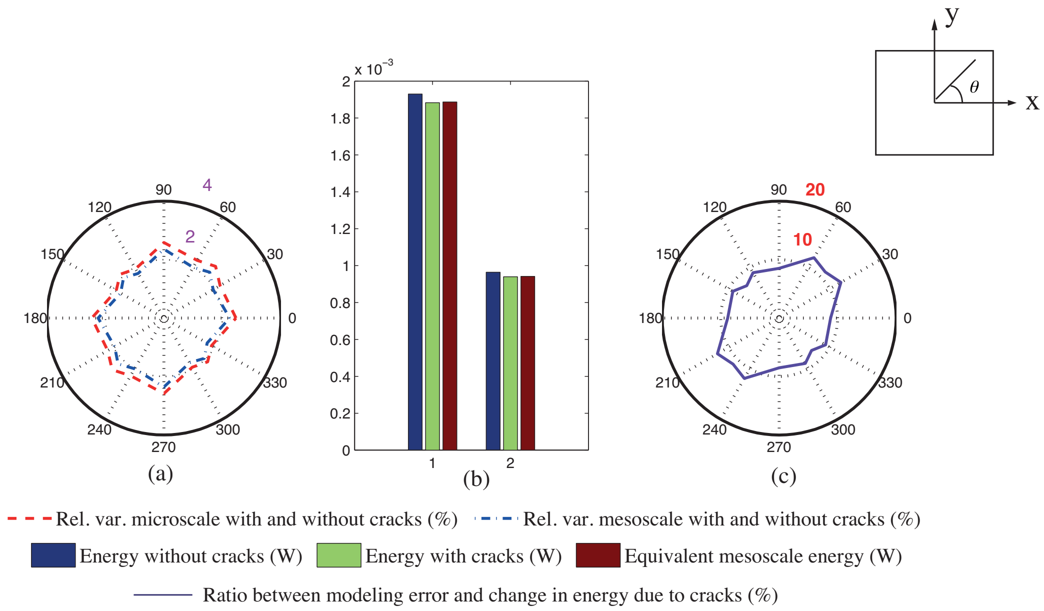

(a) (b) (c)

Figure 3.28: (a) Relative variation of energy in the micro and the mesoscale when cracks are introduced, (b) Comparison of electrical energy between the microscale and the mesoscale description for two sample orientations and (c)Percentage ratio of the modeling error to the change in energy when cracks are introduced

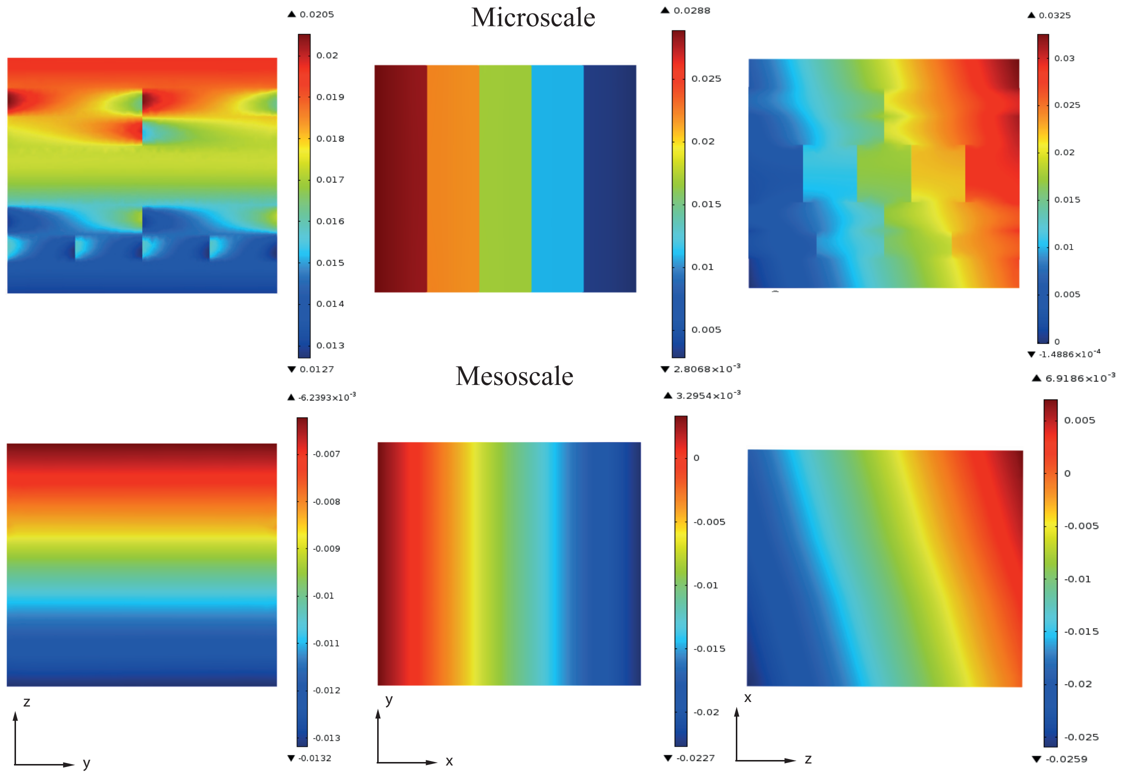

Figure 3.29: Comparison of voltage profiles between the microscale and mesoscale solutions

3.11 Discussion

The framework of mesoscale homogenization for composite laminates has been presented. The relationship between microscale damage and the damage indicators have been presented for various configurations. The energy equivalence has been validated through an example. The main results are as follows:

1. Mechanisms at the microscale can be successfully homogenized at the mesoscale. The discrete damage mechanisms at the microscale can be equivalently represented as a modification of the conductivity of the ply at the mesoscale. The

conductivity tensor of the ply that has been damaged has the form

$$\underline{\underline{\Sigma}} = \begin{bmatrix} \Sigma_{11}^0(1-d_f) & 0 & 0 \\ 0 & \Sigma_{22}^0(1-\tilde{d})(1-d_2^e) & 0 \\ 0 & 0 & \Sigma_{33}^0(1-\tilde{d})(1-d_3^e) \end{bmatrix}_{(\underline{e}_1,\underline{e}_2,\underline{e}_3)} \tag{3.33}$$

where d_f denotes damage due to fiber fracture, $\tilde{d}$ denotes diffuse damage and d_2^e, d_3^e denotes the damage due to transverse cracks and local delaminations.

2. The mesoscale damage indicators are intrinsic to each ply. The model is independent of the geometrical parameters of the surrounding plies. Thus it can be applied to any stacking sequence or geometry. This is highly important as this shows that the damage variables are only influenced by the level of degradation within the ply and nothing else.

3. The damage indicators are constant through the thickness of the ply and varies only in the in-plane direction.

Chapter 4

Detectability of transverse cracks

Abstract

In the earlier chapter, the concept of mesoscale homogenization was outlined and the relationship between the microscale damage and damage indicators were presented. However, when it comes to identifying transverse cracks or local delamination by solving the inverse problem, the quality and the sensitivity of the measurements obtained is crucial. The quality of the measurements primarily depends on the experimental set-up. However, the sensitivity of the measurements towards the damage mechanism of interest depends on the material and geometrical properties of the laminate. We focus here on the detection of the transverse cracking mechanism. We demonstrate here from numerical experiments that the sensitivity depends on several parameters, such as the anisotropy in the electrical conductivity of the baseline composite ply or the geometrical parameters of the structure. Based on these results, applicability of electrical tomography to detect transverse cracks in a laminate is discussed. One conclusion from the study is that detecting transverse cracks using electrical tomography is more reliable in some laminate configurations than others. Some recommendations about properties of either the pristine material or the inspected structures are pro-

vided to establish whether one can rely on electrical tomography to detect transverse cracks.

4.1 Introduction

Since conductivity of composites is anisotropic, the sensitivity of the measurements with respect to the various damage mechanisms are different and direction-dependent. It was shown in [77] that indeed for a typical Carbon Fiber Reinforced Plastic (CFRP), the change in the electrical potential measured at the electrodes due to transverse cracks was very small, i.e. the sensitivity was minimal. Also, unlike experiments which are carried out in a controlled environment, the nature of the loading in actual applications is often unknown and the degradation profile is complex due to multiple mechanisms occurring simultaneously. Thus, the effect of transverse cracks is hard to isolate from the other conductivity changing mechanisms such as piezoresistivity, plasticity, delamination, etc. if the sensitivity is too small. Yet, the various factors that influence the sensitivity of the measurements to transverse cracks are poorly understood. An understanding of the following aspects is thus required: (i) whether the damage is detectable through the voltage measurements, i.e. whether the change in the conductivity is higher than the level of noise, (ii) how sensitivity varies for different material and geometrical parameters, such as conductivity ratio, thickness ratio, and current injection patterns, and (iii) how the sensitivity towards transverse cracks compares with other conductivity changing mechanisms. Since the anisotropy in electrical conductivity of the single ply largely varies depending on the nature of the primary constituents, this study will show the range of applicability of electrical tomography for detecting transverse cracks.

In this following section, we present the effect of the various parameters outlined before on the sensitivity of the measurements to transverse cracks. Following that, a simple analytical model that can predict the expected sensitivity for a given laminate. Finally, a general discussion is provided on the capability of ET to monitor transverse cracking in laminates.

Through mesoscale homogenization, we have established that transverse cracks modify the transverse electrical conductivity $\Sigma_{22} = \Sigma_{22}^{\circ}(1 - d_2^e)$ of the ply with a level of change directly related to the level of cracking, ρ. This damage indicator was shown to be intrinsic, meaning that the evolution of d_2^e depends only on the cracked state of the ply and not on the geometric and material parameters of the surrounding plies. This makes the model generic, in the sense that it can be applied to any laminate structure. So, theoretically, in order to identify the level of transverse cracks in a ply through electrical tomography it is sufficient to identify the transverse conductivity at the mesoscale and then interpret the cracking density ρ locally from the obtained transverse conductivity.

However, it should be noted that, if the change in conductivity due to damage is very small, i.e. the relative change in the measurements is too small, then the reliability of the method to identify damage is reduced. Transverse cracks are detectable if the change in the electrical energy due to the introduction of these cracks is above (i) the resolution of the measuring instruments and (ii) the level of noise in the measurements. Hence, higher current through the cracked ply, directly implies more sensitivity towards damage, and the amount of current flowing through a ply in a given direction depends mainly on the following parameters: (i) conductivity ratio, (ii) thickness ratio, (iii) current injection patterns. We will focus on how these parameters affect the sensitivity towards transverse cracking, that we shall define as the relative change in voltage produced for 10% change in transverse conductivity.

4.2 Effects of geometric and material properties on sensitivity

4.2.1 Parameters and computational setup

Two common laminate lay-ups are considered: cross-ply ($[0^\circ_{mn}/90^\circ_n/0^\circ_{mn}]$) and quasi-isotropic ($[45^\circ_{mn}/-45^\circ_{mn}/90^\circ_n/0^\circ_{mn}]_s$) as shown in Fig. 4.1 (a). Parameter m, called the thickness ratio, is the ratio of thickness of the individual surrounding plies to the thickness of the cracked ply. Parameter n is the number of layers in the cracked ply. The length of the sample is 100 mm and thickness of a single layer is 0.25 mm. Eight electrodes are placed on the surface of the laminate (four on the top and four on the bottom). The outer electrodes are 80 mm apart and are used for current injection. The inner electrodes are 60 mm apart and are used for voltage measurements. The values of contact impedance and conductivity is taken as $z_{el} = 1 \times 10^{-4}\,\Omega\text{m}$, $\Sigma^\circ_{22} = \Sigma^\circ_{33} = 1$ S/m and $\Sigma^\circ_{11} = \lambda\Sigma^\circ_{22}$ respectively. For the simulations carried out in this work, current of $I_{el} = 0.25$ is injected in three ways: 1) one pair (top) 2) two pairs and 3) oblique injection as shown in Fig. 4.1 (b).

Damage is considered to occur in the 90° plies homogeneously. Thus, $\Sigma_{22}(90^\circ) = \Sigma^\circ_{22}(90^\circ)(1 - d^e_2)$. In the following studies, the fibers of the damaged 90° ply is taken to be oriented along the y-axis. For each configuration, we solve for the electrostatic problem described in Section 2.3.1. For solving, finite element commercial code COMSOL Multiphysics was used. The geometry was discretized using linear elements of size 0.1 mm×0.1 mm×1 mm. Once the problem is solved, the average surface voltage at each electrode is obtained. As mentioned above, we compute the sensitivity as the relative voltage change:

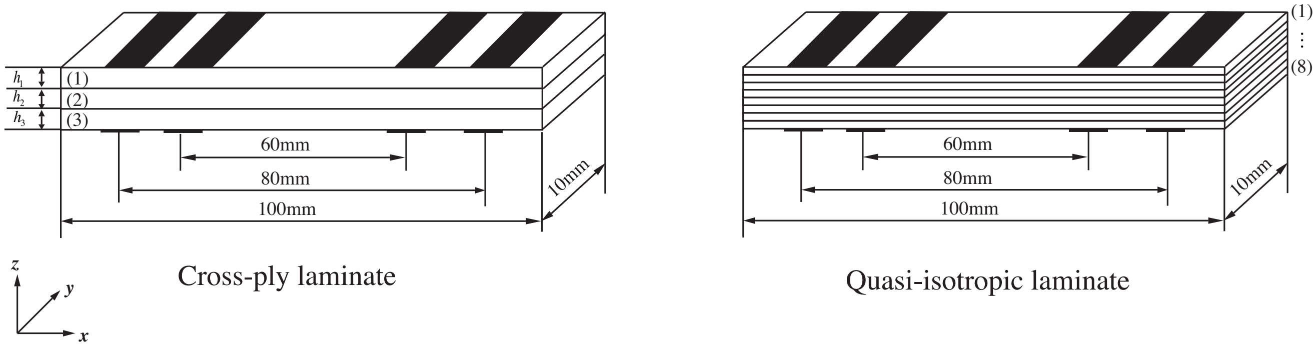

(a) Geometry

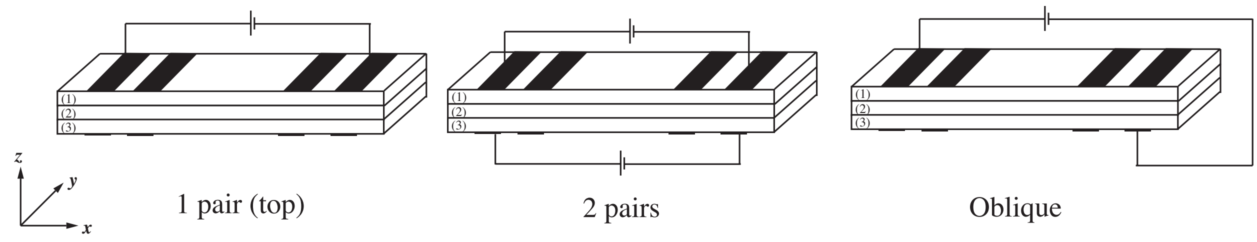

(b) Current injection patterns

Figure 4.1: Geometry and current injection patterns

$$S = \frac{V - V^{\circ}}{V^{\circ}} \times 100\% \qquad (4.1)$$

where V° and V are the average electric potential at all the four measurement electrodes evaluated for $d_2^e = 0$ (no damage) and 0.1 (10% change in conductivity), respectively. It should be noted that in the following figures, the data points represent the calculated average and the error bar denotes the variation in the voltage measurements obtained from all four measurement electrodes.

4.2.2 Effect of orthotropic conductivity

To understand the effect of the conductivity ratio, λ, we compute the sensitivity S for $\lambda = [1000, 100, 10, 2, 0.5]$ for both laminates. The results are shown in Fig. 4.2. The values of λ are sampled from the range observed in the literature for composites. The thickness of each ply is kept constant for the study. It can be seen that the measurements show higher sensitivity towards damage in the cross-ply than quasi-isotropic laminates. Also, the sensitivity decreases with increasing λ. The results obtained from the study agree well with the results from [77]. In [77], the conductivity ratio of the specimens considered in the experiments was around 27 and the variation due to matrix cracking was around 0.2-0.4% at saturation.

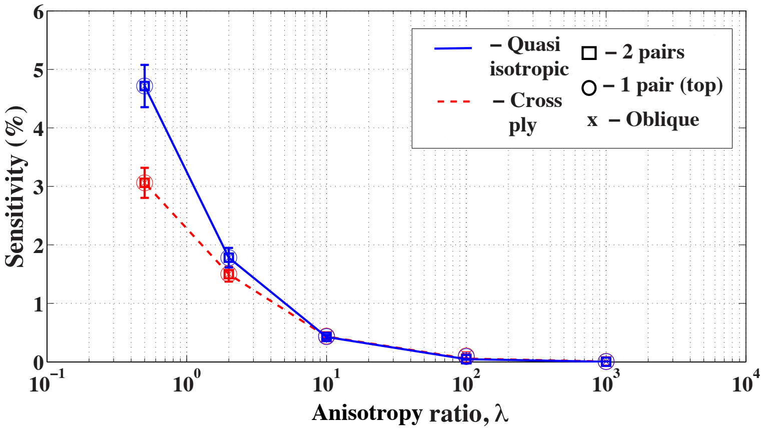

Figure 4.2: Relationship between sensitivity and λ for 10% change in $\Sigma_{22}(90^\circ)$

4.2.3 Effect of thickness ratio

We study the effect of thickness ratio, m, on sensitivity, S. By varying the thickness ratio, we vary the amount of current passing through the different layers which should influence the sensitivity of the measurements towards the damage in the cracked layer. We take $m = [0.5, 1, 2]$ and plot the sensitivity, S versus λ for cross-ply laminate and for quasi-isotropic laminate, as shown in Fig. 4.3 (a) and Fig. 4.4 (a), respectively. It can be seen that for a given λ, decreasing thickness ratios improves the sensitivity. This can be explained by the fact that the amount of current flowing through the cracked ply increases when the thickness of the surrounding plies is reduced, thereby increasing the sensitivity. It can also be seen that the sensitivity is intrinsic with respect to $m\lambda$ for the cross-ply laminate and $2m\lambda+m$ for the quasi-isotropic laminate, as shown in Fig. 4.3 (b) and Fig. 4.4 (b), respectively. The quantities $m\lambda$ and $m(2\lambda+1)$ represent the ratios of the equivalent conductivity of the plies surrounding the cracked plies to the conductivity of the cracked plies (in the direction of the applied current). They will be referred to as nominal λ. Thus decreasing the thickness ratio, m, decreases the equivalent λ for the same laminate configuration.

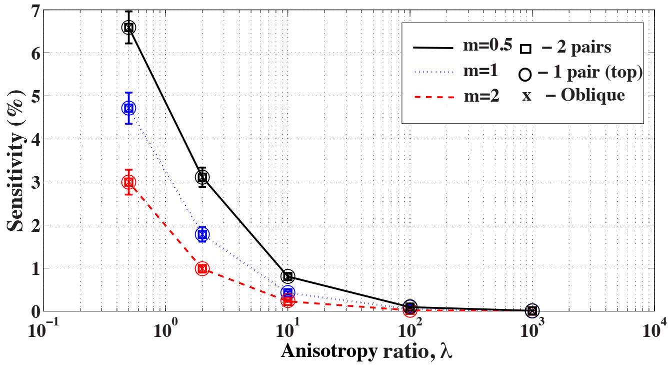

(a) Relationship between m and sensitivity

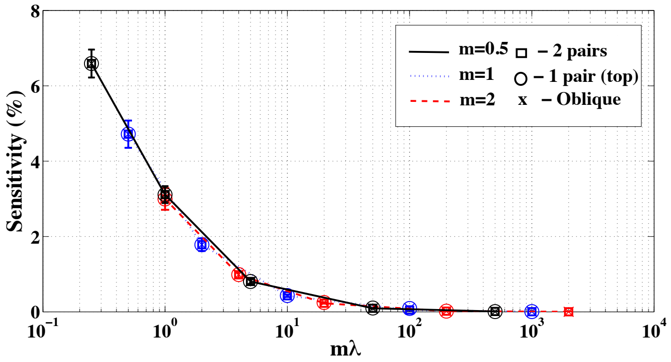

(b) Intrinsic behavior of sensitivity with $m\lambda$

Figure 4.3: Effect of thickness ratio on sensitivity for cross-ply laminate

4.2.4 Effect of current injection pattern

The cross-ply laminate configuration is taken as $[0^\circ_n/90^\circ_n/0^\circ_n]$ (m=1). First, we define parameter, χ as:

$$\chi = \frac{J_x^3 A_3}{J_x^1 A_1}. \tag{4.2}$$

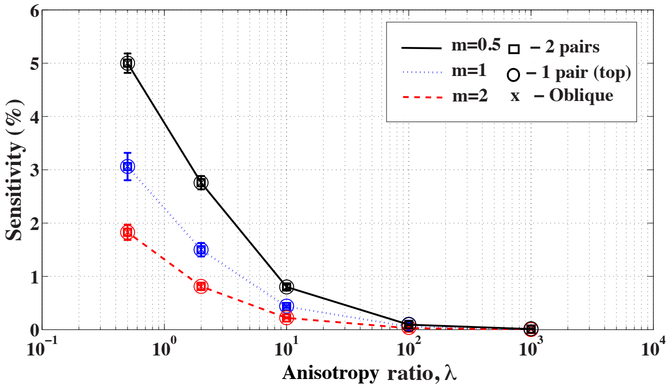

(a) Relationship between m and sensitivity

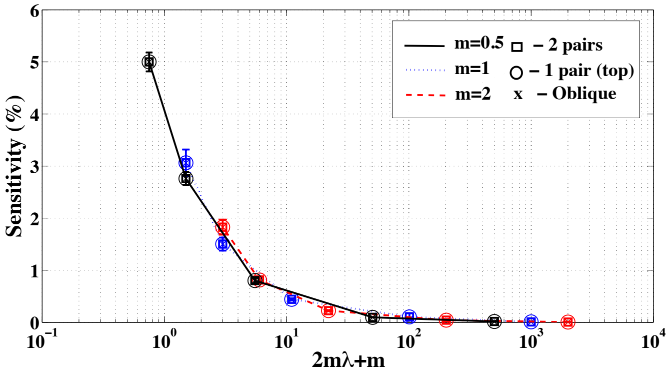

(b) Intrinsic behavior of sensitivity with $2m\lambda + m$

Figure 4.4: Effect of thickness ratio on sensitivity for quasi-isotropic laminate

Here $J_x^p A_p$ is the total current flowing through the ply p, J_x^p denotes the current density in the x-direction, and A_p is the cross-sectional area of ply p perpendicular to the current flow. Hence, the parameter χ shows how the applied electrical current distributes through the thickness of the laminate for the different injection patterns. We also define ψ as

$$\psi = \frac{1}{\lambda}\frac{J_x^1 A_1}{J_x^2 A_2}, \tag{4.3}$$

which shows how the total current applied divides among the 0° ply and 90° ply. We plot both parameters for $n = [4, 8, 16]$ and λ, in Fig. 4.5 (a) and (b), respectively.

These two parameters quantify the amount of current passing through the different plies of the cross-ply laminate and can be used to understand how the total thickness of the laminate and the different injection patterns influence the current distribution. The results from this study are:

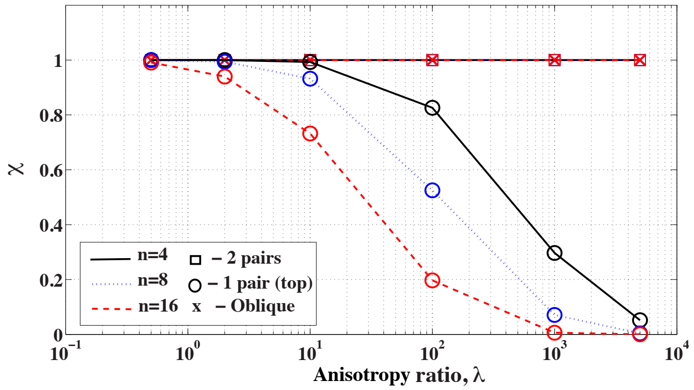

(a) Relationship between χ and λ for different n

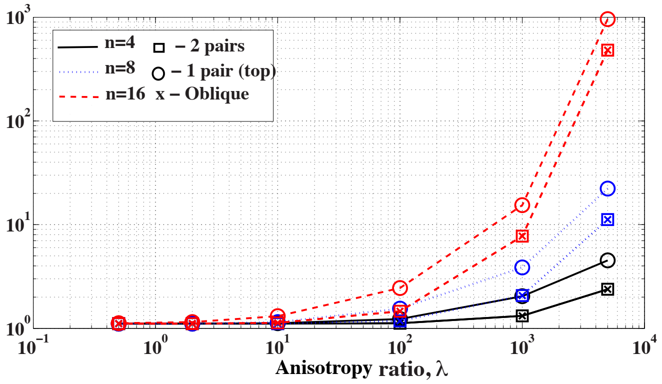

(b) Relationship between ψ and λ for different n

Figure 4.5: Current ratio between different plies

1. From Fig. 4.5 (a), it is observed that $\chi = 1$ for 2 pairs/oblique injection patterns whereas $\chi < 1$ for 1 pair injection. In the case of 1 pair injection, most of the current passes through the top ply and the amount of current reaching the bottom plies decreases as λ and n increases. Extending it to a general scenario, it can be seen that using 1 pair injection is disadvantageous when the cracked ply is closer to the bottom of the laminate. Hence, it is better to use 2 pairs/oblique

injection pattern where the current is distributed equally from the top and the bottom.

2. Fig. 4.5 (b) shows how the current divides among the top 0° ply and the mid 90° ply for increasing λ and n. The use of λ in the definition for ψ is to check if the electric field is in-plane. If $\psi = 1$, then the electric field is in-plane. It can be seen that for increasing λ and n (i) the amount of current passing through the mid 90° ply decreases and (ii) the electric field deviates from being in-plane. When comparing in terms of the current injection patterns, we observe that 2 pairs/oblique injection results in higher current distribution through the 90° ply than the 1 pair injection.

3. Also, Fig. 4.6 compares the potential distribution within the laminate for the different injection patterns. We can see that at lower levels of anisotropy, e.g., $\lambda = 10$, the electric field is in-plane for all the patterns, whereas at higher anisotropy, e.g., $\lambda = 1000$, 2 pairs injection results in a more in-plane field and symmetric field than the other two patterns. It is hence suggested to use 2 pairs for current injection.

4.2.5 Effect of other conductivity changing mechanisms

In composites, damage mechanisms are hardly isolated, i.e. several damage mechanisms occur simultaneously in the laminate. Hence, changes in the voltage measurements obtained at the electrodes reflect not only changes due to transverse cracks but also those due to the other conductivity changing mechanisms. The different conductivity changing mechanisms within the laminate include fiber breakage, piezoresistivity, delamination, diffuse damage, plasticity and temperature [73]. If changes due to

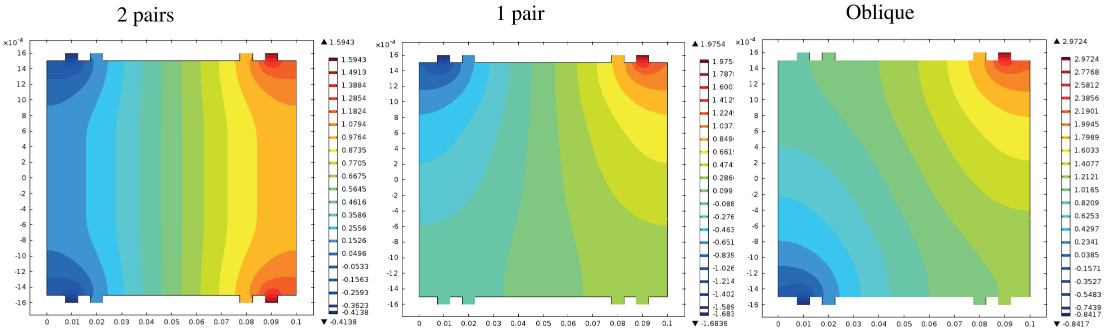

(a) $\lambda = 1000$

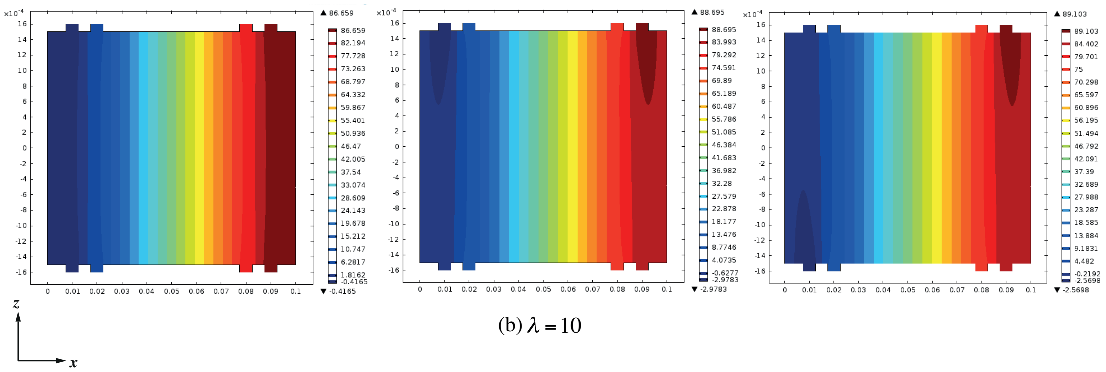

(b) $\lambda = 10$

Figure 4.6: Isocontour of electric potential for different λ

transverse cracks are negligible when compared to changes due to these other mechanisms, then transverse cracks will be hard to detect using EIT. We now investigate how the changes in the voltage measurements due to any of the other conductivity changing mechanisms compare to the change observed with transverse cracks. We consider the following scenario: Σ_{11} of the 0° plies is taken as $\Sigma_{11}(0^\circ) = 0.9\Sigma^\circ_{11}$ and the sensitivity is obtained. This could be attributed to piezoresistivity and/or fiber breakage in the 0° plies [91, 77]. We will compare how the sensitivity varies when transverse cracks are introduced in the same laminate, i.e. when $\Sigma_{22}(90^\circ)$ becomes $\Sigma_{22}(90^\circ) = 0.9\Sigma^\circ_{22}$. The results are shown in Fig. 4.7. It can be seen that when $\lambda \geq 100$, the voltage changes due to transverse cracks are very small when compared to the changes due to fiber breakage and/or piezoresistivity. When $\lambda \geq 100$, the sensitivity towards transverse cracking improves with decreasing λ. Thus, with increasing λ, the presence of other conductivity changing mechanisms makes the detection of transverse cracks difficult.

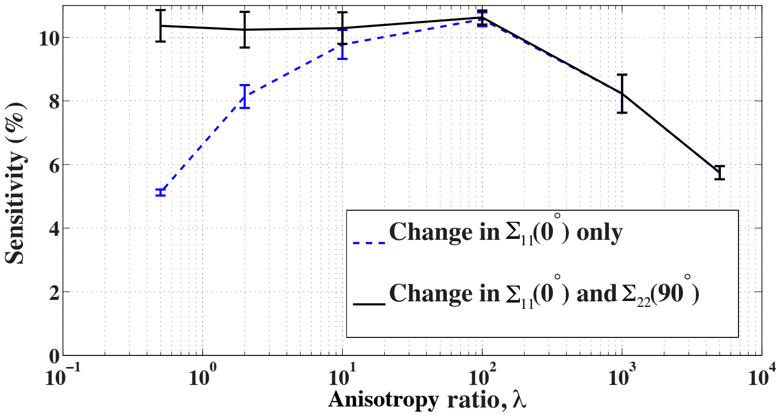

Figure 4.7: Effect of fiber breakage on the measurements

4.3 Analytical model

In this section, we propose an analytical model for the voltage change expected with homogeneous change in conductivity due to cracks/damage. Since it has been observed from the numerical experiments, presented in the previous section, that the electrical field is actually in-plane when $\lambda \leq 100$, we can thus develop a simplified model that can be used to quickly determine the expected sensitivity for varying levels of damage.

Let π represent a cross-section of a composite laminate. Let index $i = 1, 2, ..., p$ refer to the individual plies with orientations $\theta_1, \theta_2, ..., \theta_p$, respectively. We assume that one ply within the laminate exhibits transverse cracks as shown in Fig. 4.8. To detect the presence of these cracks, current is applied through the electrodes on the surface, perpendicular to the cracks. Let the total area of cross-section π be $A = hw$ where h denotes the total thickness and w the width of the laminate. Let A_i and h_i denote the cross-sectional area and thickness of the ply i, respectively.

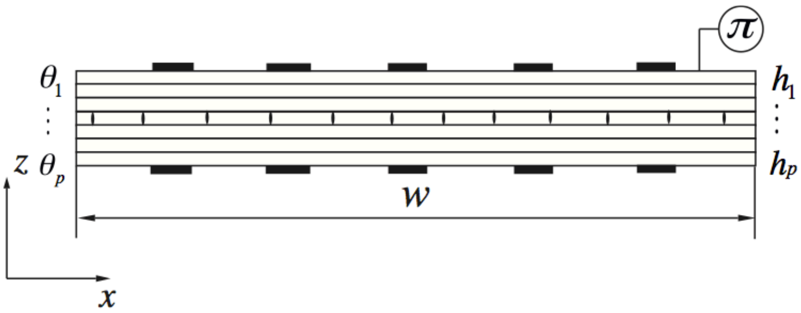

Figure 4.8: Cross-section of the laminate

Then the total current density passing through the cross-section π can be given as

$$\underline{J}^{tot} A = \sum_{i=1}^{p} \underline{J}^{i} A_i \tag{4.4}$$

where the current density $\underline{J}^{i}$ in ply i is given as

$$\underline{J}^{i} = \underline{\underline{\Sigma}}^{i} \underline{E}, \tag{4.5}$$

where $\underline{E}$ is the in-plane electric field. So, Equation (4.4) becomes

$$\underline{J}^{tot} A = \sum_{i=1}^{p} \underline{\underline{\Sigma}}^{i} \underline{E} A_i = \left[\sum_{i=1}^{p} \underline{\underline{\Sigma}}^{i} A_i \right] \underline{E}. \tag{4.6}$$

In other words, we can write:

$$\underline{J}^{tot} = \underline{\underline{\Sigma}}^{eq} \underline{E}, \tag{4.7}$$

where $\underline{\underline{\Sigma}}^{eq}$ denotes the equivalent conductivity of the laminate

$$\underline{\underline{\Sigma}}^{eq} = \frac{1}{A} \left[\sum_{i=1}^{p} \underline{\underline{\Sigma}}^{i} A_i \right] = \frac{1}{h} \left[\sum_{i=1}^{p} \underline{\underline{\Sigma}}^{i} h_i \right]. \tag{4.8}$$

As shown earlier, transverse cracks modifies Σ_{22} of the damaged ply. Since it is assumed that the ply is uniformly cracked, the change in Σ_{22} is constant over the cracked ply. Now, let $(\underline{J}^{tot^\circ}, \underline{E}^\circ, \underline{\underline{\Sigma}}^{eq^\circ})$ denote the current density, electric field, and equivalent conductivity before damage and $(\underline{J}^{tot}, \underline{E}, \underline{\underline{\Sigma}}^{eq})$ denote the same quantities after damage. Since the applied current through the electrodes remains the same, the current densities $\underline{J}^{tot^\circ}$ and $\underline{J}^{tot}$ before and after damage should be the same. Therefore

$$\underline{\underline{\Sigma}}^{eq}\underline{E} = \underline{\underline{\Sigma}}^{eq^\circ}\underline{E}^\circ. \tag{4.9}$$

Upon expanding Equation (4.9), we get:

$$\Sigma_x^{eq^\circ}E_x^\circ + \Sigma_{xy}^{eq^\circ}E_y^\circ + \Sigma_{xz}^{eq^\circ}E_z^\circ = \Sigma_x^{eq}E_x + \Sigma_{xy}^{eq}E_y + \Sigma_{xz}^{eq}E_z, \tag{4.10}$$

$$\Sigma_{xy}^{eq^\circ}E_x^\circ + \Sigma_y^{eq^\circ}E_y^\circ + \Sigma_{yz}^{eq^\circ}E_z^\circ = \Sigma_{xy}^{eq}E_x + \Sigma_y^{eq}E_y + \Sigma_{yz}^{eq}E_z, \tag{4.11}$$

$$\Sigma_{xz}^{eq^\circ}E_x^\circ + \Sigma_{yz}^{eq^\circ}E_y^\circ + \Sigma_z^{eq^\circ}E_z^\circ = \Sigma_{xz}^{eq}E_x + \Sigma_{yz}^{eq}E_y + \Sigma_z^{eq}E_z. \tag{4.12}$$

Since the cracks are oriented along the y-axis, the only component of conductivity that changes with the evolution of transverse cracks is Σ_x^{eq}. Hence, all other components cancel out, resulting in

$$\Sigma_x^{eq^\circ}E_x^\circ = \Sigma_x^{eq}E_x, \tag{4.13}$$

$$E_x = \frac{\Sigma_x^{eq^\circ}}{\Sigma_x^{eq}}E_x^\circ. \tag{4.14}$$

With abuse of notation, let l be any length along the x-axis between the current injection electrodes. Integrating E_x over length l, we thus get:

$$\int_l E_x dx = \frac{\Sigma_x^{eq^\circ}}{\Sigma_x^{eq}} \int_l E_x^\circ dx, \tag{4.15}$$

$$\triangle V = \frac{\Sigma_x^{eq^\circ}}{\Sigma_x^{eq}} \triangle V^\circ, \tag{4.16}$$

where $\triangle V$ and $\triangle V^\circ$ denote the potential difference over the length l for damaged and undamaged specimens. So the percentage change in voltage due to damage is given as

$$\frac{\triangle V - \triangle V^\circ}{\triangle V^\circ} \times 100\% = \left(\frac{\Sigma_x^{eq^\circ}}{\Sigma_x^{eq}} - 1 \right) \times 100\%. \tag{4.17}$$

Let us denote the conductivity of the cracked ply as Σ_x^{cr} and height of the cracked ply as h^{cr}. Since $\Sigma_x^{eq^\circ} = \Sigma_x^{eq}$ for all plies except the cracked ply, Eq. (4.17) can be further simplified as

$$\frac{\triangle V - \triangle V^\circ}{\triangle V^\circ} \times 100\% = \left(\frac{(\Sigma_x^{cr^\circ} - \Sigma_x^{cr}) h_{cr}}{\sum_{i=1}^{p} \Sigma_x^i h_i} \right) \times 100\%, \tag{4.18}$$

Although this equation has been derived for a single cracked ply, it can be extended to estimate the voltage change due to any conductivity changing mechanism modifying the conductivity component along the direction of the current (x-direction in this case). Upon extension, we get

$$\frac{\triangle V - \triangle V^\circ}{\triangle V^\circ} \times 100\% = \left(\frac{\sum_{cr=1}^{t^{cr}} (\Sigma_x^{cr^\circ} - \Sigma_x^{cr}) h_{cr}}{\sum_{i=1}^{p} \Sigma_x^i h_i} \right) \times 100\%, \tag{4.19}$$

where t^{cr} denotes the total number of cracked plies. Eq. (4.19) shows that the change in the electrical potential is directly proportional to the magnitude of the change in the conductivity of damaged/cracked plies and thickness ratio, and inversely proportional to conductivity ratio. This trend agrees with the results of the parametric study conducted earlier. Fig. 4.9 shows the comparison of the data obtained from the FEM analysis for cross-ply and quasi-isotropic laminates with the value obtained through the analytical expression. It can be seen that they agree quite well. Fig. 4.10 (a) & (b) shows the expected relative variation in voltage measurements at any point between the current injecting electrodes for increasing level of damage for cross-ply and quasi-isotropic laminates respectively, with the same configuration as used for the FEM analysis for various λ, obtained using the derived analytical expression. If we consider a threshold of 10% for reliable detection of transverse cracks, it can be evaluated from the analytical expression that EIT cannot be used to accurately monitor the evolution of transverse cracks when $\lambda \geq 5$ and $\lambda \geq 4$ for cross-ply and quasi-isotropic laminates respectively. For a given laminate with any stacking sequence, and known material and geometrical properties, this analytical expression gives the expected voltage change given that the electric field is in-plane. Thus it can indicate the limitations of the usability of ET for tracking transverse cracks a priori without expensive numerical or experimental campaigns.

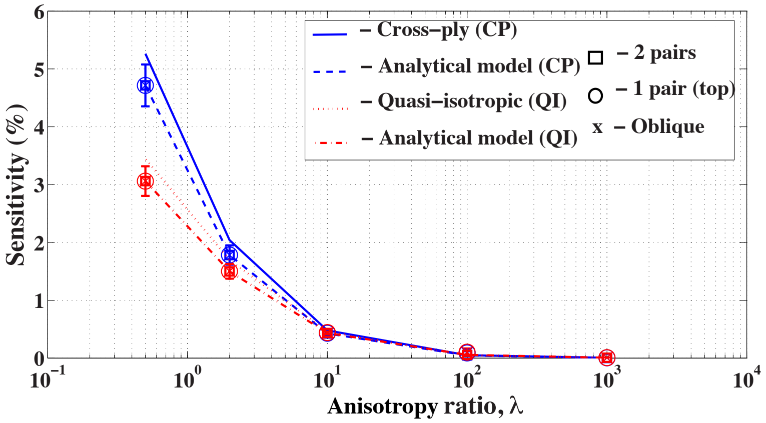

Figure 4.9: Comparison between analytical model and numerical results

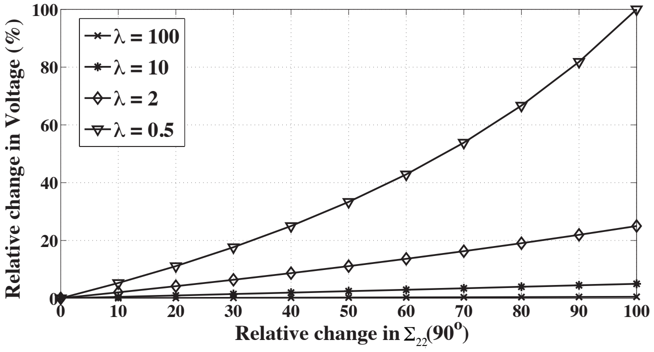

(a) Cross-ply laminate

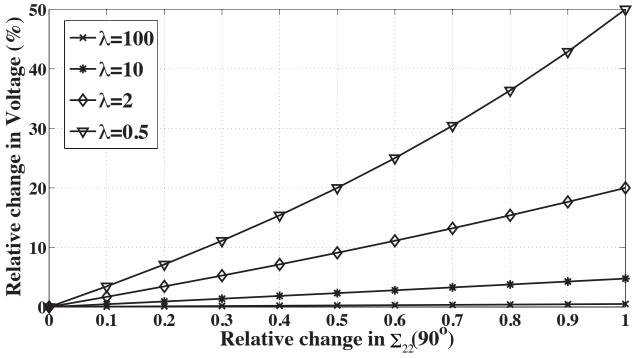

(b) Quasi-isotropic laminate

Figure 4.10: Expected relative variation in voltage with increasing d_e for various λ

4.4 Discussion

The results of the study have clearly put in evidence the following facts:

1. When considering the optimal current injection pattern, it can be seen that 2-pairs/oblique gives better penetration through the thickness of the laminate than the injection through just the top electrodes. 2-pairs injection also results in an in-plane electric field within the laminate.

2. For the cross-ply and quasi-isotropic laminates, it is shown that sensitivity reduces drastically with increasing conductivity ratio. If we consider a conservative minimum threshold of 10% change in the voltage measurements for accu-

rate/reliable detection, then the maximum feasible λ reduces to 3. Detecting transverse cracks for typical CFRP laminates is hence unfeasible in the current framework.

3. For $\lambda \geq 30$, the presence of other conductivity changing mechanisms can make the detection of transverse cracks difficult. In [77], for a sample with $\lambda = 27$, a potential change of 2.4% due to piezoresistivity and matrix cracking was observed of which 0.4% was attributed to matrix cracking alone. It is seen that the variation due to piezoresistivity is 5 times higher than due to transverse cracks. In [92], it was shown that matrix cracks were indistinguishable in the presence of delamination. Hence, it is to be noted that as λ increases, the effect of other conductivity changing mechanisms such as piezoresistivity, fiber breakage, delamination etc., will hide the effect of transverse cracks.

4. Since decreasing the thickness ratio improves the sensitivity, ET could be applied to cross-ply laminates with nano-doped matrix and very thick mid layer.

5. Going back to Fig. 2.5, the plot can now be divided into two zones as shown in Fig. 4.11: (i) feasible zone, where the technique can be used, (ii) unfeasible zone where λ is too high and the technique is unreliable. This is based on the conservative estimate that a minimum of 10% variation in the voltage measurements is needed for reliable estimation. However, if the geometrical parameters can be designed to improve the nominal λ of the laminate (see Section 4.2.3) or the level of noise is much lower, then the feasible zone can be further expanded. It should also be noted that as Σ_{11} decreases, the electrical energy applied to the laminate increases, thereby elevating its temperature. This is undesirable and should be avoided, as increasing temperature increases the thermal stress of the laminate and can potentially lead to damage. This limits the usage of

ET for composites with very low Σ_{11}. However, to the author's best knowledge, the exact limiting value of Σ_{11}, below which the method cannot be applied, has not been reported in the literature. Hence, this zone is not marked in Fig. 4.11.

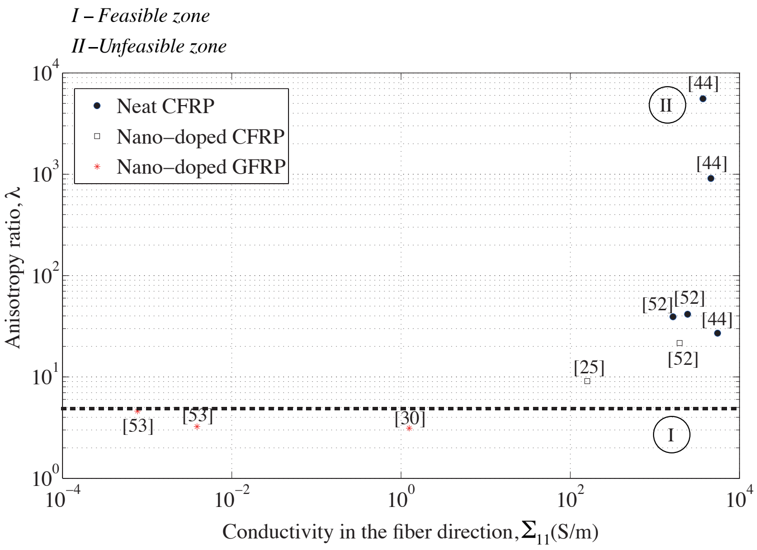

Figure 4.11: Material configurations suitable for detecting transverse cracks with electrical tomography

Chapter 5

Preliminary reconstruction

Abstract

The mesoscale homogenization provides the framework to link the microscale damage mechanisms to conductivity at the ply level. Also, the sensitivity study performed earlier provides guidelines on the scenarios in which electrical tomography is best suitable to identify transverse cracking. In this chapter, we will show a preliminary demonstration to show the potential of the mesoscale homogenization in quantitatively identifying transverse cracks in laminates. First, the equivalence between the measurements obtained between the cracked laminate and the equivalent mesoscale model is shown for a 2D sample problem. Then the reconstruction of the mesoscale conductivity is carried out using two reduced bases. Last, the quality of the results with noise in the measurements is demonstrated.

5.1 Introduction

The ill-posedness of the electrical tomography problem and the various existing methods to regularize the inverse problem has been discussed in the beginning of the thesis. Most of the regularization methods have been developed for medical imaging and anisotropy is not considered. For composite laminates, where anisotropy is prominent, these methods, although they produce conductivity maps, are not ideal. Mesoscale homogenization provides a way to introduce process specific regularization that is suitable for composite laminates. Apart from providing the relationship by which ply conductivity is modified locally by damage, mesoscale homogenization also participates in the regularization in two ways. Since the equivalent mesoscale conductivity is constant through the thickness, the conductivity can be reduced to just in-plane variations. Also, since the equivalent conductivity is continuous in the in-plane direction it can be expressed over a reduced basis that is different from the finite element basis, thereby drastically reducing the number of unknowns. The following chapter demonstrates the capability of the mesoscale guided electrical tomography through several 2D examples.

To begin with, the measurements obtained between the cracked model (micromodel) and the equivalent mesoscale model is compared to show the equivalence for various uniform crack densities. Second, we reconstruct the mesoscale conductivity of laminates with pseudo-periodical crack patterns using 2 reduced bases namely: Fourier basis and piecewise constant basis. The performance of the inverse model for measurements with noise is demonstrated.

5.2 Equivalence between micro and meso measurements

First, the voltage measurements obtained from cracked and equivalent mesoscale model are compared for various uniform crack densities. For this study, laminate beams of two commonly used stacking sequence are taken: cross-ply $[0^\circ_4/90^\circ_4/0^\circ_4]$ and quasi-isotropic laminates $[0^\circ_2/90^\circ_2/45^\circ_2/-45^\circ_2]_s$. The length of the beam is taken as 220mm and the thickness of a single layer is taken as 0.25mm. The laminates are considered to have transverse cracks in the 90° plies. In the case of the quasi-isotropic laminate, cracks are taken to be on both the 90° plies. An array of electrodes is placed on the top surface of the laminates. The electrodes have a width of 5mm and are placed 10mm apart each other as shown in Fig. 5.1. Current is applied between the outermost electrodes that are located at a distance of $d_I = 200$mm and voltage is measured at each inner electrode. The conductivity of the ply in the local basis is taken as:

$$\underline{\underline{\Sigma}}^{\circ} = \begin{bmatrix} 3 & 0 & 0 \\ 0 & 1 & 0 \\ 0 & 0 & 1 \end{bmatrix}_{(e_1,e_2,e_3)} \tag{5.1}$$

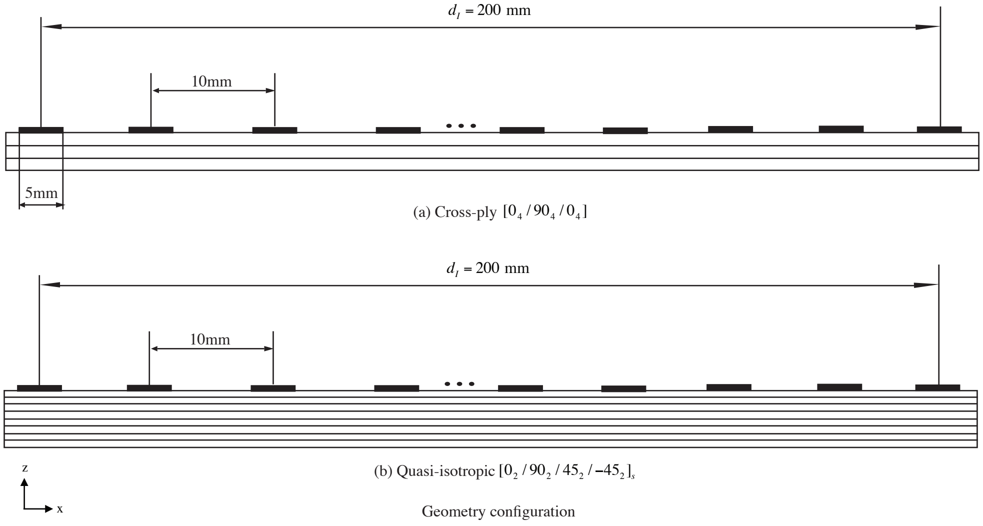

Figure 5.1: Configuration of the laminate cross-section

The cracks are taken to be uniformly spaced denoting crack densities of $\rho = [0.25, 0.5, 0.75, 1]$. Fig. 5.2 shows the mesoscale relationship between the damage indicator and ρ for the conductivity considered. A cubic polynomial fit to the damage indicator is obtained and the fit is shown in Fig. 5.2. The equivalent mesoscale conductivity is obtained using the procedure outlined in Fig. 5.3. To calculate the equivalent mesoscale conductivity, a specific homogenization length scale is chosen. The homogenization length scale is the length scale over which the effect of transverse cracks is averaged. The homogenization length is chosen as 10mm considering that the minimum distance at which the measurements are taken is 10mm. For each point in the cracked ply, the number of cracks within this length is identified and the corresponding ρ is calculated. Damage, d_e^2 corresponding to the ρ is determined through the polynomial fit. The local equivalent mesoscale conductivity, $\Sigma_{22}(90^\circ) = 1 - d_e^2$ is then obtained. The obtained measurements from cracked and equivalent meso model are then compared.

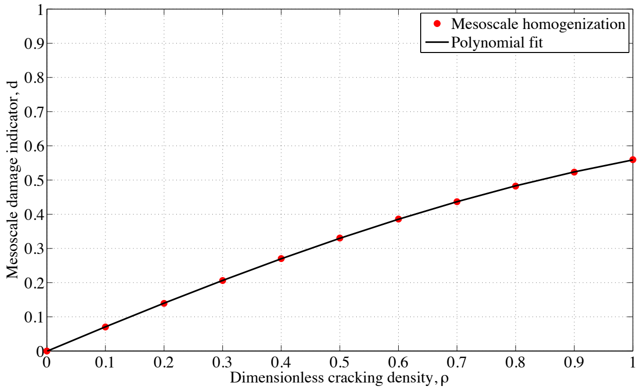

Figure 5.2: Mesoscale homogenization and polynomial fit

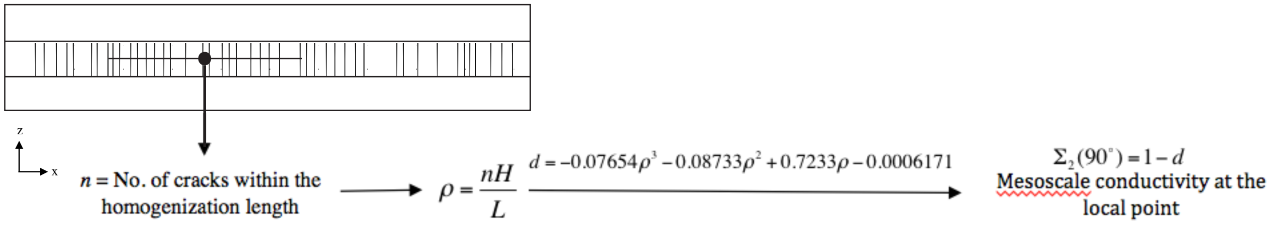

Figure 5.3: Micro to meso description

The voltage measurements are obtained for the micro and meso model as V_{micro} and V_{meso} respectively. The voltage measurements of the uncracked pristine sample is taken as $V_{nocracks}$. We plot two quantities of interest:

$$\%\text{Rel. error} = \frac{V_{meso} - V_{micro}}{V_{micro}} \times 100\%$$

as a measure to compare the error between the micro and meso measurements and

$$\%\text{Rel. variation} = \frac{V_{meso} - V_{micro}}{V_{nocracks} - V_{micro}} \times 100\%$$

as a measure to compare how big the variation between the micro and meso measurements is when compared to the change observed due to the presence of cracks.

Fig. 5.4 shows the % rel. error for the crack densities for both cross-ply and quasi-isotropic laminates. The standard deviation bar in the graph shows the variation observed in the measurements obtained from the different electrodes. From Fig. 5.4, we can see that the % rel. error increases with the decreasing crack spacing. However, the % rel. error is still quite small (below 0.4%). We also observe that the standard deviation in the measurements due to the position of the measurement electrode is minimal. Fig. 5.5 shows % rel. variation for different crack densities for both cross-ply and quasi-isotropic laminates. The % rel. variation decreases with increasing crack density. Even for smaller crack densities, the % rel. variation is quite small (the maximum being around 9%). This shows that the error is quite small when compared to the change obtained due to introduction of cracks. Based on this study, we see that not only does mesoscale homogenization provides an equivalent description of the conductivity at the ply level but also equivalent discrete voltage measurements.

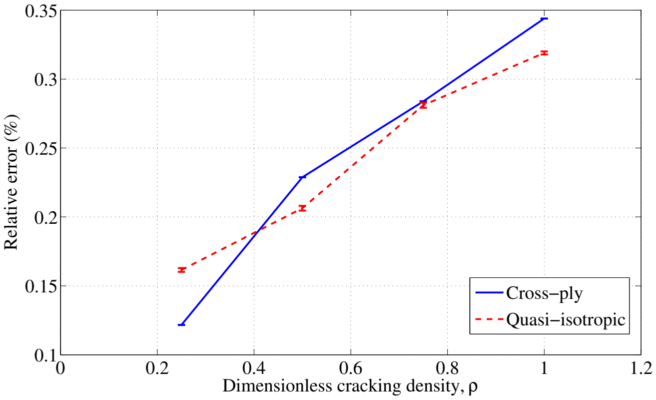

Figure 5.4: $\dfrac{V_{meso} - V_{micro}}{V_{micro}} \times 100\%$ for all crack spacings

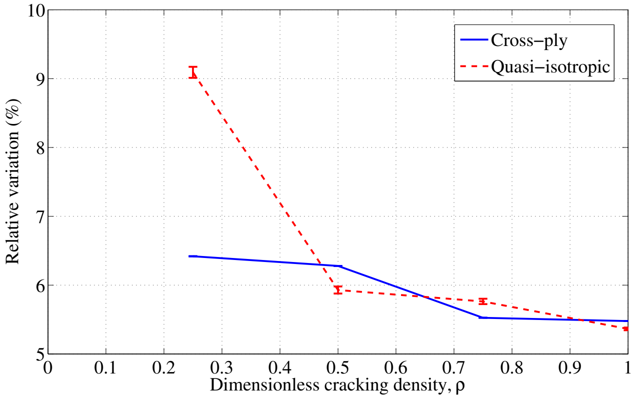

Figure 5.5: $\frac{V_{meso} - V_{micro}}{V_{nocracks} - V_{micro}} \times 100\%$ for various crack spacings

5.3 Reconstruction using reduced basis

In the previous section, we have shown that the mesoscale conductivity produces measurements that are equivalent to the measurements obtained from the cracked model. When it comes to reconstruction, the implications of mesoscale homogenization are two-fold: (i) the conductivity obtained is constant through the thickness of the ply, so the conductivity can be represented as an in-plane field and (ii) when reconstructed the obtained in-plane conductivity will be the mesoscale representation of the conductivity. The first implication reduces the conductivity field to:

$$\underline{\underline{\Sigma}}(x, y, z) \rightarrow \underline{\underline{\Sigma}}(x, y) \tag{5.2}$$

The conductivity can be further regularized in the in-plane direction. This is done using reduced basis method where the in-plane conductivity component, Σ_m of a ply is represented as a linear combination of an orthogonal basis (φ) such that

$$\Sigma_m = \sum_{i=1}^{N} \alpha_i \varphi_i \tag{5.3}$$

By representing the conductivity on a reduced basis that is independent of the finite element mesh, the number of parameters to be estimated by the inverse problem is drastically reduced and the inverse problem is further regularized. Although the concept of reduced order basis is not new, the novelty of this approach lies in how mesoscale homogenization participates in the regularization. There are plenty of different choices for the basis, namely polynomials, piecewise constant, Fourier, POD, etc.

It is to be noted that the objective is to show the capability of the mesoscale model developed, in obtaining and interpreting the conductivity of the laminate and hence the choice of the basis is not studied in detail. Different basis functions can and need to be used based on the experimental configuration that is studied.

For a simple demonstration, we consider a cross-ply laminate with the geometrical and electrode configuration as shown in Fig. 5.1. The 90° ply is considered to have different transverse crack patterns as shown in Fig. 5.6. The crack patterns are generated using a stochastic algorithm that simulates the transverse crack evolution in a laminate based on the load and material properties. The generated crack patterns are quasi-periodic and represent a statistically representative crack pattern at different time intervals over a single loading cycle. Expansions based on truncated Fourier series and piecewise constant functions has been chosen for the reconstruction. EIDORS [93], an open source software based on MATLAB has been modified to solve the problem using bilinear quadrilateral elements. Specific functions have been added to implement the reduced order basis method. The finite element discretization is carried out in GMSH.

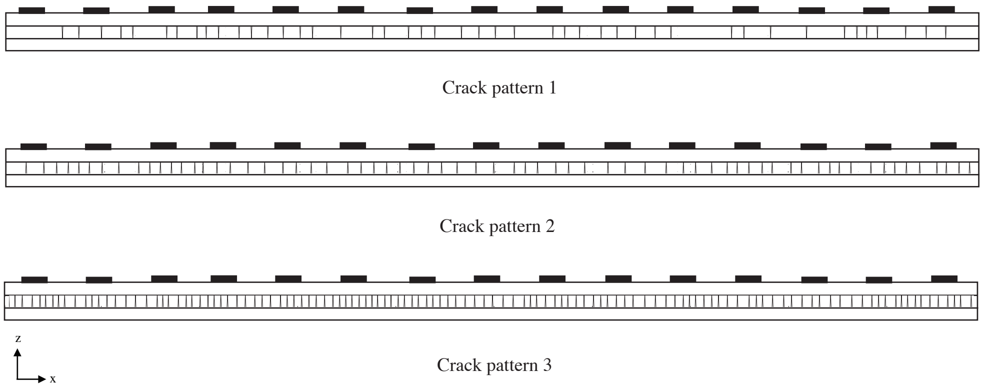

Figure 5.6: The different crack patterns in the 90° ply of the cross-ply laminate that is reconstructed using ET

First, the mesoscale conductivity for the cracked laminate is obtained using the procedure outlined in Fig. 5.3 for a homogenization length of 10mm. Current is injected through all possible pairs of electrodes without repetition in turns and the voltage measurements are obtained from all the other pairs of electrodes for each current injection pattern by solving the forward problem described in Section 2.3.1. The voltage data from the equivalent laminate is taken as $V(t_2)$ and the uncracked pristine laminate is taken as $V(t_1)$. These are provided as input to the inverse problem. In the inverse problem, the transverse conductivity of the 90° ply, $\Sigma_{22}(90°)$ is approximated using the basis functions and is taken as the unknown. Since the conductivity is constant through the thickness, the 2D field is reduced to 1D variation along the length of the ply. All the other components of the conductivity are taken to be constant.

For the Fourier basis, $\Sigma_{22}(90°)$ is taken as:

$$\Sigma_{22}(90°) = \alpha_0 + \sum_{n=1}^{n_m}(\alpha_n cos\frac{\pi n x}{L} + \beta_n sin\frac{\pi n x}{L}) \tag{5.4}$$

where $\alpha = \{\alpha_0, \alpha_n, \beta_n\} \in \mathbb{R}^N$ are the coefficients to be identified and L is the length of the ply. The number of Fourier modes, n depends on the number of available independent measurements. For this study, the number of Fourier modes chosen is 10 i.e., the number of coefficients to be reconstructed is 21. 10 modes is chosen as it is sufficient to represent the mesoscale conductivity accurately. Also, the number of coefficients is less than the number of independent measurements available, so the inverse problem is stable.

For the piecewise constant basis, $\Sigma_{22}(90^\circ)$ is taken as:

$$\Sigma_{22}(90^\circ) = \sum_{i=1}^{N} \alpha_i \varphi_i \tag{5.5}$$

where

$$\varphi_i(x) = \begin{cases} 1 & x_i < x < x_{i+1} \\ 0 & \text{elsewhere} \end{cases} \tag{5.6}$$

where $x_1 < x < x_2$ represents the length over which the step function is defined and $\alpha \in \mathbb{R}^N$ are the coefficients to be identified. For the reconstruction done here, the length of each piecewise constant element is taken as the length between two electrodes which is 10mm.

$V(t_1) \in \mathbb{R}^M$ and $V(t_2) \in \mathbb{R}^M$ denote the voltage measurements at two different times t_1 and t_2 respectively. The objective is then to identify the change in conductivity $\Delta\Sigma_{22}(90^\circ)$ that corresponds to the observed voltage measurement change, $\Delta V = V(t_2) - V(t_1)$. It is assumed that this change in conductivity is linear and is recovered using a single step Gauss-Newton algorithm. The reconstruction algorithm is described in Fig. 5.7.

The change in the mesoscale conductivity of the 90° ply due to transverse cracks and the reconstructed conductivity for the various crack patterns are shown in Fig. 5.8.

Reconstructing the conductivity using a reduced basis provides very good results as the condition number of the sensitivity matrix is significantly improved. However, the conductivity along the edge of the sample is overestimated. This is because of the voltage difference data is only available from the electrodes located between -80 and 80mm.

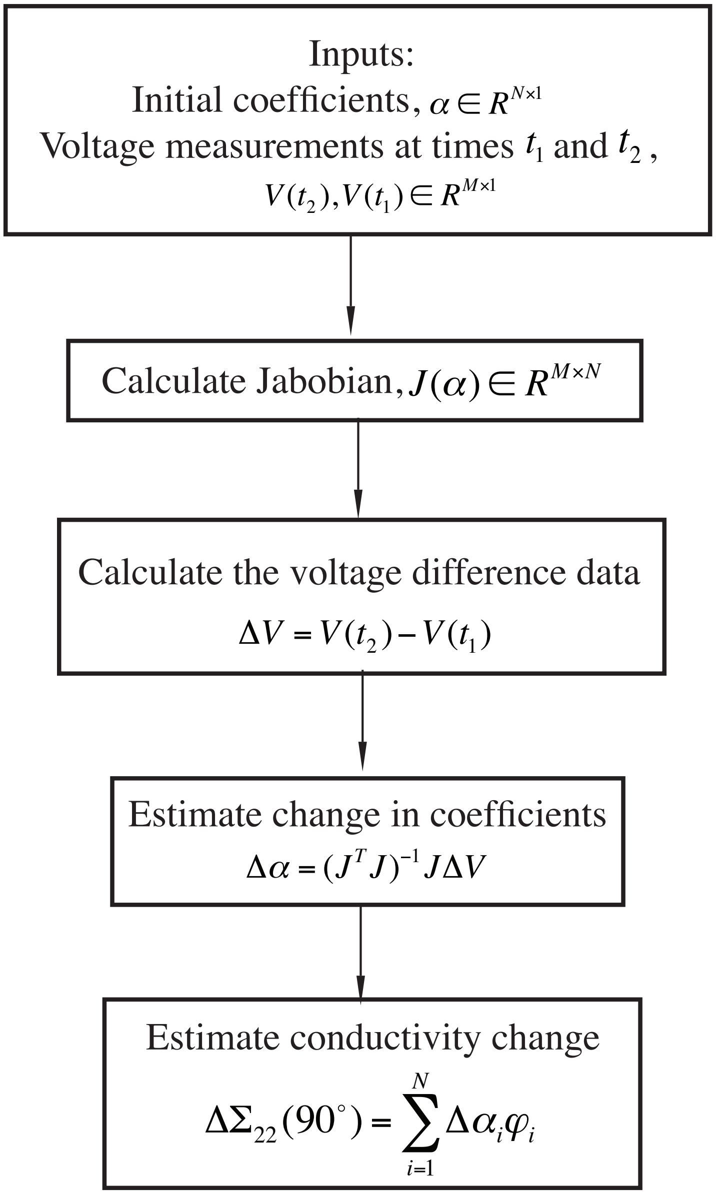

Figure 5.7: Reconstruction algorithm

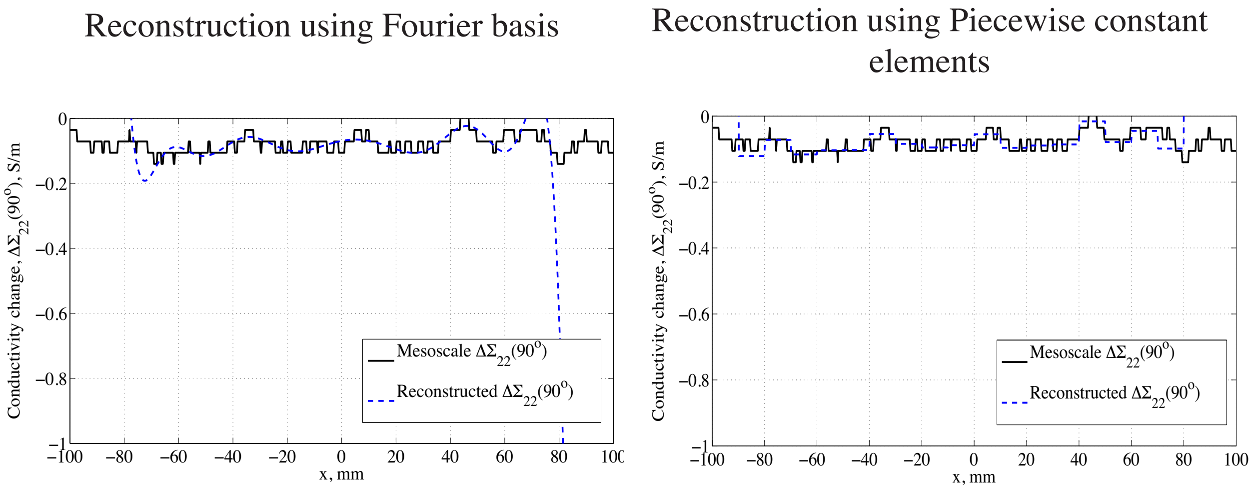

(a) Crack pattern 1

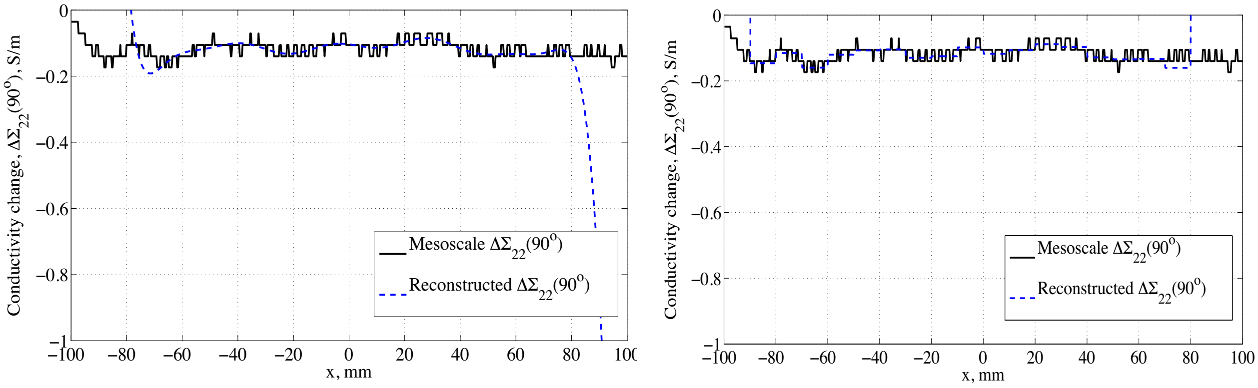

(b) Crack pattern 2

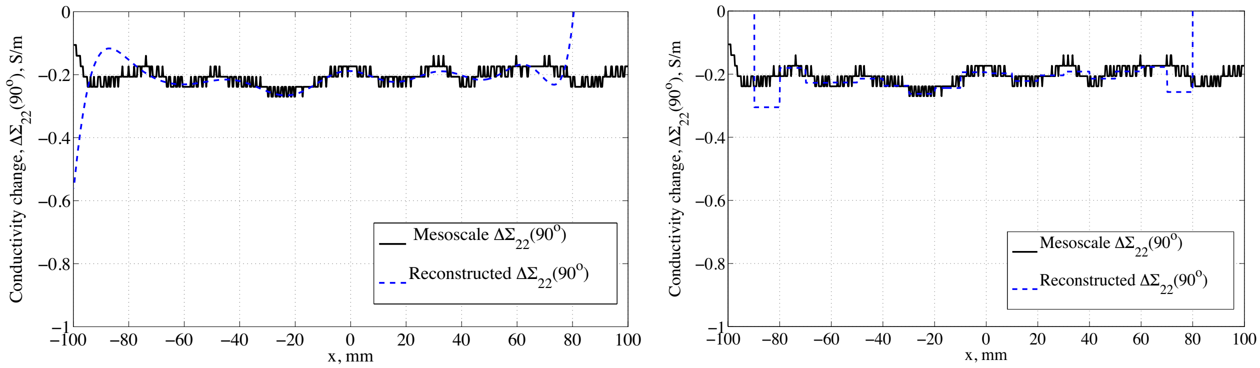

(c) Crack pattern 3

Figure 5.8: The equivalent mesoscale conductivity and the reconstructed conductivity for all the three cracks patterns in the cross-ply laminate

Additive white Gaussian noise is added to the voltage data and the reconstruction is carried out again. The performance of the reconstruction from data with two different noise levels of 60 dB and 50 dB is shown in Fig. 5.9 and 5.10. It can be seen from the results that the reduced order basis still provides a good approximation of the mesoscale conductivity with noisy measurements. It is to be noted that the relative error in the measurements due to the added noise is higher than the relative error of mesoscale approximation. Also typical ET measurement systems have a noise level of 60dB-90dB [94, 95, 96]. Based on this, a good performance at noise levels of 60dB and 50dB demonstrates that the reconstruction algorithm is stable and should provide good results on measurements obtained from typical ET systems. Similar results are obtained for quasi-isotropic laminates with transverse cracks in the 90° plies. However, the results are not shown here.

Reconstruction using Fourier basis

Reconstruction using Piecewise constant elements

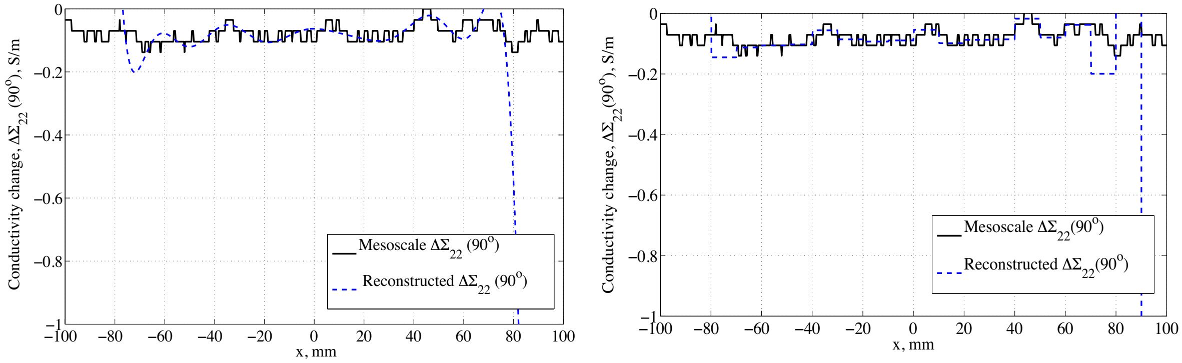

(a) Crack pattern 1

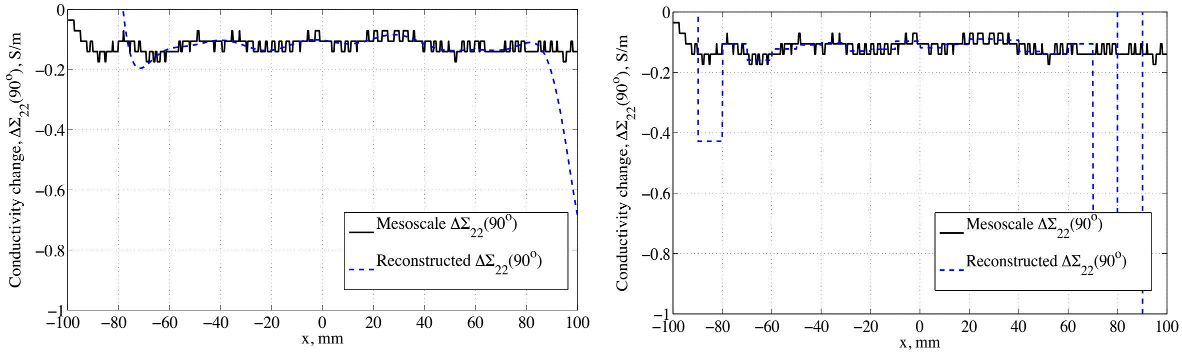

(b) Crack pattern 2

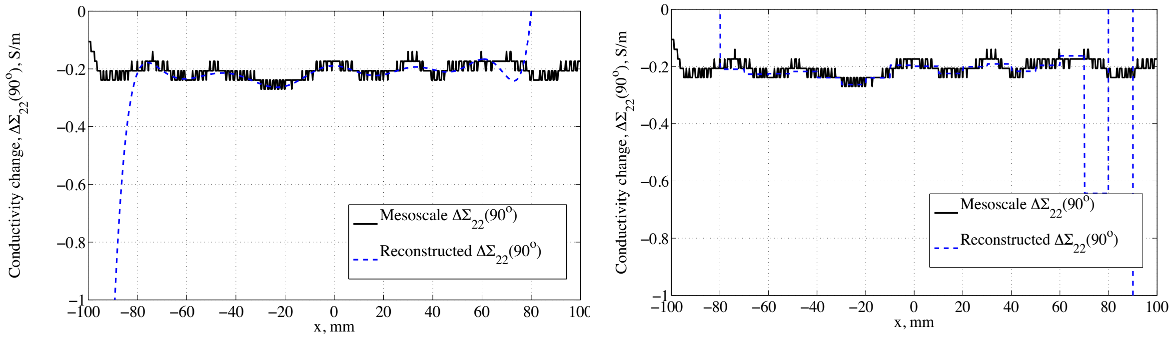

(c) Crack pattern 3

Figure 5.9: The equivalent mesoscale conductivity and the reconstructed conductivity for all the three cracks patterns in the cross-ply laminate with a noise of 60DB SNR

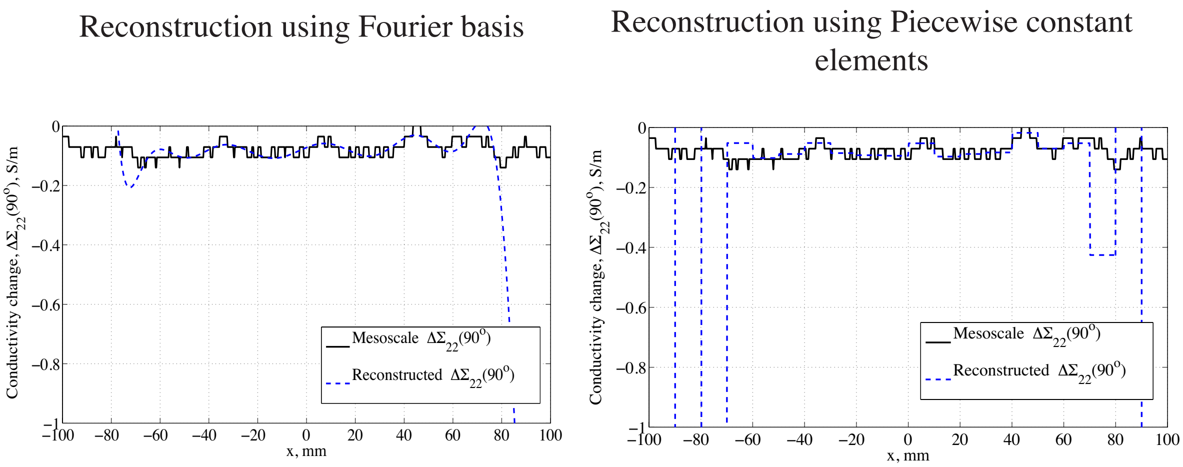
Reconstruction using Fourier basis

Reconstruction using Piecewise constant elements

(a) Crack pattern 1

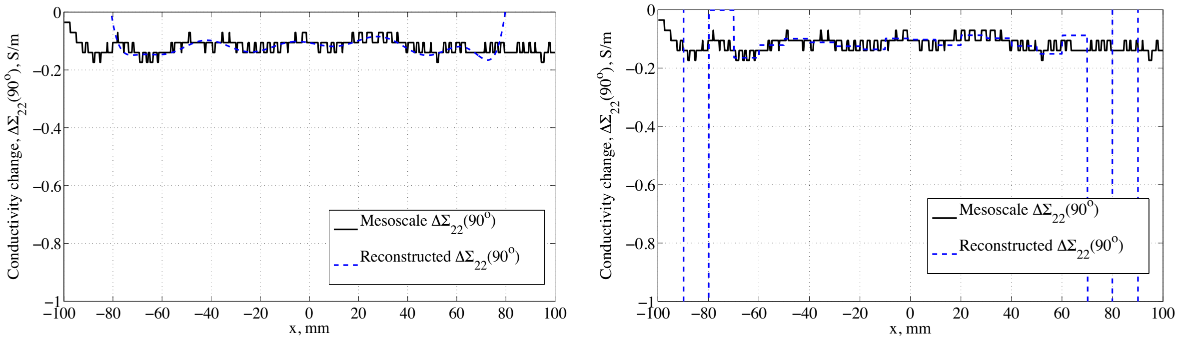

(b) Crack pattern 2

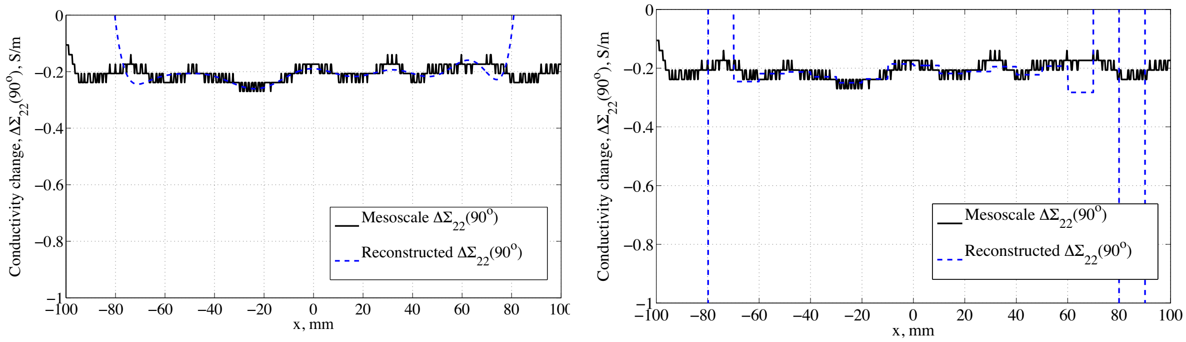

(c) Crack pattern 3

Figure 5.10: The equivalent mesoscale conductivity and the reconstructed conductivity for all the three cracks patterns in the cross-ply laminate with a noise of 50DB SNR

5.4 Discussion

Mesoscale homogenization is used to regularize the inverse problem and preliminary results of quantitative identification of the transverse cracks in a composite laminate is presented. The performance of the method in the presence of noisy measurements are shown. It should be noted that at the present stage, the reconstruction strategy presented here can only be applied to laminates where transverse cracking is the only non-reversible conductivity reducing mechanism. When multiple damage mechanisms occur simultaneously, the conductivity change becomes complex and the whole anisotropic conductivity of the laminate needs to be reconstructed. This requires a new strategy to solve the anisotropic inverse problem which is out of the scope of this work and will be addressed in the future.

Chapter 6

Conclusions

6.1 Summary of the contributions

Earlier studies have shown the capabilities of using electrical measurements to monitor the health of composite laminates. From studying the global behavior, it has been shown that electrical measurements can be used to identify strain and the different damage mechanisms. Conductivity/potential mapping have shown that electrical measurements can be used to coarsely locate the impact damage within the material. Based on these studies, the last few years have seen increasing interest in using ET as a structural health monitoring tool for laminates. Despite its potential as a structural health monitoring technique for laminates, ET has several strong limitations in terms of detectability and the interpretation of conductivity map. Multiple damage mechanisms and anisotropy in conductivity have limited the application of electrical tomography to qualitative characterization of macroscale damage such as impact damage.

This work attempts to extend the capability of ET as an quantitative interpretation tool. The major contributions of the work are discussed below. The mesoscale homogenization developed can not only be used as a tool to interpret the conductivity change due to the different damage mechanisms but also participates in the regularization of the inverse problem. This enhances the quality of the conductivity estimates obtained.

6.1.1 Interpretation of the conductivity change

This work is a pioneering effort to quantify the effect of microscale damage on the macroscale observations. This is done by bridging the microscale damage mechanisms to the conductivity change at the ply level through mesoscale homogenization. The framework of mesoscale homogenization has been presented and the relationship between ply conductivity and the various damage mechanisms have been derived. It has to be noted that this is the first attempt to link two scales and as a consequence quantify the effect of the individual damage mechanisms on the anisotropic conductivity of the composite ply.

This is achieved through the introduction of damage indicators. Specifically, the relationship between the damage indicators and microscale damage such as transverse cracks and local delamination have been presented. The damage indicator has also been shown to be intrinsic to the ply, meaning that the model is generic and can be applied to any laminate configuration.

6.1.2 Composite design for ET

To the best of the author's knowledge, no work has been done to understand the influence of various geometrical and material parameters of the laminate towards detectability of transverse cracks. Based on the sensitivity study performed as part of this work, it is evident that transverse cracks are best observed through electrical measurements in composite laminates that have lower anisotropy in the in-plane direction. From the mesoscale homogenization results, we also observe that for a given crack density, damage is higher in magnitude when the ratio between the transverse and through-thickness conductivity is higher. Thus, this work has provided guidelines on how the detectability can be best tuned through tailoring the anisotropy ratios and thickness ratios of the ply. By doing so, electrical tomography can be applied to applications that require continuous monitoring of transverse cracking.

6.1.3 Quantitative damage identification using electrical tomography

Specific regularization methods for composites that can help in producing not only qualititative conductivity maps but quantitative damage maps are yet to be developed. The mesoscale homogenization has been shown to provide a process specific regularization method. Although, it is a proof of concept and does not involve real-time experimental data, we have shown how the mesoscale homogenization regularizes the conductivity in the through-thickness and in-plane directions and demonstrated how it can be used to quantitatively assess the transverse cracking density within the ply. This work is the first attempt to identify and quantify the transverse cracking density at the ply level. However it is to be noted that the reconstruction results presented here are preliminary and further methods need to be developed to solve the anisotropic reconstruction problem.

Thus, the work carried out has presented a novel framework to quantitatively assess the different damage mechanisms at the ply level by electrical tomography. This is the first step towards making ET a viable structural health monitoring tool for composite laminates.

6.2 Future directions

This work can be extended in the following directions:

Mesoscale relationships

- The relationship between transverse cracking and local delamination mechanisms to the damage indicators were derived for the various laminate configurations. Other interlaminar mechanisms such as fiber breakage and diffuse damage occur at very fine scales and are naturally homogenized. However, the relationship has not been identified. Couple micromechanical and electrical models can be used to model the behavior of electrical properties for the two degradation mechanisms.

- Along with the various damage mechanisms, strain is a primary conductivity changing mechanism. Piezoresistance behaves differently in the different directions of the ply and various factors affect the behavior. Some of them being, the contact between the different fibers in the transverse and through-thickness directions, the waviness and misalignment of the fibers and the piezoresistive behavior of the fiber itself. The piezoresistive behavior can be characterized through homogenization of a geometric microscale model.

- Combined together, the mesoscale damage model and the piezoresistive model will provide the complete description of the change in the anisotropic conductivity due to strain and damage mechanisms.

Conductivity reconstruction

- As mentioned earlier, the reconstruction strategy presented in this work can be used only for the specific scenarios where transverse cracks are isolated. Future work will focus on the reconstruction of the anisotropic conductivity guided by the mesoscale homogenization model. This will be done through specific regularization methods that will address the anisotropy.

- Validation of the mesoscale homogenization guided electrical tomography through real experimental data.

REFERENCES

[1] J. Heida and D. Platenkamp, “Evaluation of non-desctructive inspection methods for composite aerospace structures,” *6th NDT in Progress 2011*, 2011.

[2] K. Schulte, “Sensing with carbon fibres in polymer composites,” *Materials Science Research International*, vol. 8, no. 2, pp. 43–52, 2002.

[3] R. Schueler, S. Joshi, and K. Schulte, “Damage detection in CFRP by electrical conductivity mapping,” *Composites Science and Technology*, vol. 61, pp. 921–930, 2001.

[4] D. Zhang, L. Ye, D. Wang, Y. Tang, S. Mustapha, and Y. Chen, “Assessment of transverse impact damage in GF / EP laminates of conductive nanoparticles using electrical resistivity tomography,” *Composites Part A*, vol. 43, no. 9, pp. 1587–1598, 2012.

[5] A. Baltopoulos, A. Vavouliotis, V. Kostopoulos, N. Polydorides, and L. Pambaguian, *Electrical tomography as a tool for non-destructive assessment of composite structures.* CRC press, 2012, ch. 61, pp. 389–394.

[6] W. Fan, H. Wang, and Z. Cui, “Damage detection of CFRP laminates using open electrical impedance tomography,” *IEEE Instrumentation and Measurement*, pp. 1377–1381, 2015.

[7] F. Campbell, *Structural Composite Materials.* ASM International, 2010.

[8] C. Beetz, “The analysis of carbon fibre strength distributions exhibiting multiple modes of failure,” *Fibre Science and Technology*, vol. 16, pp. 45–59, 1982.

[9] Z. Chi, T. W. Chou, and G. Shen, "Determination of single fibre strength distribution from fibre bundle testings," *Journal of Materials Science*, vol. 19, no. 10, pp. 3319–3324, 1984.

[10] H. Zhang, M. L. Ericson, J. Varna, and L. A. Berglund, "Transverse single-fibre test for interfacial debonding in composites: 1. Experimental observations," *Composites Part A*, vol. 28, pp. 309–315, 1997.

[11] F. Lagattu and M. C. Lafarie-Frenot, "Variation of PEEK matrix crystallinity in APC-2 composite subjected to large shearing deformations," *Composites Science and Technology*, vol. 60, pp. 605–612, 2000.

[12] P. Ladevèze and G. Lubineau, "On a damage mesomodel for laminates: micro-meso relationships, possibilities and limits," *Composites Science and Technology*, vol. 61, pp. 2149–2158, 2001.

[13] H. Nouri, G. Lubineau, and D. Traudes, "An experimental investigation of the effect of shear-induced diffuse damage on transverse cracking in carbon-fiber reinforced laminates," *Composite Structures*, vol. 106, pp. 529–536, 2013.

[14] G. Lubineau, "A pyramidal modeling scheme for laminates-Identification of transverse cracking," *International Journal of Damage Mechanics*, vol. 19, no. 4, pp. 499–518, 2010.

[15] J. Nairn and S. Hu, "The initiation and growth of delaminations induced by matrix microcracks in laminated composites," *International journal of fracture*, vol. 57, pp. 1–24, 1992.

[16] S. Ogihara and N. Takeda, "Interaction between transverse cracks and delamination during damage progress in CFRP cross-ply laminates," *Composites Science and Technology*, vol. 54, no. 4, pp. 395–404, Jan. 1995.

[17] J. Zhang, J. Fan, and K. P. Herrmann, "Delaminations induced by constrained transverse cracking in symmetric composite laminates," *International Journal of Solids and Structures*, vol. 36, pp. 813–846, 1999.

[18] P. Ladevèze and G. Lubineau, "An enhanced mesomodel for laminates based on micromechanics," *Composites Science and Technology*, vol. 62, pp. 533–541, 2002.

[19] P. Ladevèze, G. Lubineau, and D. Marsal, "Towards a bridge between the micro- and the mesomechanics of delamination for laminated composites," *Composites Science and Technology*, vol. 66, no. 6, pp. 698–712, 2006.

[20] F.-K. Chang, Ed., *Structural health monitoring 2013: from diagnostics & prognostics to structural health management.* DEStech Publications, September 2013.

[21] H.-N. Li, D.-S. Li, and G.-B. Song, "Recent applications of fiber optic sensors to health monitoring in civil engineering," *Engineering structures*, vol. 26, pp. 1647–1657, 2004.

[22] I. De Rosa, C. Santulli, and F. Sarasini, "Acoustic emission for monitoring the mechanical behaviour of natural fibre composites: a literature review," *Composites Part A*, vol. 40, pp. 1456–1469, 2009.

[23] F. Aymerich and S. Meili, "Ultrasonic evaluation of matrix damage in impacted composite laminates," *Composites Part B: Engineering*, vol. 31, pp. 1–6, 2000.

[24] C. Ciang, J.-R. Lee, and H.-J. Bang, "Structural health monitoring for a wind turbine system: a reivew of damage detection methods," *Measurement Science and Technology*, vol. 19, 2008.

[25] C. Ng and M. Veidt, "A lamb wave based technique for damage detection in composite laminates," *Smart Materials and Structures*, vol. 18, pp. 1–12, 2009.

[26] Z. Su, L. Ye, and L. Ye, "Guided lamb waves for identification of damage in composite structures: a review," *Journal of sound and vibration*, vol. 295, pp. 753–780, 2006.

[27] N. Goldfine, V. Zilberstein, D. Schlicker, and Y. Sheiretov, "Surface mounted periodic field eddy current sensors for structural health monitoring," *SPIE conference: Smart structures and materials*, 2001.

[28] N. Polydorides, “Image reconstruction algorithms in soft-field tomography,” Ph.D. dissertation, University of Manchester Institute of Science and Tehnology, 2002.

[29] A. Borsic, “Regularisation methods for imaging from electrical measurements,” Ph.D. dissertation, Oxford Brookes University, 2002.

[30] A. Matzenmiller, J. Lubliner, and R. L. Taylor, “A constitutive model for anisotropic damage in fiber-composites,” *Mechanics of Materials*, vol. 20, no. 2, pp. 125–152, 1995.

[31] N. Laws and G. Dvorak, “Progressive transverse cracking in composite laminates,” *Journal of composite materials*, vol. 22, pp. 900–916, 1992.

[32] A. Adler, R. Gaburro, and W. Lionheart, *Handbook of mathematical models in imaging.* Springer, 2011, ch. Electrical Impedance tomography.

[33] J. Herwanger, C. Pain, A. Binley, C. De Oliveira, and M. Worthington, “Anisotropic resistivity tomography,” *Geophys. J. Int*, vol. 158, pp. 408–425, 2004.

[34] C. Pain, J. Herwanger, J. Saunders, M. Worthington, and C. De Oliveira, “Anisotropic resistivity inversion,” *Inverse problems*, vol. 19, pp. 1081–1111, 2003.

[35] L. Heikkinen, “Statistical estimation methods for electrical process tomography,” Ph.D. dissertation, University of Kuopio, 2005.

[36] V. M, “Electrical impedence tomography and prior information,” Ph.D. dissertation, University of Kuopio, 1997.

[37] K. Wu, J. Yang, F. Fu, F. Tao, and S. Liu, *Comparative study of reconstruction algorithms for electrical impedance tomography.* Spring Congress on Engineering and Technology, 2012.

[38] M. Goharian, M. Soleimani, and G. Moran, "A trust region subproblem for 3D electrical impedance tomography inverse problem using experimental data," *Progress in Electromagnetics research*, vol. 94, pp. 19–32, 2009.

[39] M. Vauhkonen, P. Vauhkonen, J. Kaipio, and P. Karjalainen, "Three dimensional electrical impedance tomography using complete electrode model," *Proceeding of SPIE*, vol. 3171, pp. 166–174, 1997.

[40] Q. Wang, H. Wang, R. Zhang, J. Wang, Y. Zheng, Z. Cui, and C. Yang, "Image reconstruction based on L1 regularization and projection methods for electrical impedance tomography," *Review of scientific instruments*, vol. 83, 2012.

[41] A. Baltopoulos, N. Polydorides, L. Pambaguian, A. Vavouliotis, and V. Kostopoulos, "Damage identification in carbon fiber reinforced polymer plates using electrical resistance tomography mapping," *Journal of composite materials*, 2012.

[42] P. Hua, J. Webster, and W. Tompkins, "A regularised electrical impedance tomography reconstruction algorithm," *Clinical Physics and Physiological Measurement*, vol. 9, pp. 137–141, 1988.

[43] Y. Mamatjan, A. Borsic, D. Gursoy, and A. Adler, "An experimental clinical evaluation of EIT imaging with L1 data and image norms," *Physiological Measurement*, vol. 34, pp. 1027–1039, 2013.

[44] K. Andersen, S. Brooks, and M. Hansen, "A Bayesian approach to crack detection in electrically conducting media," *Inverse problems*, vol. 17, pp. 121–136, 2001.

[45] J. Kaipio, V. Kolehmainen, E. Somersalo, and V. M, "Statistical inversion and Monte Carlo sampling methods in electrical impedance tomography," *Inverse problems*, vol. 16, pp. 1487–1522, 2000.

[46] A. Nissinen, L. Heikkinen, and J. Kaipio, "The Bayesian approximation error approach for electrical impedance tomography-Experimental results," *Measurement Science and Technology*, vol. 19, pp. 1–9, 2008.

[47] A. Adler and R. Guardo, “Electrical impedance tomography: regularized imaging and contrast detection,” *IEEE transactions on medical imaging*, vol. 15, no. 2, pp. 170–179, 1996.

[48] A. Lipponen, A. Seppanen, and J. Kaipio, “Electrical impedance tomography imaging with reduced-order model based on proper orthogonal decomposition,” *Journal of Electronic Imaging*, vol. 22, no. 2, 2013.

[49] J. C. Abry, S. Bochard, A. Chateauminois, M. Salvia, and G. Giraud, “In-situ detection of damage in CFRP laminates by electrical resistance measurements,” *Composites Science and Technology*, vol. 59, pp. 925–935, 1999.

[50] A. Kaddour and et al., “Electrical resistance measurement technique for detecting failure in CFRP materials at high strain rates,” *Composites Science and Technology*, vol. 51, pp. 377–385, 1994.

[51] A. Todoroki, M. Tanaka, and Y. Shimamura, “Measurement of orthotropic electric conductance of CFRP laminates and analysis of the effect on delamination monitoring with an electric resistance change method,” *Composites Science and Technology*, vol. 62, pp. 619–628, 2002.

[52] A. Todoroki and et al., “Effects with a matrix crack on monitoring by electrical resistance method,” *Advanced Composite Materials*, vol. 13, no. 2, pp. 107–120, 2004.

[53] C. May, Ed., *Epoxy resins: chemistry and technology.* CRC press, 1987.

[54] DOW, “Dow liquid epoxy resins,” DOW Plastics, Tech. Rep., 1999.

[55] D. Hartman, M. E. Greenwood, and D. M. Miller, “High strength glass fibers,” AGY, Tech. Rep., 1996.

[56] Torayca, “Torayca data sheet,” Torayca carbon fibers America, Santa Ana, CA, 2005.

[57] Hextow, “Hextow carbon fiber product data,” February 2014.

[58] R. Schueler and et al., “Agglomeration and electrical percolation behavior of carbon black dispersed in epoxy resin,” *Journal of applied polymer science*, vol. 63, pp. 1741–1746, 1997.

[59] J. B. Bai and A. Allaoui, “Effect of the length and the aggregate size of MWNTs on the improvement efficiency of the mechanical and electrical properties of nanocomposites - Experimental investigation,” *Composites Part A*, vol. 34, pp. 689–694, 2003.

[60] S. Bal, “Experimental study of mechanical and electrical properties of carbon nanofiber/epoxy composites,” *Journal of Materials and Design*, 2009.

[61] D. Zhang, L. Ye, S. Deng, J. Zhang, Y. Tang, and Y. Chen, “CF/EP composite laminates with carbon black and copper chloride for improved electrical conductivity and interlaminar fracture toughness,” *Composites Science and Technology*, vol. 72, no. 3, pp. 412–420, 2012.

[62] V. Kostopoulos and et al., “Damage monitoring of carbon fiber reinforced laminates using resistance measurements. Improving sensitivity using carbon nanotube doped epoxy matrix system,” *Journal of Intelligent Material Systems and Structures*, vol. 20, pp. 1025–1034, 2009.

[63] A. Markov, B. Fiedler, and K. Schulte, “Electrical conductivity of carbon black-/fibers filled glass fiber reinforced thermoplastic composites,” *Composites Part A*, vol. 37, pp. 1390–1395, 2006.

[64] A. Todoroki, Y. Samejima, Y. Hirano, and R. Matsuzaki, “Piezoresistivity of unidirectional carbon/epoxy composites for multiaxial loading,” *Composites Science and Technology*, vol. 69, no. 11-12, pp. 1841–1846, 2009.

[65] S. Wang and D. D. L. Chung, “Negative piezoresistivity in continuous carbon fiber epoxy-matrix composite,” *Journal of Materials Science*, vol. 42, no. 13, pp. 4987–4995, 2007.

[66] N. Angelidis, C. Wei, and P. Irving, “The electrical resistance response of continuous carbon fibre composite laminates to mechanical strain,” *Composites Part A: Applied Science and Manufacturing*, vol. 35, no. 10, pp. 1135–1147, 2004.

[67] J. Xiao, Y. Li, and W. X. Fan, “A laminate theory of piezoresistance for composite laminates,” *Composites Science and Technology*, vol. 59, pp. 1369–1373, 1999.

[68] A. McDonach, P. Gardiner, S. McEwen, and B. Culshaw, Eds., *Electrical potential techniques for damage sensing in composite structures*, vol. 2361, Smart structures research insititute. Second European conference on smart materials and structures, 1994.

[69] M. Ceysson.O and L.Vincent, “Damage mechanisms characterization of carbon fibre/epoxy composite laminates by both electrical resistance measurements and acoustic emission analysis,” *Scripta Materialia*, vol. 34, no. 8, pp. 1273–1280, 1996.

[70] J. Abry, Y. Choi, A. Chateauminois, B. Dalloz, G. Giraud, and M. Salvia, “Insitu monitoring of damage in CFRP laminates by means of AC and DC measurements,” *Composites Science and Technology*, vol. 61, no. 6, pp. 855–864, 2001.

[71] B. Chen and J. Liu, “Damage in carbon fiber-reinforced concrete, monitored by both electrical resistance measurement and acoustic emission analysis,” *Construction and Building Materials*, vol. 22, no. 11, pp. 2196–2201, 2008.

[72] A. Todoroki, “Self-Sensing Composites and Optimization of Composite Structures in Japan,” *International Journal of Aeronautical and Space Sciences*, vol. 11, no. 3, pp. 155–166, 2010.

[73] K. Schulte and C. Baron, “Load and failure analyses of CFRP laminates by means of electrical resistivity measurements,” *Composites Science and Technology*, vol. 36, pp. 63–76, 1989.

[74] M. Kupke, K. Schulte, and R. Schu, “Non-destructive testing of FRP by DC and AC electrical methods,” *Composites Science and Technology*, vol. 61, 2001.

[75] J. B. Park, T. Okabe, and N. Takeda, “New concept for modeling the electromechanical behavior of unidirectional carbon-fiber-reinforced plastic under tensile loading,” *Smart Materials and Structures*, vol. 12, no. 1, pp. 105–114, 2003.

[76] Z. Xia and W. Curtin, "Modeling of mechanical damage detection in CFRPs via electrical resistance," *Composites Science and Technology*, vol. 67, no. 7-8, pp. 1518–1529, 2007.

[77] A. Todoroki, K. Omagari, Y. Shimamura, and H. Kobayashi, "Matrix crack detection of CFRP using electrical resistance change with integrated surface probes," *Composites Science and Technology*, vol. 66, no. 11-12, pp. 1539–1545, 2006.

[78] K. Omagari, A. Todoroki, Y. Shimamura, and H. Kobayashi, "Detection of Matrix Cracking of CFRP Using Electrical Resistance Changes," *Key Engineering Materials*, vol. 197-300, pp. 2096–2101, 2005.

[79] A. Todoroki and K. Omagari, "Detection of Matrix Crack Density of CFRP using an Electrical Potential Change Method with Multiple Probes," *Journal of Solid Mechanics and Materials Engineering*, vol. 2, no. 6, pp. 718–729, 2008.

[80] S. Wang, D. Chung, and J. H. Chung, "Impact damage of carbon fiber polymer-matrix composites, studied by electrical resistance measurement," *Composites Part A: Applied Science and Manufacturing*, vol. 36, no. 12, pp. 1707–1715, 2005.

[81] A. Todoroki, "High performance estimations of delamination of graphite/epoxy laminates with electric resistance change method," *Composites Science and Technology*, vol. 63, no. 13, pp. 1911–1920, 2003.

[82] A. Todoroki and M. Ueda, "Low-cost delamination monitoring of CFRP beams using electrical resistance changes with neural networks," *Smart Materials and Structures*, vol. 15, no. 4, pp. 75–84, 2006.

[83] A. Todoroki, Y. Tanaka, and Y. Shimamura, "Multi-probe electric potential change method for delamination monitoring of graphite/epoxy composite plates using normalized response surfaces," *Composites Science and Technology*, vol. 64, no. 5, pp. 749–758, 2004.

[84] M. Ueda and A. Todoroki, "Delamination monitoring of CFRP laminate using the two-stage electric potential change method with equivalent electric conductivity," *Engineering Fracture Mechanics*, vol. 75, no. 9, pp. 2737–2750, 2008.

[85] A. Baltopoulos, N. Polydorides, L. Pambaguian, A. Vavouliotis, and V. Kostopoulos, "Exploiting carbon nanotube networks for damage assessment of fiber reinforced composites," *Composites Part B*, vol. 76, pp. 149–158, 2015.

[86] G. Lubineau and P. Ladevèze, "Construction of a micromechanics based intralaminar mesomodel, and illustrations in abaqus/standard," *Computational Materials Science*, vol. 43, pp. 137–145, 2008.

[87] P. Ladevèze, "Sur la mécanique de l'endommagement des composites," *Comptes-rendus des JNC5*, pp. 667–83, 1986.

[88] P. Ladevèze, G. Lubineau, and D. Violeau, "A Computational Damage Micromodel of Laminated Composites," *International Journal of Fracture*, vol. 137, no. 1-4, pp. 139–150, 2006.

[89] P. Ladevèze and G. Lubineau, "On a damage mesomodel for laminates: micromechanics basis and improvement," *Mechanics of Materials*, vol. 35, pp. 763–775, 2003.

[90] G. Lubineau, H. Nouri, and F. Roger, "On micro-meso relations homogenizing electrical properties of tranversely cracked laminated composites," *Composite Structures*, vol. 105, pp. 66–74, 2013.

[91] L. Selvakumaran and G. Lubineau, "Electrical behavior of laminated composites with intralaminar degradation: a comprehensive micro-meso homogenization procedure," *Composite Structures*, vol. 109, pp. 178–188, 2014.

[92] A.Todoroki and J. Yoshida, "Electrical Resistance Change of Unidirectional CFRP Due to Applied Load," 2004.

[93] A. Adler and W. Lionheart, "Uses and abuses of EIDORS: An extensible software base for EIT," *Physiological Measurement*, vol. 27, pp. S25–S42, 2006.

[94] H. Wi, H. Sohal, A. L. McEwan, E. J. Woo, and T. I. Oh, “Multi-frequency electrical impedance tomography system with automatic self-calibration for long-term monitoring,” *IEEE transactions on biomedical circuits and systems*, vol. 8, pp. 119–128, 2013.

[95] R. J. Halter, A. Hartov, and K. D. Paulsen, “A broadban high-frequency electrical impedance tomography system for breast imaging,” *IEEE transactions on biomedical engineering*, vol. 55, pp. 650–659, 2008.

[96] M. Rafiei-Naeini, P. Wright, and H. McCann, “Low-noise measurement for electrical impedance tomography,” in *IFMBE proceedings*, vol. 17, 2007, pp. 324–327.

7 Journal publications

- Selvakumaran L, Lubineau G, “Electrical behavior of laminated composites with intralaminar degradation: A comprehensive micro-meso homogenization procedure”, *Composite Structures*, 109, 178-188, 2013.
- Selvakumaran L, Long Q, Prudhomme S, Lubineau G, “On the detectability of transverse cracks in laminated composites using electrical potential change measurements”, *Composite Structures*, 121, 237-246, 2015.
- Selvakumaran L, Lubineau G, “Validation of micro-meso electrical relations for laminates with varying anisotropy”, *Applied Mechanics and Materials*, 784, 2015.
- Almuhammadi K, Selvakumaran L, Alfano A, Yang Y, Bera T K, Lubineau G, “Laser-based surface preparation of composite laminates leads to improved electrodes for electrical measurements”, *Applied Surface Science*, Accepted.
- Lubineau G, Yagoubi J, Saghir S, Selvakumaran L, Askari A, “Cyclic hygrothermal aging of aircraft lightning protections: phenomenological overview”, *AIAA proceedings*, 2012.
- Lubineau G, Nouri H, Selvakumaran L, “Towards mechanisms-guided resistivity-based monitoring of damage evolution in laminated composites”, *AIAA proceedings*, 2013.